THE UNIVERSITY OF CHICAGO

MOLECULAR SIMULATION OF ORGANIC GLASSES: TUNING STRUCTURAL PROPERTIES VIA VAPOR DEPOSITION, PHOTOISOMERIZATION, AND CHEMICAL STRUCTURE

A DISSERTATION SUBMITTED TO
THE FACULTY OF THE INSTITUTE FOR MOLECULAR ENGINEERING
IN CANDIDACY FOR THE DEGREE OF
DOCTOR OF PHILOSOPHY

BY
LUCAS WILLIAM ANTONY

CHICAGO, ILLINOIS
AUGUST 2018

To my mother and father, Jeannie and Al

"The strongest of all warriors are these two – Time and Patience."

- Leo Tolstoy, War and Peace

TABLE OF CONTENTS

LIST OF FIGURES

LIST OF TABLES

ACKNOWLEDGMENTS

First and foremost, I would like to thank my advisor Professor Juan de Pablo as none of this work would have been done if not for him. He was willing to take on a student from outside the chemical engineering department at the University of Wisconsin-Madison who had no training in computational science. During my tenure in his group, he has given me many opportunities to push myself while providing support, guidance, and as much computational resources as I desired. In retrospect, I may have been a little slow on the uptake initially coming from the outside, but Juan was patient enough and guided me through.

I'd like to thank the rest of my committee Professor James Skinner and Professor Benoît Roux for giving advice and their time for taking an important part in my graduate career.

Throughout graduate school, I have had the privilege to be a part of different collaborative efforts, through which I received regular advisement and guidance from some wonderful people. Most prominently, I want to thank Professor Mark Ediger from the University of Wisconsin-Madison. Much of my graduate work, including two of the chapters in this thesis, was in collaboration with him and his students. Even though I was not his student, he always provided thoughtful discussion concerning my project proposals and results, and took the time to Skype with me and his students to keep us on track and focused. The summer of 2014, I had the opportunity to work at the Institut Laue-Langevin in Grenoble, France. There I was able to try my hand once again at wet-lab work and I want thank Dr. Anne Martel, Dr. Yuri Gerelli, and Dr. Lionel Porcar for hosting me; also for their patience as I was reminded why I decided to go into computational work in the first place. I had the privilege to intern with IBM in the spring of 2017 at their facility in Almaden, CA, where I was under the advisement of Dr. Jed Pitera. I am thankful for the time he took out of his schedule to come up with a project for me to work on, check on me regularly, and involve me in his subgroup outings. Additionally, I want to thank Professor Sankaran Thayumanavan at UMass-Amherst for the guidance he had given to me and his students that culminated in the work of Chapter 4.

The backbone of those collaborations were the students doing the work with me. I would like to thank Yue Qiu, Dr. Poornima Rangadurai, and Dr. Diane Walters for their hard work ethic and the enthusiasm they brought to each project. It was a pleasure getting to work with and getting to know each of you over many random Skype calls and emails about research.

I want to thank all the current and former group members of the de Pablo group. They have truly made graduate school not only intellectually stimulating, but have provided great friendships and a family like atmosphere. I would like to highlight a few who were particularly influential in my development as a graduate student. Dr. Sadanand Singh, Dr. Devin Averett, and Dr. Aaron Fluitt helped me get started by providing example scripts, tutorials, and papers to read to get me on the ground running. If it weren't for Dr. Kyle Hoffmann's thorough scripts and advice on coding, I wouldn't have gained the programming skills that I have acquired over time. I am particularly thankful to Dr. Ivan Lyubimov who, as a post-doc, really helped me along as I started researching vapor deposited glasses and was always there to provide guidance and support. I'd like to thank Dr. Nick Jackson, especially for him adding the electron transport calculation to bring my ethylbenzene study home and for our mutual taste in terrible yet entertaining action movies. A special thanks to Alec Bowen, Josh Moller, and Dr. Tyler Roberts who made it especially difficult not to bring work home, as each were a room mate as well as a fellow group member at one point. I would like to also thank, in no particular order, the past and present group members I had the pleasure of knowing: Dr. Arnout Boelens, Prof. Jian Qin, Prof. Sumi Hur, Prof. Chi-cheng Chiu, Prof. Jonathan Whitmer, Dr. Grant Garner, Dr. Gurdaman Khaira, Dr. Abhijeet Joshi, Dr. Dan Hinckley, Dr. Gordon Freeman, Dr. Brandon Peters, Dr. Julian Helfferich, Dr. Michael McGovern, Dr. Alejandro Londoño, Dr. Monirosada (Sanaz) Sadati, Dr. Nader Taheri Qazvini, Dr. Mohammad (Amin) Rahimi, Dr. Hadi Ramezani-Dakhel, Dr. Marat Andreev, Dr. Yamil Colón, Dr. Mike Webb, Dr. Joshua Lequieu, Dr. Yongrui Su, Dr. Daniel Reid, Weiwei Chu, Ye Zhou, Ashley Guo, Emre Sevgen, Jiyuan Li, Cody Bezik, Phil

Rauscher, and last but not least Viviana Palacio-Betancur.

Lastly, but certainly not least, I would like to thank all my friends and family for their love and support. My parents may not understand how the graduate school process works, or much of scientific research in general, but they were always there to support me in what I endeavored in. My brothers and their families have always brought me great joy and helped get me through much in life. I also want to thank friends like Arin Greenwood, Dr. Aditya Gupta, Dr. Ben Conrad, Dr. Doug Stone, and Luke Kersting.

ABSTRACT

The homogeneous structure, and inherent tunability, of molecular glasses makes them particularly interesting for applications in material science and manufacturing. A glass is a nonequilibrium state where the timescales of relaxation far exceed those of observation, such that the atomic structure resembles that of a liquid but possesses the mechanical strength of a solid. In this dissertation, the focus is on the tuning and manipulation of organic glasses, particularly those formed by physical vapor deposition, as well as a polymer glass. Organic glass films formed by physical vapor-deposition have demonstrated remarkable thermophysical properties relative to those formed by conventional liquid cooling and aging techniques, and can be tuned by deposition parameters. In the first part of this work, we utilize a computational procedure that closely mimics the vapor deposition process to examine how the mobile surface of the film influences the characteristics of the resulting films. An all atom model of ethylbenzene was used to study the substrate temperature dependence of molecular orientation and, by treating ethylbenzene as a simple semiconductor, the corresponding effect vapor deposition has on charge transport properties of the film. This is the first computational atomistic study of an experimentally formed vapor-deposited glass, which demonstrated that with vapor deposition the charge transport properties can be tuned along with providing further evidence that surface relaxation during deposition dictates the resulting average molecular orientation within the film. We then use a coarse-grained model of azobenzene along with an algorithm imitating the photoisomerization reaction to explore the photostability of vapor deposited films. Our results, which are in qualitative agreement with experimental results for the azobenzene derivative disperse orange 37, indicate that the films formed with higher density also have a significant increase in photostability. Continuing the exploration of the photoisomerization response in a glassy medium, we demonstrate that the photoisomerization of a molecularly thin layer within a polymersome, which is assembled from a hydrophilic-azobenzene-hydrophobic diblock copolymer, can reversibly disrupt a glassy matrix to enable leakage in an otherwise sealed membrane via “photo-softening”.

Finally, we explore how the location of a ethynyl groups within molecular glass photoresist can affect the glass and structural properties of the material as well as potential confinement effects on the structure.

CHAPTER 1

INTRODUCTION

All the work presented in this thesis involves organic glassy systems. This chapter will give a brief description of what an organic glass is and why these materials are of interest within materials research and development. There will then be a discussion on "ultra-stable" vapor deposited glasses, which have been shown to produce highly desirable properties within certain organic glasses. Chapters 2 and 3 of this thesis are focused on studying the properties of these glasses and how they differ with respect to their liquid-cooled counterparts.

Photoisomerization, the reaction in which structural change between isomers is caused by absorption of a photon, is the main focus of Chapters 3 and 4. Particularly, the photoisomerization of azobenzene derivatives from the *trans* to *cis* conformation. Azobenzene derivatives have been used as molecular switches in many applications, here we are looking at its ability to either reversibly or irreversibly transform a glass matrix. In this chapter, a brief description of this "photo-softening" effect will be provided.

Chapter 5 focuses on molecular glasses considered for photoresists in the semiconductor industry. The molecules considered have the same molecular weight and only differ based on the location of three ethynyl groups, or tripled bonded carbon atoms. Glass properties depend on the stiffness and internal degrees of freedom within the molecules; thus by changing the location of the ethynyl groups and changing the rotational degrees of freedom or radius of gyration, the T_g of the material changes.

1.1 Organic Glasses

A simple definition of a glass is a nonequilibrium amorphous solid. It is nonequilibrium as the material is not in the thermodynamically favored state, but has become kinetically trapped. Unlike crystalline solids, a glass is amorphous in that there isn't a periodicity or long range order to the microscopic structure.[35] The most common method to form a glass is by cooling

a liquid below the melting point of the material at a rate fast enough to avoid crystallization. This so-called "super-cooled" liquid can remain in equilibrium for a brief time as the material is continued to cool; however, eventually the timescales of relaxation and rearrangement slow so dramatically that the material can no longer sample configurational space properly and becomes kinetically trapped and falls out of equilibrium. The temperature at which it no longer can remain in equilibrium is called the glass transition temperature, T_g. The glass formed and the T_g depend on the cooling rate used. Conventionally, T_g is consider the temperature at which the relaxation timescales are on the order of 100s. Despite the large timescales for relaxation, the molecules composing the glass will continue to slowly rearrange to approach the equilibrium state, that of the super-cooled liquid, through the process of "physical aging." However, this process, which usually involves the density and modulus increasing and improved thermal stability, changes at a logarithmic rate. For instance, to observe the same change observed from aging 1 hr to 100 hr one would have to wait another 10000 hrs.

Typically people associate the term "glass" to window glass, which is a silicate-oxide glass. However, organic glasses are used in food[152, 87], pharmaceuticals[164, 53, 80], and organic electronic devices[17, 133]. For example, the active layer of organic light emitting diodes (OLEDs) are an organic semiconducting glass formed via vapor deposition and used in most smart phone displays and organic photovoltaics are composed of organic glasses.[161] There are many applications where glasses are preferable over crystals. Unlike crystals, the composition of a glass can be widely varied which allows for homogeneous multicomponent films. Additionally, glasses are macroscopically homogeneous, whereas crystals tend to be macroscopically inhomogeneous with grain boundaries that can act as charge traps or lead to differences in device performance. Due to the nonequilibrium aspect of a glass, the glass formed is highly dependent on the process of formation, which can be taken advantage of for tuning towards desired properties. One method of preparation mentioned earlier is the process of vapor deposition, which, a little over a decade ago, was shown to be able to

produce glasses whose properties are similar to those that would require 100 to 100000 years of physical aging, depending on the method of extrapolation.[140, 40]

1.2 Vapor Deposited Glasses

Physical vapor deposition, PVD, is the process of building a film by attaining the vapor phase of the desired material under vacuum and allow it to condense onto a substrate. Vapor deposition had been used to prepare and study glasses for many year[106, 60], but it was not until the study conducted in Ref. 140 by my collaborators, the Ediger group at the University of Wisconsin-Madison, that PVD can be utilized to form exceptional glasses with densities, thermal stabilities, and moduli that were not practically attainable through conventional cooling and aging processes. This enhanced stability has since been observed for a variety of organic molecules, including, but not limited to, indomethacin[140, 170, 33, 120], a variety of alkylbenzenes[64, 63, 65, 19, 116, 83, 137], several tris-naphthylbenzene (TNB) isomers[31], intraconazole[50], and several organic semiconductors[6, 75, 29]. The stability of the glass formed in all instances is dependent on the substrate temperature, T_{s}, at which the films were deposited. The optimal range is typically between 0.8 to 0.9 T_{g}[40], and typically with lower T_{s} the glasses become less stable until they are relatively less stable than the liquid-cooled glasses. The current understanding of how these "stable glasses" are formed is via a surface equilibration mechanism. As the film is being formed, there is a thin layer at the top that is liquid-like in that the relax times are fast enough for the newly deposited molecules to properly sample configurational space and form more favorable states. As T_{s} the liquid layer at the top becomes smaller and the molecules have less time to equilibrate and at very low T_{s} or very fast deposition rates the molecules have no time to relax and form unstable assemblies. Studies have shown that the surface diffusion can be up to 10^8 times faster than bulk diffusion at T_{g}.[169, 95] There have been studies to show that molecules with comparable surface and bulk diffusion are not good stable glass formers.[18, 10]

Simulation groups, particularly our own, have developed methods for probing glassy

dynamics and to study this effect from vapor deposition. The first simulations were performed by Sadanand Singh with an all-atom model of trehalose[134] and then with the Kobb-Anderson glass model[135]. To mimic the deposition process a substrate is created of Lennard-Jones beads randomly arranged within the same plane and then constrained to their initial position by strong harmonic springs. Iteratively new molecules are added slightly above the top of the film at high temperature and then slowly cooled to the desired substrate temperature and equilibrated at the new temperature for a short period of time. An energy minimization is then performed over all molecule positions and then then the next iteration is initialized. This process can be thought of as playing the game Tetris, slowly building up the film, and has been shown to provide results that qualitatively agree with the trends observed in experiments.

Experimental studies have shown that the vapor deposition process can influence the average molecular orientation within the glass, leading to formation of anisotropic films.[28, 26] This is not surprising as glasses are sensitive to the method of preparation and vapor deposition is anisotropic in that it is grown in a single direction. For several different semiconducting molecules, it has been demonstrated that PVD films have a degree of anisotropic orientation that depends on molecular shape and deposition conditions, and that this anisotropic ordering can improve the charge carrier transport properties relative to isotropic films.[162, 161] Simulations of vapor deposition of short polymeric molecules have also shown that physical vapor deposition leads to stable anisotropic glasses.[85] More recent studies of organic semiconducting PVD glasses[29] and intraconazole[50] have shown that the average molecular orientation can be systematically tuned as a function of T_{s}, while maintaining the enhanced stability observed from PVD.

This anisotropic ordering within the glass films is consistent with the picture of the stability gained by PVD is due to a thin liquid layer during film formation. The anisotropy is thought to arise from the interfacial ordering that occurs at the vacuum-liquid interface. This ordering is trapped at different states depending on the T_{s} and deposition rate.[29, 88]

The degree of structural ordering observed in PVD glasses is currently thought to be a feature of the vapor deposition process, but not necessary for enhanced stability. For example, vapor deposited glasses of a mostly spherical molecule, tetrachloromethane, form relatively stable glasses and are expected to form isotropic materials.[20] Similarly, simulated vapor-deposited glasses of spherical particles[89, 117] exhibit significant kinetic stability and do not exhibit any signs of ordering beyond those observed in liquid-cooled glasses.

Chapter 2 is the first all-atom simulation study of vapor deposition of a molecule that has been shown to form stable glasses via PVD. The study of trehalose mentioned earlier was never confirmed with experiments. First agreement was established between several simulated and experimental macroscopic observables, and then the simulations were used to examine the substrate temperature dependence of molecular orientation that had been observed experimentally for larger molecules and coarse-grained models. The results indicate that ethylbenzene glasses are anisotropic, depending upon substrate temperature, and that this dependence can be understood from the orientation present at the surface of the equilibrium liquid as hypothesized. By treating ethylbenzene as a simple model for molecular semiconducting materials, a quantum-chemical analysis was used to show that the vapor deposited glasses exhibit decreased energetic disorder and increased magnitude of the mean-squared transfer integral relative to isotropic, liquid-cooled films; an effect that is attributed to the anisotropic ordering and increased density of the molecular film.

Chapter 3 is a collaborative study to investigate the effect vapor-deposition and the enhanced stability associated with it can have on the reactivity within the film. Particularly, we investigated the ability of the composing molecules to undergo the photoisomerization reaction. Disperse Orange 37 (DO37), an azobenzene derivative, is studied as a model system in the experiments. Photostability is assessed through changes in the density and molecular orientation of glassy thin films during light irradiation. By optimizing the T_{s} used for deposition, we were able to increase photostability by a factor of 50 relative to the liquid-cooled glass. Photostability correlates with glass density, with density increases of up to

1.3%. I developed a coarse-grained model to perform molecular dynamic simulations, which utilizes an iterative method to mimic the photoisomerization reaction, also indicated that glasses with higher density have substantially increased photostability. These results provide insights that may assist in the design of organic photovoltaics and light emission devices with longer lifetimes. The results in Chapter 3 are related to another glass phenomenon of "photo-softening" that is observed with photoisomerization in polymer glass systems.

1.3 Photo-softening of Glasses

The photo-induced *trans-cis* isomerization of azobenzene and its derivatives has been utilized as a trigger in applications ranging from molecular machines[3, 101] to holographic recording devices[66]. One particular feature of azobenzene systems is the process of photo-softening in polymer glasses. In these systems, azobenzene derivatives are incorporated in either the side-chains or backbone of the polymer; upon irradiation, the isomerization reaction can reduce the modulus of the material and induce a flow within the glassy material.[79, 42] During this process, the viscosity of a polymer glass can be lowered by almost a factor of ten.[129, 73] There is an ongoing debate as to whether the mechanism at work is an isotropic process of "photofluidization" or an anisotropic mechanism where a mechanical stress is imposed on the glass due to the reorientation of azobenzene units.[124, 129] In either scenario, these observations allude to an ability to control the viscosity and material properties such as free volume and shape in polymer glasses.[103, 157] Chapter 3 demonstrates that the cyclic process of *trans*→*cis*→*trans* isomerization enacted can irreversibly lower the density and change average molecular orientation in an ultra-stable glass films of DO37.

In a recent report, photo-softening was used in vesicles to trigger an order-disorder transition in the liquid crystal composite of the membrane. By enacting the isomerization process, proton transfer was observed to increase through the vesicular membrane.[158] In Chapter 4, we utilize the photo-softening effect to control the mobility within a thin layer of polymer glass. Unlike the majority of the previously mentioned studies, a single azobenzene unit is

incorporated into the backbone of an amphiphilic diblock copolymer, PEG-azo-PLA, rather than attached to a side-chain, which is located at the interface of hydrophilic polyethyleneglycol (PEG) and hydrophobic poly-DL-lactide (PLA) blocks. We demonstrate that with this assembly we are able to reversibly increase the mobility and disrupt the packing of the glassy PLA layer. A previous study has shown that a similar assembly forms vesicles and can be used for nano-encapsulation. In that study, the load was released through environmental changes causing the vesicle to rupture.[78] By taking advantage of the photo-softening affect in Chapter 4, the mobility in the sealed hydrophobic layer can be increased in a controlled manner, which could lead to controlled leakage of the membrane without dissociating the vesicular structure.

CHAPTER 2

INFLUENCE OF VAPOR DEPOSITION ON STRUCTURAL AND CHARGE TRANSPORT PROPERTIES OF ETHYLBENZENE FILMS

In this chapter we further delve into the connection that was starting to be draw between the surface relaxation during film formation and the resulting average orientation within the bulk of the film. Prior to this work, trehalose had been the only all-atom model utilized in simulations of vapor deposition, which has not been shown experimentally to form stable glasses[134]. An effect on molecular orientation was observed in that study; however, this was not further investigated until a coarse-grained model was used.[88] Here we performed a comprehensive all-atom study using an experimentally established stable glass former, ethylbenzene. Unlike the coarse-grained model used in Ref. 88, a distinct head and tail direction can be defined, which allows us to look more closely at the rotational relaxation of a molecule at the film surface and the resulting molecular orientation. We do observe a favored orientation with the ethyl groups pointing towards the vacuum at the interface. Furthermore, ethylbenzene can be treated as a simple organic semiconductor to investigate the effect vapor deposition has on the charge transport properties of the film. All the electronic structure calculations and analysis were performed by Dr. Nicholas Jackson, whereas I performed all the other simulations and analysis.

2.1 Introduction

Glasses are typically formed by cooling a liquid at a sufficiently fast rate to avoid crystallization. As the liquid approaches the glass transition temperature, T_g, the characteristic relaxation times and viscosity increase substantially, and eventually the supercooled liquid falls out of equilibrium. The properties of the resulting glass, such as its kinetic stability and density, depend on the cooling rate. Such properties can evolve over time by letting the material relax towards equilibrium, a process referred to as "physical aging". Physical vapor deposition (PVD), a process in which molecules are deposited onto a substrate held at a temperature below T_g, has been shown to create glass films with enhanced kinetic stability. For some materials, the properties of PVD glasses are in fact comparable to those expected of highly aged, liquid-cooled glasses[140, 74, 142] This enhanced stability has been observed for a variety of organic molecules, including indomethacin[140, 170, 33, 120], a variety of alkylbenzenes[64], toluene and ethylbenzene[63, 65, 19, 116, 83, 137], several tris-naphthylbenzene (TNB) isomers[31], and several organic semiconductors[6, 75, 29].

In recent years, the discovery of these highly stable glasses has motivated simulation efforts to create stable glasses in silico. Using a protocol based on the vapor deposition process, a series of simulation studies have examined the increased stability of vapor deposited glasses relative to conventional glasses, and the influence of the process itself. That work has focused on relatively simple models that are known to be good glass formers. These include the so-called Kob-Andersen model[135, 89, 57], short-chain coarse-grained polymers[85], and a 2D version of the Kob-Andersen model[117].

Experimental studies have shown that the vapor deposition process can in some cases influence the average molecular orientation within the glass, leading to formation of anisotropic films.[28, 26] In particular, Yokoyama and others have demonstrated for several different semiconducting molecules that PVD films have a degree of anisotropic orientation that depends on molecular shape and deposition conditions, and that this anisotropic ordering can improve the charge carrier transport properties relative to isotropic films.[162, 161] Simula-

tions of vapor deposition of short polymeric molecules have also shown that physical vapor deposition leads to stable anisotropic glasses.[85] More recent studies of organic semiconducting PVD glasses[29] and intraconazole[50], a smectic liquid crystal, have shown that the average molecular orientation can be systematically tuned as a function of the substrate temperature, T_s, while retaining the enhanced density and kinetic stability that is imparted by the PVD process. The anisotropic ordering within the glass films is now thought to arise from the interfacial ordering that arises at the vacuum-liquid interface; that order is trapped in the glassy film as it is grown by PVD, leading to materials whose structure in the glass is different from that obtained in the bulk of liquid cooled glasses.[29, 88] The degree of structural ordering observed in PVD glasses is currently thought to be a feature of the vapor deposition process, but not necessary for enhanced stability. For instance, vapor deposited glasses of tetrachloromethane, which is a mostly spherical molecule, form stable glasses (with high onset temperatures relative to the liquid-cooled material) and are expected to form isotropic materials.[20] Similarly, simulated vapor-deposited glasses of spherical particles[89, 117] exhibit significant kinetic stability and do not exhibit any signs of ordering beyond those observed in liquid-cooled glasses.

Molecular simulations have provided important insights into the structure and properties of vapor deposited glasses and into key features of the PVD process itself. However, all simulations studies to date have focused on simplified models that do not exhibit the structural richness of realistic, atomistic systems. An exception is provided by an early study of trehalose, which revealed significant anisotropy in a stable glass. Trehalose, however, has not been considered in experimental PVD processes, partly because it can easily crystallize, and it is therefore difficult to interpret the results of that study. In this work, we investigate the formation of glasses by physical vapor deposition for ethylbenzene (EB), and we examine its effects on molecular orientation and, importantly, on the corresponding charge transport descriptors that would be relevant for semiconducting applications. Ethylbenzene is one of the smallest PVD stable glass formers that have been studied in the literature. Care-

fully generated experimental data for this molecule are now available from multiple research groups,[63, 65, 19, 116, 83, 137, 14] making it a good candidate for an in-depth computational study of an atomistic vapor deposited glass. Note, however, that structural studies have not been performed before on vapor deposited films of ethylbenzene; it is therefore not known whether the resulting materials are isotropic or not. Our simulations provide evidence suggesting that the vapor deposition process can in fact be used to tune molecular orientation even in slightly asymmetric molecules, such as ethylbenzene. Along with those findings, we also examine the corresponding effect that PVD growth can have on the charge-transport properties of the resulting glassy films.

It is important to note that ethylbenzene itself is not a practically useful semiconducting molecule. However, from a theoretical point of view, it serves as an excellent model system for examining the impact of variable morphologies on relevant charge transport parameters; ethylbenzene's conjugated ring and small alkyl side-chain can be treated as a minimal model for the design motifs of common molecular semiconductors[96]. Given the promise of vapor deposition to form stable glasses of organic semiconducting molecules, it is important to understand the impact that subtle changes in morphology may have on molecular-scale descriptors of charge transport. Since the majority of non-crystalline molecular semiconductors operate in the activated hopping regime of charge transport[9], which can be accurately described by a non-adiabatic theoretical framework[70], the two relevant parameters that are most strongly influenced by morphology are the molecular site-energies and transfer integrals between molecules[8]. The local site-energy of a molecule, determined by the orientation of nearest-neighbor molecular dipoles[36], impacts the density of states through which charge transport occurs. If this density of states is too broad, due to large site-energy disorder, charge transport is inhibited by localization into low-energy trap states[9]. Similarly, the transfer integral (electronic coupling) between the valence orbitals of two neighboring molecules dictates the maximum rate of charge hopping between those molecules; if the mean-alignment of neighboring molecules results in poor molecular orbital

overlap, the maximum possible rate of charge hopping decreases, and charge transport is hindered[145]. While it is heuristically known that one can strongly influence these parameters via changes in morphology, a rational and systematic modification of these parameters via deliberate changes in processing parameters is difficult to achieve. Here we couple the ability to control orientational order in molecular simulations with a quantum-mechanical analysis of site energies and transfer integrals to understand the impact of PVD on charge transport parameters of stable glasses.

2.2 Results and Discussion

Experimental observation timescales for glass behavior are typically on the order of seconds or longer, whereas for all-atom simulations, the accessible timescales are on the order of nanoseconds. Due to this discrepancy in timescales and rate dependence of glass properties, in simulations it is better to base the substrate temperatures for vapor deposition on the lowest practical simulated fictive temperature T_{f} rather than the conventional T_{g} for the material. The fictive temperature is given by the intersection of the equilibrium liquid property of interest (e.g. enthalpy or density) extrapolated to lower temperatures, and the glass line property extrapolated to higher temperatures. A total of three cooling rates were considered here, namely: 10K/ns, 5K/ns, and 1K/ns. The intensive per atom potential energy U_{atom} was used to define T_{f}, as it exhibits a linear temperature dependence for both the glassy and liquid states. The change in slope when the liquid falls out of equilibrium is subtle; SI-Figure 2.8c displays the temperature range over which the transition occurs. A dependence of about 6 K per decade decrease is observed in T_{f} as the rate is decreased for the three rates considered. The effective glass transition temperature T_{g} in this study is defined as the T_{f} for the slowest cooling rate, which is 146 K (marked by grey lines on SI-Fig. 2.8). The density, ρ_{bulk}, and the average Debye-Waller factor for the middle bulk region (defined in the Methods section) are shown in panels **(a)** and **(b)**, respectively, in SI-Fig. 2.8. Glassification is also observed in these two properties, where the rate of change is considerably smaller once

the material becomes glassy on the time scale of our simulations for both. The super-cooled liquid deviates from the equilibrium line at higher temperatures as the rate increases, and becomes trapped in a lower-density and higher-energy state.

In order to validate the model, the conventional T_{g} value can be estimated via extrapolation. Conventionally, the glass transition is defined as the temperature at which the structural relaxation reaches $\tau_\alpha = 100$ seconds. Within the domain of $10^{-14} < \tau < 10^2$ and $T > T_g$, the relaxation times τ and the viscosity η follow a Vogel-Fulcher-Tammann (VFT) expression of the form

$$\log(\tau) = A + \frac{B}{T - T_0}. \tag{2.1}$$

SI-Figure 2.9 shows the rotational auto-correlation for the bulk region of the films in the temperature range from 150 K up to 350 K. The VFT expression requires that the liquid films be fully relaxed, and, as evident in SI-Figure 2.9, 150 K is the lower limit accessible to simulations. A stretched exponential was fitted to each rotational auto-correlation function, leading to a relaxation time τ_{rot} (the fit parameters are given in SI-Table 2.1). The τ_{rot} relaxation times were fitted to the VFT relation (SI-Fig. 2.10), giving $A = -11.98$, $B = 206.8$ K , and $T_0 = 112.8$ K. Extrapolation of the relaxation times to $\tau_{\mathrm{rot}} = 100$ seconds yields a $T_g \approx 128$ K. This value is not too different from the reported glass transition temperature for ethylbenzene of 115 K.[63, 116, 19] The fragility of the material can also be determined from the fit parameters according to

$$m = \frac{(2 - A)\big(B + T_0(2 - A)\big)}{B}, \tag{2.2}$$

which gives a value of $m = 121$ by extrapolation. These values are in reasonable agreement with those calculated by Chen *et al.* in Ref. 19 who measured the dielectric relaxation of EB. In their results, a fit of $A = -15.0$, $B = 344.4$ K, $T_0 = 95.5$, and $m = 97.5$ were obtained. Moreover, Chen *et al.* observed the temperature dependence of the dynamics does not follow a single VFT law over the entire range of temperatures, such that temperatures

closer to experimentally defined T_g, which are not accessible to simulations, would lead to improved agreement. Note that τ_{rot} is already on the order of 100 nano-seconds at $T = 150$ K, which is comparatively the same order of magnitude as the longest practical runtime for all-atom films. The relaxation rate for films any lower in temperature would be far too large to equilibrate on practical timescales, which is in accordance with our lowest fictive temperature and effective T_g of 146 K.

2.2.1 Enhanced stability

Vapor-deposited films of ethylbenzene were generated according to the scheme outlined in the Methods section onto substrates with temperatures ranging from 95 K up to 145 K, which is just below the effective T_g of our system (146 K). In order to assess the relative stability of the various films, the per atom inherent structure energy E_{IS} was calculated for the bulk region of each film. The energy of the entire system was minimized after the film was cooled to 70 K at a rate of 10 K/ns, in order to allow the film to relax in the x and y dimensions prior to quenching. As illustrated in Figure 2.1, a linear fit to E_{IS} relative to $\log_{10}(q_c)$ was used to extrapolate what the corresponding cooling rate would need to be in order to achieve the E_{IS} of each vapor deposited film. The E_{IS} decreased approximately 7.7×10^{-3} kcal/(mol·atom) per decade decrease in cooling rate. A similar calculation was performed on ρ_{bulk}, as discussed in the supporting information. Our results indicate that all the vapor deposited films exhibit a lower E_{IS} than the liquid-cooled glass. Note that PVD films are closely clustered together around an estimated cooling rate of 0.1 K/ns, which would take on the order of months to years of simulation time to produce by liquid cooling.

To further assess the relative stability of the films, we subjected them to a heating cycle at a rate of 5 K/ns. The temperature at which the film begins to return to the equilibrium liquid state, referred to as the onset temperature and denoted by T_{on}, is a measure of kinetic stability. For the liquid-cooled glass, this T_{on} is 159 K in Fig. 2.2. All the PVD glasses prepared here have higher T_{on}, with values in the vicinity of 170 to 172 K for all deposition

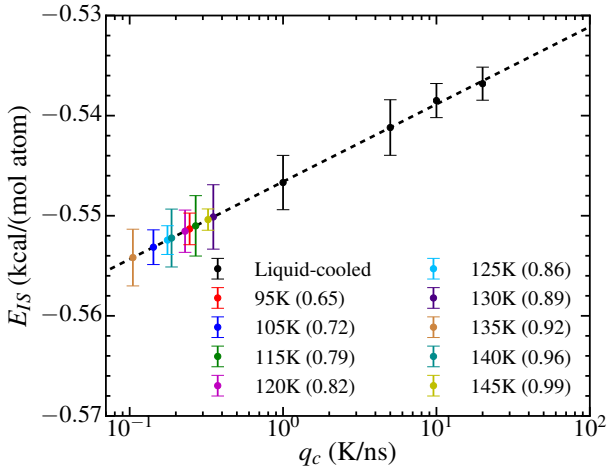

Figure 2.1: The intensive inherent structure energy, E_{IS}, for the bulk region. The black points are calculated from the liquid-cooled glasses as a function of cooling rate, q_{c}. The vapor deposited glasses (colored points) are plotted by the predicted q_{c}, assuming a linear relation between E_{is} and the order of q_{c}(dashed line). Error bars are calculated from the standard deviation of three samples for vapor deposited films and five samples for the liquid-cooled.

temperatures considered here as seen in SI-Figure 2.11. This finding is consistent with the enhanced E_{IS} and ρ_{bulk} observed for PVD films. For the sake of comparison, T_{s}=120 K is the only PVD glass shown in Fig. 2.2. The PVD glass loses the enhanced stability upon entering the liquid state and has a T_{f} of around 148 K upon cooling, as was observed previously for q_{c}= 5 K/ns.

2.2.2 Structural orientation

The orientation of ethylbenzene molecules is quantified in terms of the vector pointing from the carbon atom para to the ethyl group to the α-carbon of the ethyl group (SI-Fig. 2.18a). To characterize the molecular orientation within the bulk region of the films, we relied on two orientational order parameters defined by the first and second Legendre polynomials

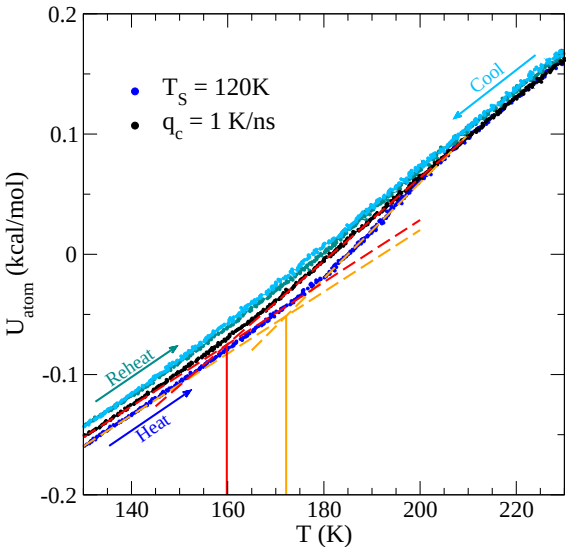

Figure 2.2: T_{on} comparison of the slowest cooled glass, q_{c}= 1 K/ns, and the films deposited at $T_{\text{s}} = 120$ K. The darker blue and the black curves represent the intensive potential energy of the film during a heating run at a rate of 5 K/ns. The films were then cooled and reheated at the same rate (light blue and dark cyan). The dashed lines are linear extrapolations from the glass line, and from the temperature range where the glass returns to an equilibrium super-cooled liquid. Red and orange solid lines mark the onset temperature T_{on} for the liquid-cooled glass and vapor deposited glass, respectively.

given by

$$P_1 = \left\langle \mathbf{n} \cdot \mathbf{n_z} \right\rangle_{\text{bulk}} = \left\langle \cos(\alpha) \right\rangle_{\text{bulk}} \tag{2.3}$$

$$P_2 = \left\langle P_2 \left(\mathbf{n} \cdot \mathbf{n_z} \right) \right\rangle_{\text{bulk}} = \frac{3}{2} \left\langle \cos^2(\alpha) \right\rangle_{\text{bulk}} - \frac{1}{2} \tag{2.4}$$

where the dot product is between the unit vector along the molecular axis, $\mathbf{n}$, and the unit normal to the substrate, $\mathbf{n_z}$, as shown in SI-Fig. 2.18a. The dot product is given by the cosine of the angle α between the molecular axis and $\mathbf{n_z}$, and averaging was performed over all molecules within the middle bulk region of the film. The two order parameters provide complementary information about the average molecular orientation within the film. P_1 identifies if the molecules are pointed perpendicular to the substrate with the ethyl group pointed to the surface ($P_1 = 1$) or towards the substrate ($P_1 = -1$); however, a value of 0 can either mean that the film is isotropic, or that molecules are parallel to the substrate.

Parameter P_2 indicates if the molecule is generally perpendicular to the substrate ($P_2 = 1$), parallel ($P_2 = -0.5$), or isotropic ($P_2 = 0$). Thus, P_1 elucidates whether $P_2 = 1$ means that molecules are pointed up or down, and P_2 determines whether $P_1 = 0$ means that the film is isotropic or parallel.

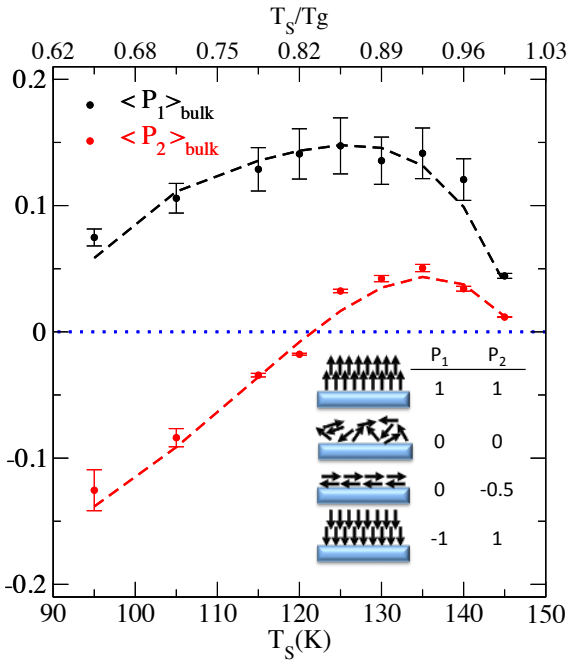

Figure 2.3: Bulk averages for $P_1 = \cos(\alpha)$ (black) and $P_2 = \frac{1}{2}\left(3\cos^2(\alpha) - 1\right)$ (red) as a function of substrate temperature, T_s, where α is the angle between the normal of the substrate and the orientational vector as shown in SI-Figure 2.18a. The dashed lines are to guide the eye and the dotted blue line is 0 to distinguish deviation from random for both P_1 and P_2. The insert describes the molecular orientations corresponding to the different P_1 and P_2 values.

Figure 2.3 shows the substrate temperature dependence of the average molecular orientation within the prescribed bulk region. Consistent with experimental measurements and results from coarse-grained simulations of vapor deposited films, that dependence is found to be non-monotonic. When T_s is slightly below T_g, in this case 120 K $< T_\mathrm{s} < T_\mathrm{g} = 146$ K, there is a slight tendency for the molecules to orient perpendicular to the substrate ($P_2 > 0$) such that the ethyl groups are pointed towards the surface ($P_1 > 0$). For $T_\mathrm{s} < 125$ K, the molecules start to orient more parallel to the substrate, with $P_2 < 0$ and P_1 decreasing towards zero after 125 K.

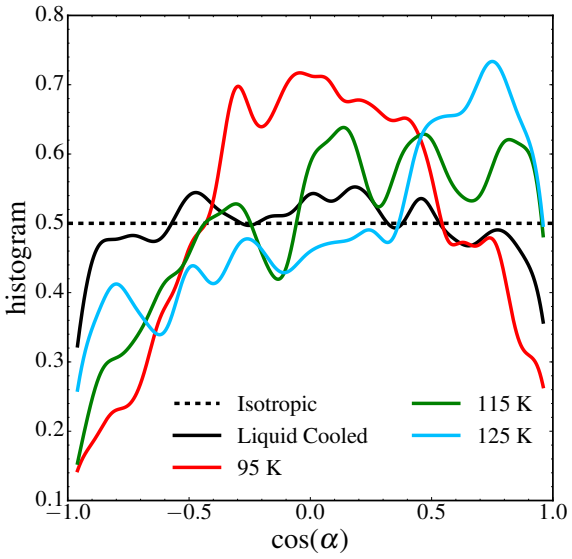

Figure 2.4: Distribution of $P_1 = \cos(\alpha)$ values in the bulk of the liquid-cooled glass (black), where q_c= 1K/ns, vapor deposited glasses for T_s values of 95 K, 115 K, and 125 K (colored). Calculated using a Gaussian kernel density estimation (bandwidth = 0.10).

Figure 2.4 provides the full $\cos(\alpha)$ distribution for the liquid-cooled glass and a subset of the PVD glasses (a larger subset provided in SI-Fig. 2.14). For reference, a dotted line is shown to illustrate the uniform distribution that is expected for a completely isotropic film. The liquid-cooled glass exhibits a relatively uniform distribution, within some sampling error, as expected. For all PVD glasses the ethyl groups point away from the substrate to some degree. For the films just below T_g, there is a tendency towards slightly positive values, with a peak around $\cos(\alpha) = 0.75$ and monotonic decrease for lower cosine values as is evident for T_s= 125 K. For the films deposited at the lowest substrate temperature, 95 K, the peak is almost symmetric at $\cos(\alpha) = 0$. This is indicative of the molecules being oriented in the plane of the substrate, with very little perpendicular orientation. The substrate temperature T_s=115 K represents the transition from the positively skewed distribution to the distribution of the lower T_s, with the peak located at zero with a relative plateau from 0 to 1.0.

In a previous coarse-grained study, Lyubimov *et al.* connected this T_s dependent molecular orientation to features observed at the liquid-vacuum interface.[88] We performed a similar analysis with ethylbenzene, but we focused on the rotational correlation during the deposition process with respect to the molecular orientation in the immobile state. In other

words, where in the previous study the correlation was based on P_2, here we define for each molecule i a quantity

$$p_i(t) = \mathbf{n}_i(t) \cdot \mathbf{n}_i^f = \cos(\delta_i), \tag{2.5}$$

where $\mathbf{n}_i(t)$ is the molecular orientation unit vector of molecule i at time t, $\mathbf{n}_i^f$ is the orientation of the final immobilized state, and δ_i is the angular displacement between them. The average rotational correlation with respect to $\mathbf{n}_i^f$ was calculated over the bulk molecules by

$$p_1(t) = \frac{1}{N_b} \sum_{i=1}^{N_b} p_i(t_i + t), \tag{2.6}$$

where t_i denotes the moment in time when molecule i was deposited on the free surface. The averaging was done over all molecules in the middle bulk region at the end of deposition, N_b. Similarly, the average depth into the film at time t since deposition was defined by

$$\langle z_{\text{surf}}(t) \rangle = \frac{1}{N_b} \sum_{i=1}^{N_b} z_{\text{interface}}(t_i + t) - z_i(t_i + t), \tag{2.7}$$

where $z_{\text{interface}}(t_i + t)$ is defined by where the density drops to 50% of the bulk value in the z dimension and $z_i(t_i + t)$ is the z location of molecule i.

By plotting $p_1(t)$ with respect to $\langle z_{\text{surf}}(t) \rangle$ in Fig. 2.5a, we get the average rotational correlation to the final immobilized orientation relative to film depth. All PVD films, except for those deposited at the two coldest T_{s}, start with zero or near-zero correlation to the final orientation. In accordance with what was observed for coarse-grained molecules Ref. 88, as the molecules become more deeply embedded into the film, the rotational correlation to the glass state $p_1(t)$ smoothly approaches unity. The curve shifts to the left as T_{s} is lowered, indicating that the molecular orientation becomes frozen-in at shallower depths, and thus each molecule has a shorter period of time from when it is first introduced to when it is locked into the immobilized glassy state. For instance the films with $T_{\text{s}} = 95$ K or 105 K are shifted such that the initial correlation value is as high as 0.25 at $\langle z_{\text{surf}}(t) \rangle \approx 0$. The immobilized

orientation of the molecules deposited onto these films is correlated to the orientation of the molecules when they come into first contact with the film.

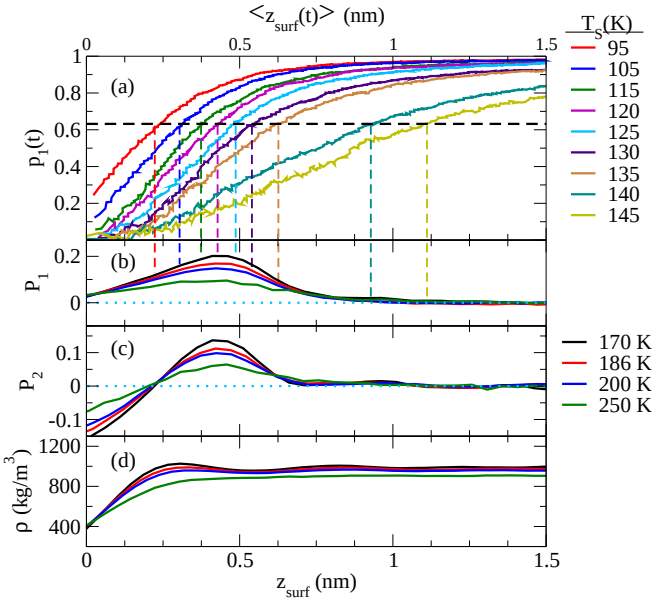

Figure 2.5: The top panel **(a)** is the correlation function for molecular orientation during deposition, $p_1(t)$. The function is shown for all substrate temperatures. The lower panels **(b, c** and **d)** contain data for the equilibrium liquid at four different temperatures: 170K (black), 186K (red), 200K (blue), and 250K (green). The panels **(b)**, **(c)**, and **(d)** display relative to the distance from the surface of the film, z_{surf}, the orientation parameters P_1 and P_2 as well as the density, respectively. The dashed lines from panel **(a)** to panel **(b)** mark the depth in the equilibrium liquid that the corresponding correlation function $p_1(t)$ has a value of $(1 - 1/e) = 0.632$ for each T_{S}.

Keeping with the procedure outlined by Lyubimov et al., Ref. 88, we define a rotational arrest time, t_a, through the relation $1 - p_1(t_a) = 1/e$ (horizontal dashed line of Fig. 2.5a). The distance from the free surface at which this occurs is denoted by $z_a = \langle z_{\text{surf}}(t_a) \rangle$. For each of the PVD glasses, the corresponding z_a is marked by a vertical dashed line in Fig. 2.5a (colored according to T_{S}). This gives a distance into the film at which the molecules become arrested, and thus a measure of how thick the mobile layer is during the vapor deposition process. There is a sudden shift between $T_{\text{S}} = 130$ K and $T_{\text{S}} = 140$ K due to the exponential temperature dependence of glass relaxation (SI-Figure 2.13).

Focusing on the equilibrium liquid films of ethylbenzene, there is a notable orientation preference at the vacuum-liquid interface, as was observed for the coarse-grained model and

atomistic TPD simulations. Figure 2.5(b, c, and d) show, respectively, the P_1 and P_2 order parameters and the density, ρ, relative to the distance from the free interface, z_{surf}, for films held at four different temperatures above the effective T_{g}. As observed in previous studies, the density is relatively featureless, with a uniform profile prior to a monotonic decay at the interface, whereas P_1 and P_2 reach a maximum at a depth of about 0.4 nm, or half a molecular length. Right at the free surface, P_1 is near zero and P_2 is negative, indicating that the molecules are preferentially aligned parallel to the surface at first contact. For $z_{\text{surf}} \geq 0.8$ nm, or slightly larger than one molecular length, $P_1 = P_2 = 0$, indicating that molecular orientations are random for the bulk of the film. Between the free surface and 0.4 nm, P_2 goes from negative to slightly positive and P_1 becomes increasingly significant, Fig. 2.5(b)-(c). In this region, the molecules go from a preferential parallel orientation to one that is slightly oriented with the ethyl groups pointing towards the vacuum region. Deeper into the film, where 0.4 nm $< z_{\text{surf}} <$ 0.8 nm, both P_1 and P_2 decrease towards zero, indicating that the preferential order decays and the material becomes isotropic at these depths. The deviation from isotropic for P_1 and P_2 as $z_{\text{surf}} \to 0$ begins at the same point for each temperature, and the peak z_{surf} for both order parameters remains the same. Moreover, P_2 switches sign and thus become parallel to the substrate at the same depth, for all consider temperatures refer to Fig. 2.5c. However, as observed for the coarse-grained model, the height of the peak in the order parameters increases as the temperature approaches T_{g}.

Following the mechanism proposed in Ref. 88, we connect the z_a to the values of P_1 at the same depth into the film (dashed lines from panel **(a)** to **(b)** in Fig. 2.5). In Figure 2.6, we compare the values of P_1 for each T_{s} (black) with the values for $T = 170$ K corresponding to z_a defined by either $1 - p_1(t_a) = 1/e$ (red) or $1 - p_1(t_a) = 0.5$ (blue). All curves have relatively the same shape, though the predicted values for $1/e$ are shifted to the left and peak at 125 K whereas the measured values peak at 120 K. Defining z_a based on $1 - p_1(t_a) = 1/e$ is rather arbitrary, though inspired by typical exponential decay. This value of $1/e$ could be shifted in order to more properly fit the measured data, but the relative correlation between

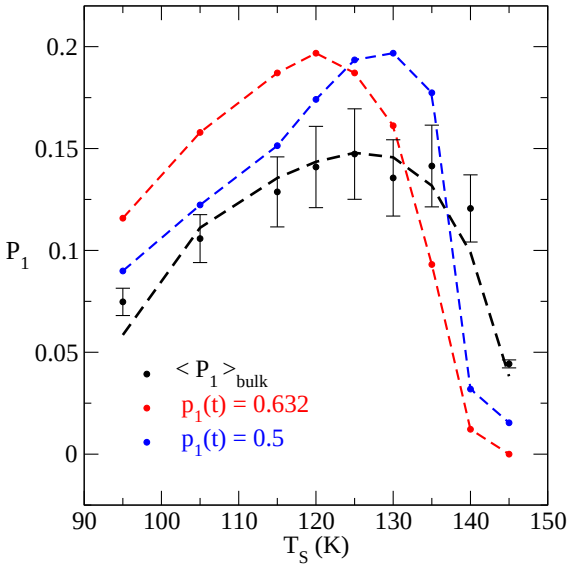

Figure 2.6: The value of P_1 from the 170K equilibrium liquid at the z_{surf} where $p_1(t) = (1 - 1/e) = 0.632$ (red) and 0.5 (blue) for the given substrate temperature from panels **(a)** and **(b)** Figure 2.5.

the orientation at the free surface of the film and the liquid and what is observed in the PVD glasses would remain. For instance, z_a based on $1 - p_1(t_a) = 0.5$ provides a similar peak position, thus the corresponding curve is in better agreement with the observed P_1 values (Fig. 2.6 blue). We also note that the analysis outlined above and shown in Figure 2.6 is more clearly manifest on P_1 than it is on P_2.

The previous characterizations neglected to address a component of structural ordering crucial to charge transport: the orientational correlations between neighboring molecules. The relative orientation of the pi-systems for two ethylbenzene molecules, described by the normal vector of each benzene ring, will, when taken in conjunction with their separation distance, be directly related to the magnitude of the electronic transfer integral.[145] To examine these local correlations, we plotted the alignment probability as a function of neighbor distance (SI-Fig. 2.15). While from SI-Figure 2.15 it is apparent that there is a slight enhancement in the ordering of local molecular orientations for the 120K PVD film relative to the liquid-cooled film, the change is very subtle. Whereas in more practical molecular semiconducting molecules we expect a stronger correlation due to pi-stacking effects, for

benzene, it is well-known that the pi-stacking configuration is not a global minimum energy configuration relative to the "T-structure", and many competing minimum energy configurations exist.[136] Consequently, there is no expectation of pi-stacking being the deeper energy minimum configuration within the stable glasses.

To further explore the nature of the orientational correlation networks within the films, we have used a graph-theoretical approach inspired by previous work [68] and constructed adjacency matrices using correlation functions between neighboring ethylbenzene molecules. By examining the eigenvalues of the corresponding Laplacian matrix, we use the algebraic connectivity as a measure of structural correlations within these graphs.[98] As observed in the SI, the enhancement of the graph's connectivity for the 120K PVD film is slightly increased relative to the liquid-cooled film, but the effect is within the error bars of both results. In summary, a slight enhancement of local orientational correlations between neighboring pi-system normal vectors is observed, though it is not a priori expected that this effect be large for this system, whereas it would be expected to be much larger for practical molecular semiconductors.

2.2.3 Charge Transport

Figure 2.7a shows the distribution of site energies in ethylbenzene for the vapor-deposited glass at 120 K normalized to the mean site-energy value, and a similar plot is provided in SI-Figure 2.16a for the liquid-cooled glass (q_c= 1 K/ns). The distributions fit well to a Gaussian distribution of site-energies, as is commonly considered in organic semiconducting materials.[43] Fitting the standard deviation of the site-energies yields a site-energy disorder parameter of 222 ± 2.6 meV for the liquid cooled glass, nd 201 ± 1.3 meV for the vapor-deposited glass, using a simple bootstrapping analysis for the error. While this difference appears small, it is quite consequential, particularly given the fact that the stability and orientational effects in simulated systems are significantly less than experimentally observed, that ethylbenzene is a relatively non-polar molecule, and that actual organic semiconducting

molecules of relevance will be significantly larger, thus exhibiting greater potential for orientational preferences. As such, this ≈ 20 meV difference in energetic disorder is considerable. Typical values of the site-energy disorder range between 0 and 300 meV, making this 10% change for ethylbenzene an important consideration for molecular design, especially provided that larger, more anisotropic molecular semiconductors used in practical applications should exhibit larger orientational preferences than our minimal ethylbenzene model.[96]

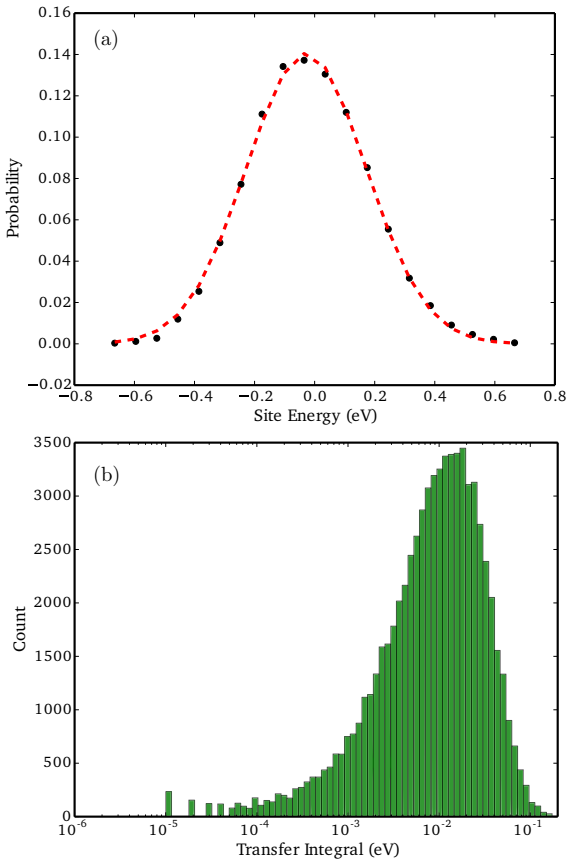

Figure 2.7: Histograms of the **(a)** molecular site-energies in eV and **(b)** the transfer integrals (eV) for the 120K vapor-deposited glass.

Figure 2.7b shows the distribution of transfer integrals for the vapor-deposited glass at 120 K (see SI for distribution of liquid-cooled glass). Computing the mean-squared electronic coupling for this system, which is the relevant prefactor in a non-adiabatic rate expression, yields 23.08 ± 0.01 meV for the vapor-deposited glass and 21.04 ± 0.02 meV for the liquid cooled glass. This 2 meV increase in the RMS transfer integral is substantial, as the

maximum value of the transfer integrals in these systems in which Marcus-like theories apply is 25 meV. Consequently, we again observe an approximately 10% effect in the enhancement of the electronic couplings between stable ethylbenzene glasses and conventional liquid-cooled glasses. Again, for a molecular semiconductor utilized in practical applications, we would anticipate a larger effect due to the increased pi-electron system size and potential for anisotropic ordering.

The enhancement in the transfer integral and the decrease of structural disorder can be directly related to the structural ordering of the system.[23] In the case of the transfer integral, its enhancement could conceivably arise from two effects. First, all neighboring ethylbenzene molecules are on average closer together for the 120 K PVD glass due to the relatively higher density, and thus the transfer integrals (which depend exponentially on the relative separation of the COG) will increase. Secondly, the increase in the neighboring orientational correlations between ethylbenzene molecules were shown to marginally increase (see SI), and the overlap of the pi-orbital systems should consequently increase.[145] We have evidence for both effects contributing here, though it is our expectation that the relative importance of the density-dependent effect and the orientational-dependent effect do not properly represent common organic semiconductors, as the pi-stacking configuration of two ethylbenzene molecules is not a deep global minimum[136], as it is in the majority of practical molecular semiconductors with significantly larger pi-electron systems.[51]

Regarding the decrease in the site-energy disorder, this effect is in agreement with the observed trends in the structural ordering of the films. Since the site-energy of the hole state of a molecule depends strongly on the relative orientation of the neighboring dipoles,[36] the increased structural ordering of the film should lead, on average, to a more uniform dipolar environment around each ethylbenzene molecule[67], leading to decreased energetic disorder. Again, we expect this effect to be further magnified in systems of more practical molecular semiconductors due to the larger magnitude of neighboring pi-stacking interactions to induce strong local ordering.

A third effect which influences charge transport in these systems, and which could potentially be tuned by PVD, is the role of the charge transport network topology.[68] For a hopping charge to traverse the length scale of a device, it must depend not upon single molecule properties alone, but on the correlated hops between a number of aligned molecules (a one-dimensional stack of pi-electron entities). Given the inherent weakness of van der Waals forces relative to thermal energy, the self-assembly of these molecules over device length scales is difficult. PVD presents a potentially useful mechanism for the alignment of charge transport entities over length scales larger than that dictated by van der Waals forces alone. Previous experimental work has described the importance of molecular orientation effects for charge transport and light-emitting diode applications, where the specific alignment of molecules over large length scales can lead to considerable optoelectronic enhancements.[161] While our graph-theoretical orientational correlation function is a step in this direction, the full analysis of the topology of the charge transport network, and how this varies with deposition conditions, could be integral to inducing directional charge transport within the deposited films. Work is currently underway studying this effect in more practical organic semiconductors, where the local orientational ordering, and thus the charge transport topology, depends on a deep pi-stacking minimum, and are more strongly modified by the PVD process.

2.3 Conclusions

These simulations make a series of predictions about the structure of vapor-deposited glasses of ethylbenzene in line with known experimental observables, as indicated by the computed glass transition temperature and fragility. Vapor deposition onto substrates with temperatures ranging from 95 K to 145 K led to films with enhanced kinetic stability and lower inherent structure energies relative to liquid-cooled glasses; the onset temperatures were found to be up to 11 K above those of liquid cooled films. The substrate-temperature dependent anisotropic behavior observed in past studies of larger molecules was demonstrated to

also occur for this smaller molecule. These calculations indicate that even slightly anisotropic molecules can result in anisotropic glasses when vapor-deposited. Consistent with past work for coarse-grained TPD molecules by Lyubimov *et al.*[88], the anisotropic molecular orientation in the films can be traced back to molecular ordering observed at the vacuum interface of the equilibrium liquid.

Using ethylbenzene as a minimal model for common organic semiconducting molecules, we also examined the effects of PVD-induced structural effects on molecular descriptors relevant to charge transport, specifically the distribution of site-energies and the transfer integrals between molecular sites. Our simulations demonstrate a 10% ($\approx$ 20 meV) decrease in energetic disorder and a 10% (2 meV) enhancement of the mean-squared transfer integrals within the vapor-deposited film, relative to the slowest liquid cooled film. Given the under-prediction of structural order in simulated films relative to experimental films, and the larger, more anisotropic dimensions of organic semiconductors used in practical semiconducting devices, we expect these effects to be potentially considerable in stable glasses of common organic semiconductors. Moreover, the ability of PVD to tailor the global molecular orientation of molecules in a stable glass film has potential ramifications for tailoring the topology of charge transport networks, an idea which will be explored in future work.

2.4 Methods

2.4.1 Simulated Vapor Deposition

Atomistic simulations of ethylbenzene (EB) films were performed with the all-atom optimized potential for liquid simulations (AA-OPLS) force field.[69, 72] The substrate was constructed of Lennard-Jones particles with characteristic energy and size similar to those of silica ($\sigma = 3$Å, $\epsilon = 5.2$ kJ/mol, mass = 60, and density = 2650 g/L) as used in previous all-atom PVD simulations.[134] Each substrate atom was restrained to its initial position through a harmonic potential, where the spring constant was $K = 10^4$ kJ/(mol nm^2). The

volume of the system was held constant with box dimensions 5 nm×5 nm×20 nm, and periodic boundary conditions were enforced in the lateral directions. The x and y dimensions are about 7 times the molecular length of EB ($\approx$ 7.25Å). The length of the box in the z direction (perpendicular to the substrate) was sufficiently large to encompass the film during deposition, with ample amount of vacuum space to avoid interaction between the top layer of the films at any temperature used in the study and the periodic image of the substrate (SI-Fig. 2.18). Coulombic forces were calculated using the particle mesh Ewald algorithm[41] with a force and potential correction applied in the z dimension in order to produce a pseudo-2D summation.[160] Molecular simulations were carried out using the GROMACS 4.6.3 simulation package.[59, 112] Covalent hydrogen bonds were constrained using the SETTLE[97] and LINCS[58] algorithms. All simulations were performed with a time step of 2 fs. A stochastic integrator was used during the vapor deposition process described below.[49] This choice was made due to the small number of atoms being coupled to the thermostat at certain points of the process. During production runs, including the heating and cooling runs, temperature coupling was achieved using velocity rescaling with a stochastic term.[16]

The deposition cycle consists of six repeated steps: (i) introduction of two randomly oriented molecules within 1.5 molecular lengths above the film surface (red in SI-Fig. 2.18b), (ii) minimization of the energy for the entire system using the conjugate gradient method, (iii) equilibration of the newly introduced molecules at high temperature (T=200K) for 200 ps, (iv) linear cooling over a period of 1200 ps of the newly introduced molecules to the substrate temperature, (v) a short equilibration of these molecules at the substrate temperature for an additional 200 ps, and finally (vi) minimization of the energy for the entire system. A separate thermostat is used to maintain the previously deposited molecules and substrate particles at the desired substrate temperature throughout the cycle. Any molecules that remain in the vacuum region, dissociated from the film at the end of a deposition cycle, are deleted to avoid the formation of separate aggregates. The energy is minimized at the start

and end of the cycle, as discussed in previous work[134], in order to help relax the films during the relatively shorter timescales that are accessible to simulations compared to those used in experiments. This process was repeated until all the films have at least 1200 or more EB molecules inserted, which in the glass state corresponds to a film thickness of about 8 nm (SI-Fig. 2.17).

The bulk of the film was defined to be from 4.8 nm to 7.2nm in the z dimension, or roughly 3.3 molecular lengths thick. These limits are based on where the substrate effect in the density fluctuations is dampened and where the Debye-Waller factor becomes relatively constant before rapidly increasing again near the free interface, as demonstrated for the three samples deposited at T_{s}=130K ($0.89T_{\mathrm{g}}$) in SI-Figure 2.17 and highlighted in SI-Fig. 2.18b. The Debye-Waller factor, denoted by $\langle u^2 \rangle$, is defined as the average mean-squared-displacement of hydrogen atoms after 20 ps; this is a commonly measured quantity that can be extracted both from neutron scattering experiments and from simulations, and it provides a measure of local mobility and free volume. Three independent films were deposited for each substrate temperature, and five independent samples were used to generate statistically meaningful results for the liquid-cooled films.

2.4.2 Energetic Disorder for Charge Transport

The bulk region of the glass was examined for charge transport. For every molecule in this region, a 2-level ONIOM[30] (B3LYP/6-31G*: CHARMM) optimization was performed on the cationic state for the ethylbenzene molecule within a frozen shell of nearest neighbors (cutoff = 7 Å). The cation state represents the electronic state of interest for hole transport in a molecular semiconducting film. Our ONIOM methods treats the center molecule at the DFT level (B3LYP/6-31G*), and the nearest neighbor shell with molecular mechanics (CHARMM). This modest basis set size is necessary for the calculation of energetic disorder over the entire film width to be performed in a reasonable amount of computer time. The ONIOM optimization yields a local site-energy for every molecule in the film, which is

dictated by the precise arrangement or packing of the neighboring molecules. Site energies are computed for all molecules in the region and histogrammed over the film width, with subsequent averaging for five trajectory snapshots for three separate trajectories for both the conventional liquid-cooled glass and the 120K vapor deposited glass. The histogram is then plotted and fit to a Gaussian disorder model to obtain the standard deviation of the site energies.[43] Note that a larger standard deviation of the site energy implies more energetic disorder, and has a deleterious effect on charge transport. All electronic structure calculations involved in the determination of site energies were performed using the Gaussian software package[46].

2.4.3 Transfer Integrals for Charge Transport

Each molecule surrounded by "N" nearest-neighbors within the 7 Å cutoff was parsed into N separate snapshots where the transfer integral for hole self-exchange between two ethylbenzene sites is determined using the Electron Transfer module[150] in NWChem at the B3LYP/6-31G* level of theory. The self-exchange reaction can be denoted (EB/EB+ $\rightarrow$ EB+/EB), where EB+ and EB represent the cation state and ground state of ethylebenzene, respectively. Transfer integrals between all nearest neighbors are computed for all molecules in the film, with subsequent averaging for five trajectory snapshots for three separate trajectories for the liquid-cooled and vapor-deposited morphologies. The mean-squared electronic coupling is then determined from the distribution of transfer integrals in the film. This mean-squared coupling would be the exact input used in a Marcus-like approach to charge transfer theory,[70] and thus the larger its value, the more beneficial for charge transport within the film.

2.5 Supporting Information

2.5.1 Effective T_g

Three different cooling rates were applied to the system and the corresponding fictive temperatures calculated are presented in Fig. 2.8. There is a slight effect observed for the faster cooling rates on the instantaneous density and Debye-Waller factor, which may suggest that higher rates are becoming less physical. As the thermostat decreases the temperature of the system, the system lags slightly behind in equilibration due to the timescale. To correct for this effect, snapshots are taken at various temperatures during the cooling process and allowed to equilibrate at the appropriate temperature for 1 nanosecond. The values reported are averaged over the nanosecond trajectories for five samples with the standard deviation given as the error bars.

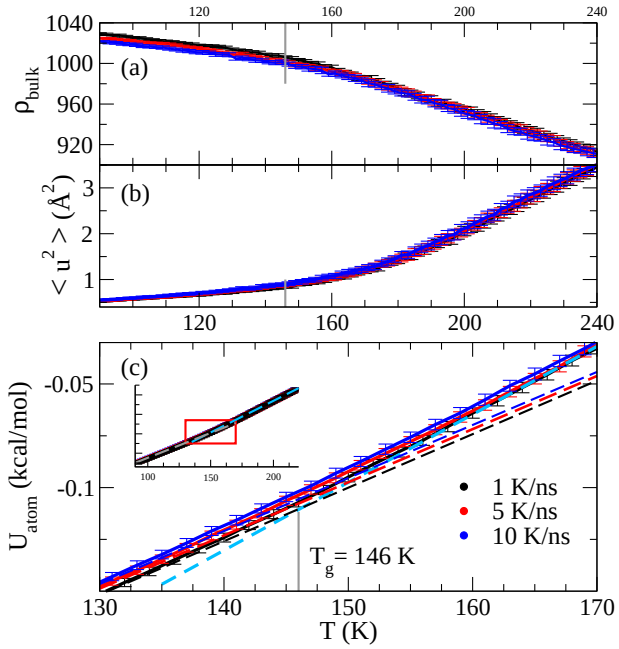

Figure 2.8: Three different cooling rates were investigated: 1 K/ns (black), 5 K/ns (red), and 10 K/ns (blue). The temperature at which the intensive potential energy per particle deviates from the super-cooled liquid line (dashed cyan line) was used to estimate the T_{f}, panel **(c)**, which is estimated from the intersection of the glass line for q_{c}= 1 K/ns (dashed grey line) to be 146 K. The panels **(a)** and **(b)** display the temperature dependence of the middle bulk density, ρ_{bulk}, and the average bulk Debye-Waller factor, respectively, with 146 K marked by a grey line.

2.5.2 Rotational Relaxation

A relaxation time τ_{rot} was extracted by fitting a stretched exponential to the rotational autocorrelation function with respect to the molecular orientation vector (Fig. 2.9). The τ_{rot} and β for each fit are provided in Table 2.1.

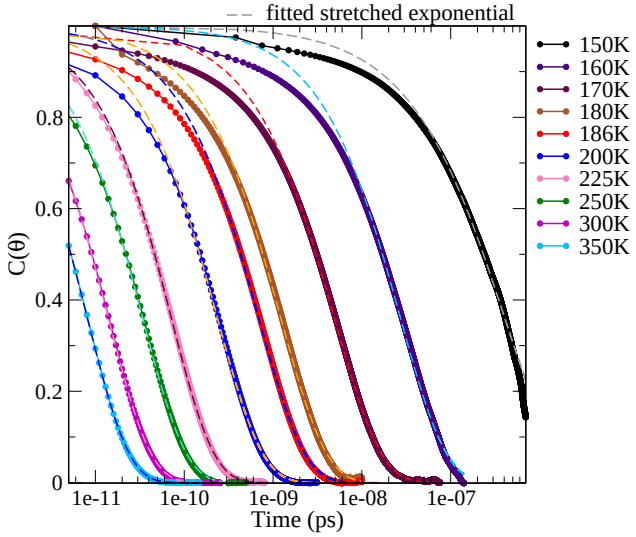

Figure 2.9: Angular correlation with respect to the molecular orientation vector described in Figure 1a averaged over the bulk region of the film. Each dotted solid line is a liquid or super-cooled liquid ranging in temperatures from 350 K down to 150 K, which is just 4 K above the effective T_{g}. The dashed lines are fitted stretched exponentials to each decay curve.

Using the above parameters, a VFT fit was applied to extrapolate to the conventional glass transition temperature and to calculate the fragility.

Table 2.1: Parameters for stretched exponentials : $C(\theta) = \exp\left(-\left(\frac{t}{\tau_{\rm rot}}\right)^{\beta}\right)$

T (K)	$\tau_{\rm rot}$ (s)	β
150	3.68×10^{-7}	0.77
160	2.66×10^{-8}	0.80
170	4.78×10^{-9}	0.81
180	1.19×10^{-9}	0.83
186	6.74×10^{-10}	0.83
200	2.34×10^{-10}	0.85
225	6.99×10^{-11}	0.89
250	3.39×10^{-11}	0.90
300	1.37×10^{-11}	0.90
350	7.84×10^{-12}	0.91

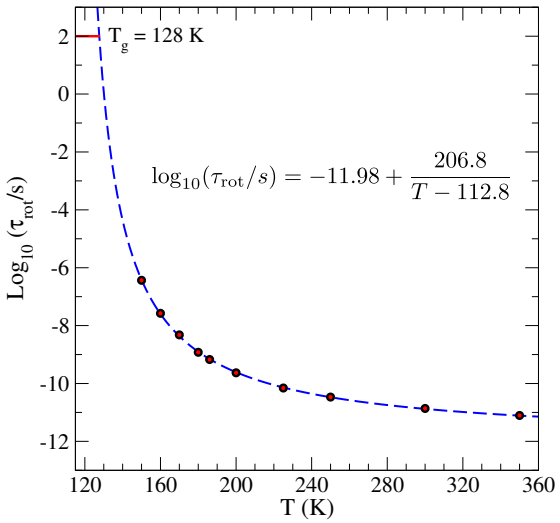

Figure 2.10: The VFT equation was fitted to $\tau_{\rm rot}$ (red points) calculated for temperatures ranging from 150 K up to 350 K. Extrapolating this function to $\tau_{\rm rot}$=100 sec gives a conventionally defined $T_{\rm g}$ of 128K for this model.

2.5.3 Substrate Temperature Comparison

The onset temperature calculated for the various vapor-deposited glasses are very similar, Fig. 2.11. The films with a T_s of 120K or 115K have a T_{on} of approximately 173K and the films with a T_s of : 105, 125, 130, 135, or 140K have a T_{on} around 170K. Whereas, the slowest cooled glass with q_c=1K/ns, has T_{on} of $\approx$ 159K. Thus, all VD glasses have enhanced kinetic stability relative to the conventional glasses. This similar T_{on} for the various T_s is in agreement with how similar the inherit structure energies and the densities in Fig. 2.11b are.

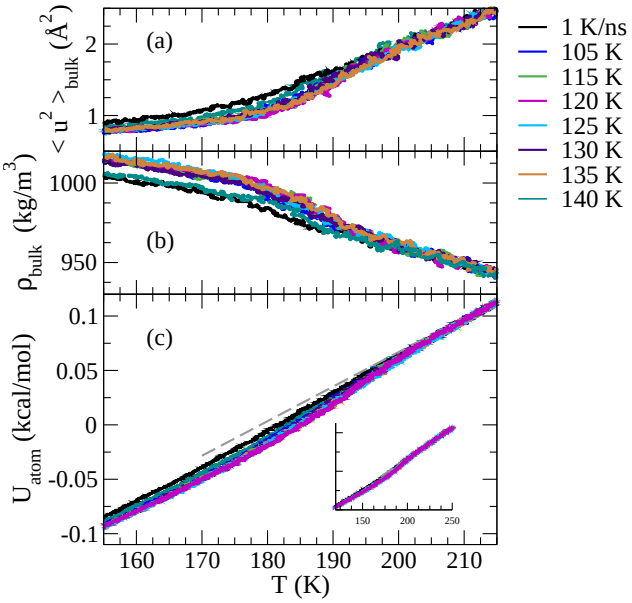

Figure 2.11: The liquid-cooled film with q_c=1 K/ns (black) and the vapor deposited films (colored) were subjected to a heating run at a rate of 5K/ns, after first being cooled to 90K for comparison. The average bulk Debye-Waller factor, ρ_{bulk}, and the intensive potential energy were calculated as a function of temperature (panels **(a), (b)**, and **(c)** respectively). The onset temperature seems to be similar for all vapor deposited films except for T_s = 140 K (dark cyan), but all are higher than the liquid-cooled glass.

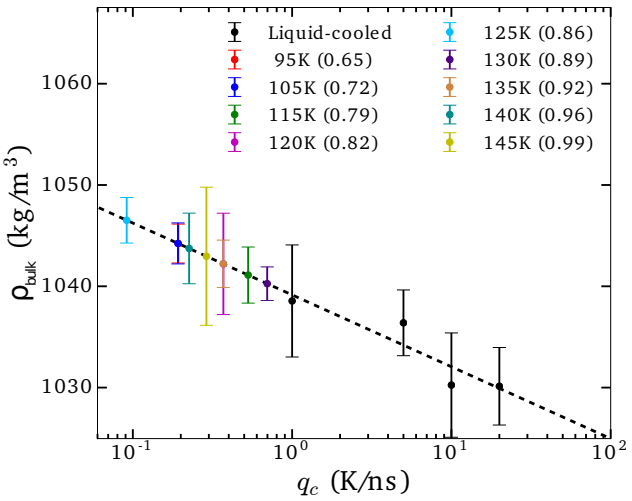

Figure 2.12: The bulk density, ρ_{bulk}, is given as a function of cooling rate. The black points are calculated from the liquid-cooled glasses as a function of cooling rate, q_{c}. The vapor deposited glasses (colored points) are plotted by the predicted q_{c}, assuming a linear relation between ρ_{bulk} and the order of q_{c}(dashed line). Error bars are calculated from the standard deviation of three samples for vapor deposited films and five samples for the liquid-cooled.

2.5.4 Arrest Depths

The arrest times, t_a, and the depth at which it occurs, z_a, appear to have an exponential dependence on substrate temperature. There is a temperature regime where it appears linear, but the films at the lowest temperatures plateau as they approach 0 and the higher temperature films quickly increase as the films approach the simulated T_g.

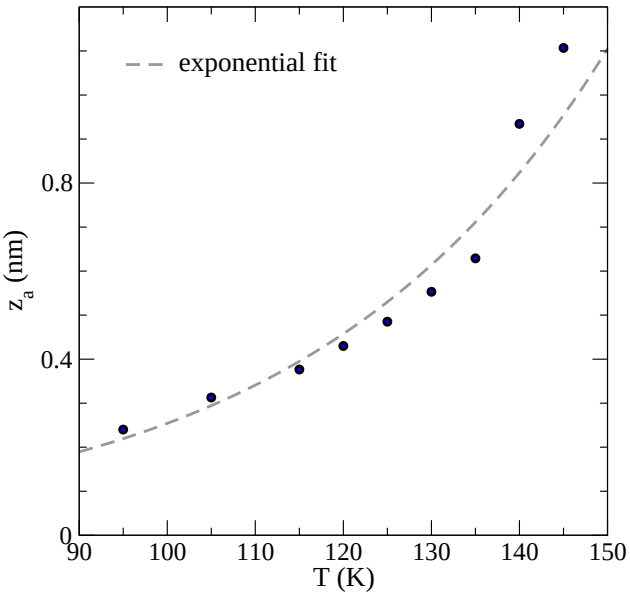

Figure 2.13: The distance from the surface that corresponds to the time of rotational arrest, z_a, as a function of T_s. An exponential function was fitted to the data (grey dashed lines).

2.5.5 Bulk Films Molecular Orientation

Figure 2.14 provides the full $\cos(\alpha)$ distribution for the liquid-cooled glass and a larger subset of the PVD glasses than provided in the main text. For reference, a dotted line is shown to illustrate the uniform distribution that is expected for a completely isotropic film.

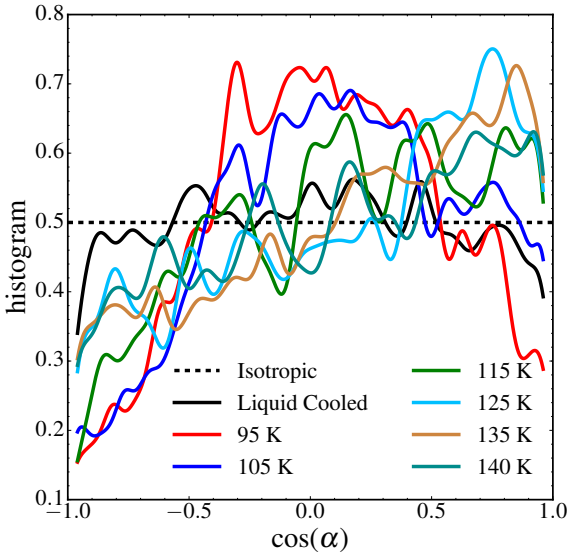

Figure 2.14: Distribution of $P_1 = \cos(\alpha)$ values in the bulk of the liquid-cooled glass (black), where q_c= 1K/ns, and vapor deposited glasses (colored). Calculated using a Gaussian kernel density estimation (bandwidth = 0.10).

2.5.6 Molecular Orientation and Distance Correlation

The probability of benzene ring alignment was calculated as a function of center of geometry (COG) distance. Averaging over molecules within the bulk region of the film, only neighbors that were within a cylinder of radius 1 nm centered at the COG of the benzene ring of interest and aligned with that normal of the benzene ring of that molecule were considered. Each column is normalized to one, giving the probability of a neighboring benzene ring having that cosine alignment for a given distance.

The distance from the center of the cylinder was calculated as follows. First, project the COG vector, $\boldsymbol{v}_{COG}$, onto the benzene ring unit vector, $\boldsymbol{v}_{benz}$, which is simply $\boldsymbol{v}_{projCOG} = (\boldsymbol{v}_{COG} \cdot \boldsymbol{v}_{benz})$. The radial distance from the center of the cylinder is the magnitude of the vector $\boldsymbol{v}_{rad} = \boldsymbol{v}_{COG} - \boldsymbol{v}_{projCOG}$.

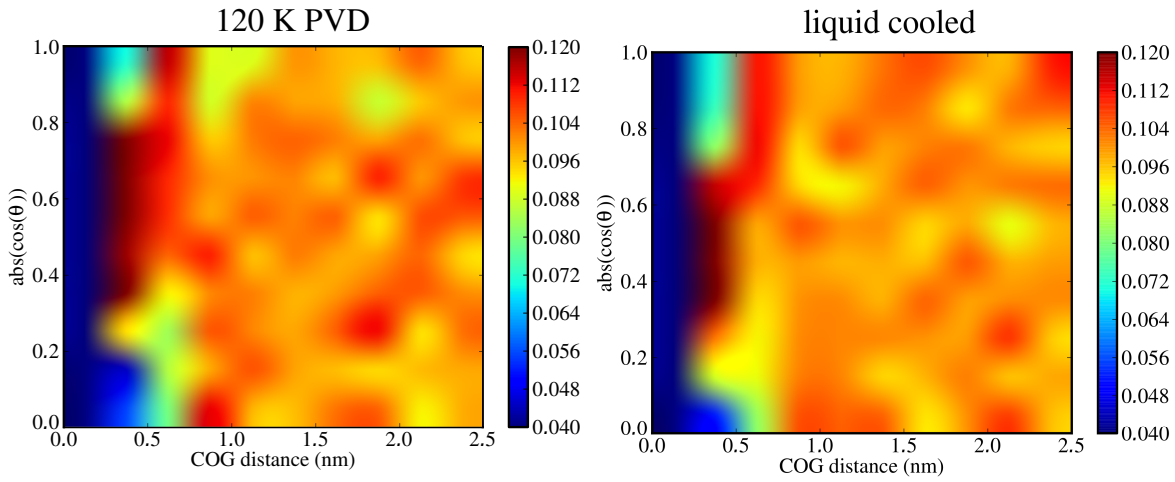

Figure 2.15: The probability of absolute value cosine alignment of the benzene ring normals for neighbors at a give center of geometry (COG) distance, where each neighbor is within a cylinder of radius 1 nm centered on the benzene ring and pointing in the direction normal of the benzene ring.

2.5.7 A Graph Theoretical Approach to the Orientational Correlation Networks

To further explore the distance dependence of orientational correlations we used a modification of a graph theoretic approach to charge transport networks developed in previous works. Using the absolute value of the dot-product of the pi-system unit normal vectors between two neighboring ethylbenzene molecules, we set up an adjacency matrix to describe the orientational connectivity of the ethylbenzene molecules within the middle section of the film. This adjacency matrix is defined as:

$$A_{ij} = \begin{cases} \text{abs}(\boldsymbol{v}_{benz,1} \cdot \boldsymbol{v}_{benz,2}) & i \neq j \\ 0 & i = j \end{cases} \tag{2.8}$$

We can then form the Laplacian matrix using the strength matrix, S, and the adjacency matrix, A, by L = S - A. The second eigenvalue of this Laplacian matrix is known as the algebraic connectivity, and represents how well-connected the overall graph is.

We then compare the values of the algebraic connectivity for the liquid-cooled and 120K PVD films, obtaining values of 0.0215 +/- 0.019 for the latter, and 0.0172 +/- 0.016 for the former. While the PVD film shows a slight increase in the algebraic connectivity of the orientational correlation network relative to the liquid-cooled films, this result is well within the error bars, and thus by this metric the orientational differences in these systems manifest by the vector normal to ethylbenzene's pi-electron system are quite subtle, in agreement, with the previous section on molecular orientations and distance correlations.

2.5.8 *Charge Transport in Liquid Cooled*

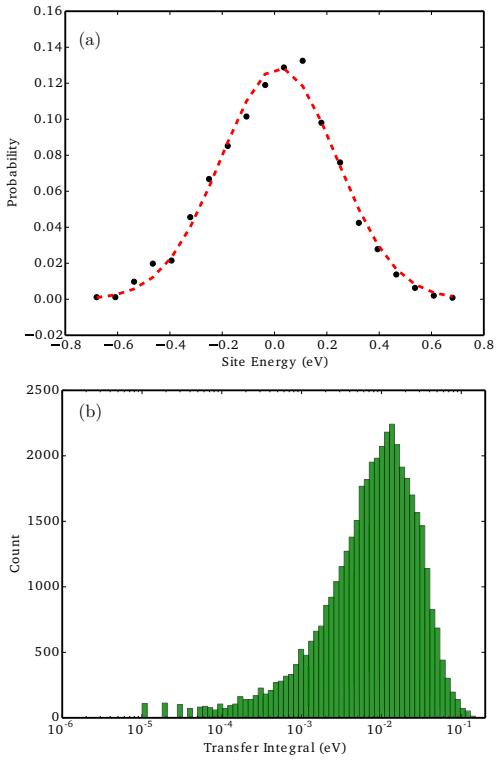

Figure 2.16: Histograms of the **(a)** molecular site-energies in eV and **(b)** the transfer integrals (eV) for the liquid-cooled glass.

2.5.9 Bulk Region

To define the bulk region for analysis, effects from both interfaces needed to be avoided as much as possible. The Debye-Waller Factor was considered for the change in mobility caused at each (arrested near the substrate, and higher mobility at the vacuum interface), as well as the density.

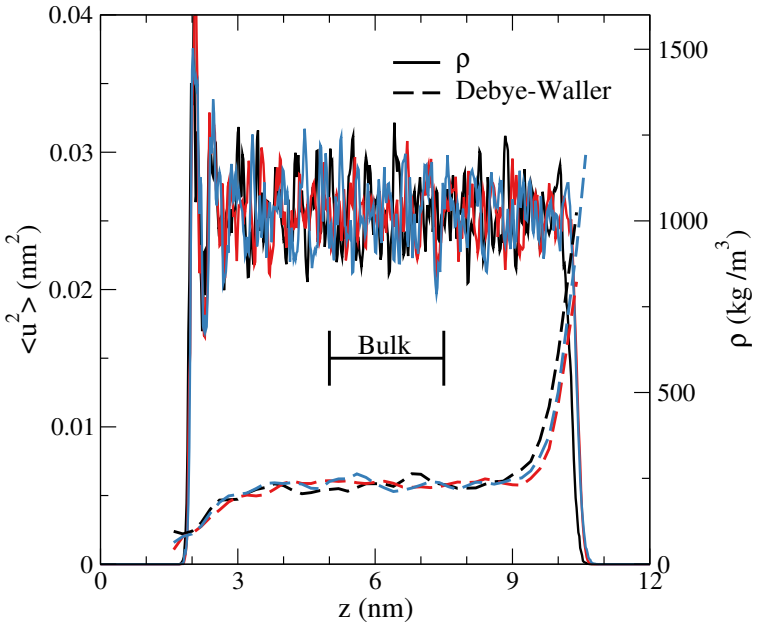

Figure 2.17: The Debye-Waller factor (dashed lines) and density (solid lines) as a function of z, where the substrate oscillates around 1 nm, for $T_{\mathrm{s}} = 130$ K ($0.89T_{\mathrm{g}}$). There are three independent samples (different colors) per substrate temperature. The bulk region is defined as z between 4.8 nm and 7.2 nm, where the surface effects from the substrate and the free-surface are dampened out.

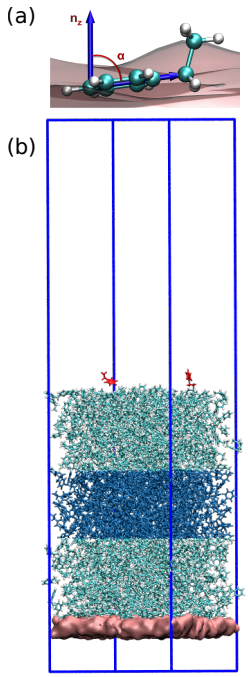

Figure 2.18: **(a)** Image of the all-atom ethylbenzene model. The vector normal to the substrate, n_z, and the angle, α, between it and the vector used to describe the molecular orientation. **(b)** Snapshot from the vapor deposition process. The particles that form the substrate are represented as a surface, the box edges are blue. Two newly inserted molecules are highlighted as red whereas the previously deposited molecules are colored by atom (cyan for carbon, white for hydrogen). The inner bulk region of the film used is colored with a darker blue.

CHAPTER 3

PHOTOSTABILITY CAN BE SIGNIFICANTLY MODULATED BY MOLECULAR PACKING IN GLASSES

In this chapter we analyze how the "ultra-stability" gained by some molecules through performing vapor-deposition may have on the photostability of the material. To this point, we instigated the resistance of a material to the photoisomerization reaction of an azobenzene unit. Yue Qiu vapor deposited an azobenzene derivative Disperse Orange 37 (DO37) and I developed and simulated a coarse-grained representation of azobenzene. For both systems, we demonstrate that stable glasses can be formed via vapor deposition. We then show for both systems that properties such as density and average molecular orientation, which are affected by the photoisomerization process, are more resistant to change for a vapor deposited glass. This resistance correlates well with the higher densities observed for the various vapor-deposited glasses, which leads us to postulate that this higher resistance is due to a disfavoring of certain relaxation pathways requiring rearrangement of the densely packed material. Section 3.2.6 was not included in the original publication cited below, but was added for further insight.

3.1 Introduction

Glasses are amorphous materials that have wide usage in modern technology, including polymers,[138] pharmaceuticals,[164] solar [17] and organic electronics.[161, 133] For many applications, organic materials prepared as amorphous states are preferred over crystalline solids. For example, in the pharmaceutical industry, some drugs are formulated as glasses due to their higher solubility and bioavailability.[53, 80] In the organic electronics field, glasses are frequently used in device fabrication to provide smooth and homogeneous layers.[161] One important issue for organic glasses is photochemical stability. Photodegradation can cause the failure of organic electronics in both display and light harvesting technologies, and this is sometimes a more limiting factor than device efficiency.[62, 155] As photodegradation can be caused by light in the environment or by self-emission,[155, 128] photochemically robust materials are in demand.[128, 118]

Previous work has shown that modification of local packing in glasses has a negligible effect on photostability in comparison to what has been observed for crystalline materials. Organic molecules can have very different photoreactivities in different crystal polymorphs. In pioneering work in topochemistry, Schmidt *et al.* studied the [2+2] photodimerization of cinnamic acid in the solid state. This compound crystallizes in three polymorphic forms which exhibit different photochemical reactivity upon irradiation.[126] An even more striking example is provided by tetrabenzoylethylene, which can undergo unimolecular photoisomerization. Of the two crystalline modifications, one polymorph is light stable while the other photoisomerizes to the furanone.[21] In contrast, for amorphous materials, it has been found that photoreactivity depends only slightly on the manner in which the glass is prepared. Torkelson *et al.* reported that, for 4,4'-diphenyl azobenzene dispersed in amorphous polycarbonate, the susceptibility to photoisomerization decreased by about 5% after physical aging for 100 hours; aging generally increases the density of a glass.[121] We are not aware of a literature precedent showing significant tuning of photoreactivity in organic glasses through control of local packing.

Recently, physical vapor deposition (PVD) has been used to prepare glasses with exceptional properties that are not accessible by any other preparation method.[141, 82, 132, 119, 115, 29] By properly controlling processing conditions such as deposition rate and substrate temperature, vapor deposition can form *stable glasses* that have higher density and enhanced kinetic stability relative to that of traditional liquid-cooled glasses. Typically, the optimal substrate temperature for preparing these PVD glasses is about 0.85 T_{g}, where T_{g} is the glass transition temperature. Vapor-deposited glasses can exhibit enhanced kinetic stability; upon heating at a constant rate a stable glass can maintain its glassy packing to a much higher temperature than a liquid-cooled glass. Vapor-deposited glasses also have densities up to 1.4% higher than the corresponding liquid-cooled glass.[27] It has been estimated that a liquid-cooled glass would have to be physically aged for thousands to millions of years to achieve a glass with the same density.[76] Many of the features observed in experimental PVD glasses, including high density and high kinetic stability, have also been observed in computer simulations that mimic the vapor deposition process.[29, 88, 89]

In this work, we test whether the extraordinary kinetic stability and high density of PVD glasses also lead to extraordinary photostability. As a model system, we investigate the photostability of vapor-deposited and liquid-cooled glasses of 3-[[4-(2,6-dichloro-4-nitrophenyl)azo]-*N*-ethylanilino]-propionitrile (also known as Disperse Orange 37 or DO37), an azobenzene derivative. Azobenzenes can undergo *trans* $\rightarrow$ *cis* photoisomerization reactions when irradiated by light; the *cis* state will relax back to the *trans* state spontaneously, as the *trans* state is thermodynamically more stable. We vapor-deposited DO37 onto substrates held at different temperatures and successfully obtained glasses with different initial densities and a wide range of kinetic stabilities. Using spectroscopic ellipsometry, the photostability of the different DO37 glasses during light irradiation was characterized by changes in the glass density and birefringence. In this way, the photostability of a series of glasses with identical composition but different densities could be easily compared.

We find that photostability of vapor-deposited DO37 glasses can be significantly mod-

ulated through the choice of substrate temperature. The most photostable PVD glass is 50 times more resistant to light irradiation than the liquid-cooled glass. We observe that photostability is highly correlated with the density of the vapor-deposited glasses. Molecular simulations of photoisomerization in vapor-deposited glasses are able to capture the key features observed in the experiments, and provide further molecular-level insight into the mechanism of stability. In particular, the tight molecular packing of the denser glass creates higher energy barriers for molecular rearrangement which then inhibit the photoisomerization reaction. We expect that enhanced photostability is a general property of dense vapor-deposited glasses that may also be exploited with other molecular systems, including those used in organic electronics.

3.2 Results and Discussion

3.2.1 Vapor-Deposited DO37 Forms Glasses with High Kinetic Stability

As an initial step in these experiments, we used spectroscopic ellipsometry to characterize the kinetic stability and density of PVD glasses of DO37. Figure 3.1 shows an example of a temperature-ramping experiment for a DO37 glass vapor-deposited at $T_s = 260$ K ($0.88\ T_g$). Three different ramping cycles were performed. In the first cycle, the as-deposited sample was first heated from 288 K to 320 K and then cooled back to 288 K. Subsequent heating and cooling cycles between 288 K to 310 K are also shown, and all heating/cooling rates were 1 K/min. During the first cycle of heating, the initial increase in thickness (below 303 K) is due to thermal expansion of the as-deposited glass. At the onset temperature (T_{on}), the as-deposited glass begins to transform into a super-cooled liquid. During subsequent cooling, the super-cooled liquid falls out of equilibrium and transforms into a glass at T_g. As expected, the second and third cooling runs shown in Figure 3.1 are indistinguishable from the first cooling since they all started in the equilibrium supercooled liquid.

The as-deposited glass of DO37 in Figure 3.1 shows high kinetic stability and high density

relative to the liquid-cooled glass. The high T_{on} (12 K above T_g) required to transform the as-deposited glass into the supercooled liquid is an indication of enhanced kinetic stability. The change in thickness between the first heating and cooling cycles is used to determine the density of the as-deposited glass relative to the liquid-cooled glass ($\Delta\rho$). In this case, the as-deposited glass is 1.3% more dense, consistent with more efficient local packing and higher kinetic stability. Vapor-deposited glasses of DO37 have properties similar to other PVD glasses with high kinetic stability.[141, 82, 119, 115, 148, 170, 32, 153] For comparison, indomethacin, an extensively studied system, has been reported to form glasses with T_{on} as high as 18 K above T_g, along with density increases of up to 1.4%.[27]

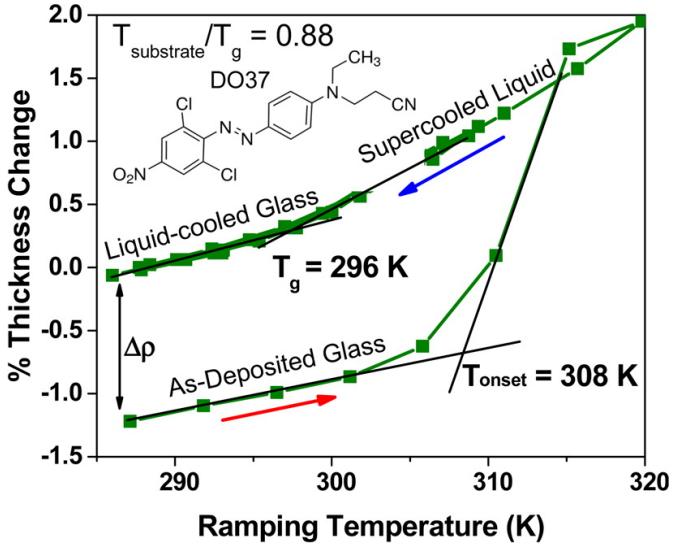

Figure 3.1: Thickness changes for a vapor-deposited glass of DO37 during temperature ramping at 1 K/min. The green symbols represent experimental data for a sample prepared at $T_s = 0.88T_g$. Black lines are linear extrapolations that demonstrate the determination of T_g (for the liquid-cooled glass) and the onset temperature T_{on} (for the as-deposited glass). $\Delta\rho$ shows the density difference between the as-deposited and liquid-cooled glass. The inset shows the molecular structure of DO37.

The kinetic stability of vapor-deposited DO37 glasses depends on the choice of substrate temperature during PVD. As indicated by the inset in Figure 3.2, DO37 glasses were prepared on a substrate that had an imposed temperature gradient ranging from 0.75 T_g to above T_g. In this way, a library of glasses was prepared in one deposition. The detailed method of sample preparation is presented in the Methods section. For glasses deposited above

T_g (296 K), the as-deposited sample had the same onset temperature as the liquid-cooled glass. For $T_{substrate}$ lower than T_g, enhanced kinetic stability was obtained. The optimal T_s for kinetic stability is 0.88 T_g (Figure 3.2), which is similar to indomethacin and other molecular systems.[76] The increased kinetic stability and density of vapor-deposited films is attributed to enhanced surface mobility during film formation.[89, 169, 165] Freshly deposited molecules have enough mobility to efficiently sample packing arrangements, resulting in near-equilibrium local packing well below T_g; subsequent deposition locks this efficient packing into the glassy film. The optimal stability obtained by deposition onto substrates near 0.88 T_g is a result of the competition between kinetic and thermodynamic control.[76] At lower temperature surface mobility is not high enough to allow access to better packing arrangements even though the thermodynamic driving force is larger.

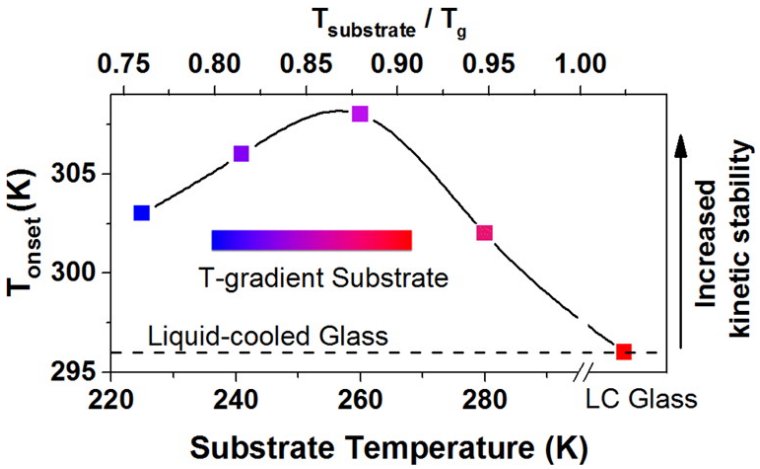

Figure 3.2: Kinetic stability of DO37 glasses vapor-deposited at different substrate temperatures. T_{on} represents the onset of glass transformation during heating of 1 K/min. All glasses were prepared during one deposition on a temperature gradient substrate. The inset schematically indicates a temperature-gradient across the substrate. The solid black line is a guide to the eye.

3.2.2 PVD Glasses Exhibit Enhanced Photostability

The photostability of DO37 glasses was monitored by spectroscopic ellipsometry during light irradiation. Density and birefringence, representing molecular packing and molecular

orientation respectively, can be obtained by ellipsometry and were used to characterize photostability of the glassy thin films. As shown in Figure 3.3, a 532 nm laser was used to irradiate the thin glass samples and induce photoisomerization. Simultaneously, spectroscopic ellipsometry measured the thickness and birefringence changes in the irradiated area. Since the in-plane sample dimensions are fixed, density is inversely related to thickness.

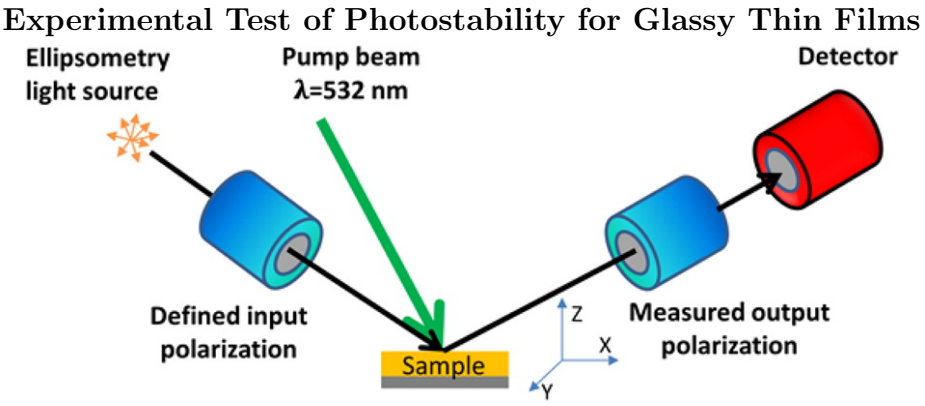

Figure 3.3: A 532 nm laser is used to irradiate the DO37 thin film inducing photoisomerization. Simultaneously, spectroscopic ellipsometry is used to measure thickness and birefringence changes in the film.

A comparison of the light-induced density and birefringence changes for PVD and liquid-cooled glasses, as shown in Figure 3.4, reveals that the PVD glasses display significantly enhanced photostability. The density of the liquid-cooled glass decreases immediately after irradiation begins and reaches steady-state in tens of seconds. In contrast, PVD glasses can maintain their original density for hundreds to thousands of seconds, depending on the substrate temperature at which the sample was deposited. The birefringence measurements also show that vapor-deposited glasses are more photostable; molecules in PVD glasses are more resistant to light-driven changes in molecular orientation. Both *s*-polarized and *p*-polarized irradiation result in similar trends. Results for *s*-polarized irradiation are shown in Figure 3.4 while results for *p*-polarized irradiation are given in the Supporting Information (SI), SI-Figure 3.11.

Previous studies of azobenzene-containing glasses under irradiation have proposed mechanisms which qualitatively explain the density and birefringence changes shown in Fig-

ure 3.4.[139, 143, 52, 131] *Trans*→*cis*→*trans* cycling disrupts packing in the glassy matrix due to changes in molecular shape and molecular volume.[12, 54] Because of the very long relaxation time of the glass, molecules have little opportunity to re-optimize their local packing during irradiation. Changes in birefringence during irradiation can be attributed to the photoalignment effect.[52] When a molecule returns to the *trans* state after isomerization, it need not have the same orientation as it had initially. Repeated photoisomerization with polarized light has the net effect of increasing the fraction of molecules whose transition dipoles are orthogonal to the excitation polarization, since these molecules do not have the opportunity for further photoisomerization; the sample thus becomes anisotropic and birefringent. We note that most as-deposited glasses of DO37 showed negative initial birefringence (SI-Figure 3.12). In Figure 3.4b, the birefringence is shifted so that the initial value is zero for all glasses for easier comparison.

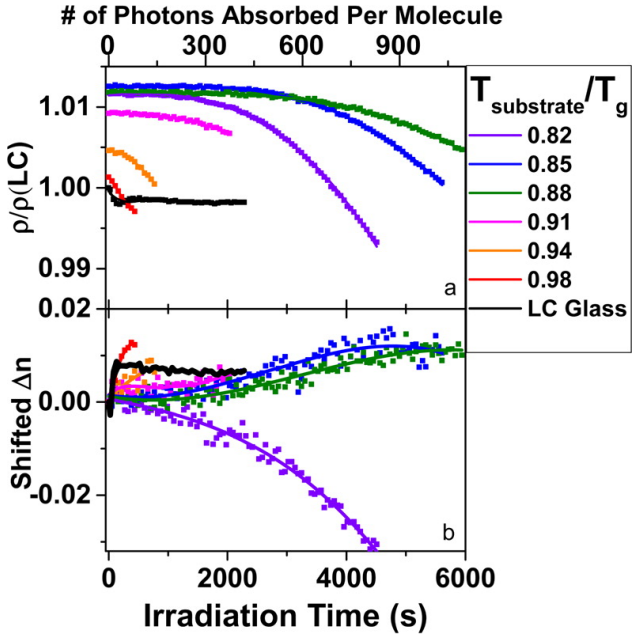

Figure 3.4: Density and birefringence changes for vapor-deposited and liquid-cooled glasses of DO37 as a function of irradiation time. (a) Glass density relative to initial density of the liquid-cooled glass. (b) Birefringence Δn relative to as-deposited glass. Lines are guides to the eye.

3.2.3 Photostability Correlates with Glass Density

To quantitatively compare photostability of vapor-deposited and liquid-cooled glasses, we analyze the experimental results presented in Figure 3.4. Figure 3.5a shows the irradiation times required to achieve small changes in density and birefringence. These small changes in density (0.1%) and birefringence (0.005) represent the initial structural alteration of the glasses, at a stage where the glasses have not yet lost their initial material properties. Photostabilities deduced from these two observables are highly consistent. For comparison, Figure 3.5b shows the density for DO37 glasses vapor-deposited at different substrate temperatures relative to the liquid-cooled glass. All glasses deposited with $T_s<T_g$ show higher densities than the liquid-cooled glass. The maximum density is observed for a substrate temperature of 0.86 T_g, which is consistent with previously reported vapor-deposited glasses of indomethacin.[27]

By comparing Figure 3.5a and 3.5b, it is evident that there is a strong correlation between photostability and glass density, and that the higher density of the PVD glasses is associated with a 50-fold increase in photostability. As we discuss further below, there is no precedent for such a large effect of glass packing at ambient pressure. In a study of an azobenzene derivative tethered to a PMMA polymer, it was demonstrated that optically induced molecular orientation can be hindered by density increases caused by high pressure;[100] compared to ambient pressure, the glass density at 150 MPa was increased by 2.4% and the rate of photo-orientation decreased by a factor of nearly 50. This high pressure work demonstrated a correlation between density and photostability that is qualitatively consistent with the results in Figure 3.5. However, in the work of ref 100, enhanced photostability was only observed at high pressure and the rate of photoisomerization became fast again when the pressure was released. In contrast, the present work provides a method to increase the photostability of ambient-pressure materials.

To test the generality of the effect of enhanced photostability, we performed additional experiments at a lower irradiation temperature and found that PVD glasses of DO37 become

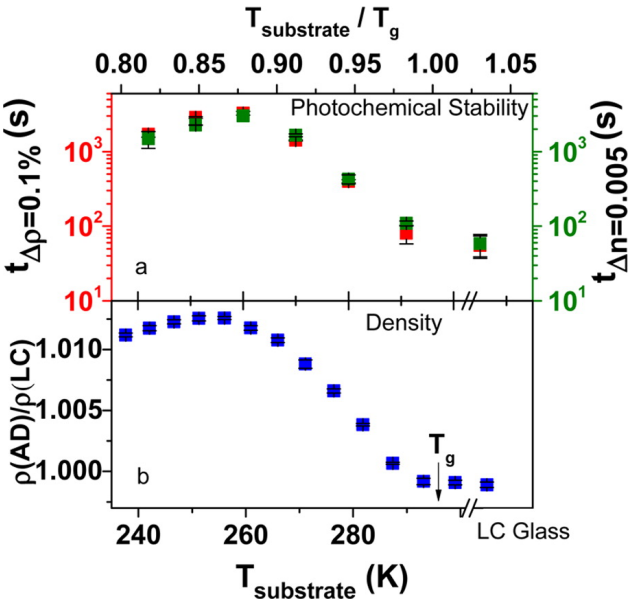

Figure 3.5: Photostability and density of PVD glasses of DO37, with comparison to the liquid-cooled (LC) glass. A strong correlation is observed between photostability and density. (a) Irradiation time required to achieve a 0.1% density change (red) and 0.005 birefringence change (green). (b) Density of as-deposited (AD) glasses relative to the LC glass. For substrate temperature below T_g, vapor-deposited glasses show increased density, and the maximum density occurs at 255 K (0.86 T_g).

even more photostable relative to the liquid-cooled glass. In the field of organic electronics, materials are usually used at temperatures at least 30-40 K below T_g. In contrast, for experiments described in Figure 3.4 and 4, the measurement temperature was 287 K, only 9 K below the T_g for DO37. For a few experiments, we lowered the measurement temperature to 278 K (T_g-18 K) to get closer to the conditions for many applications. For PVD glasses, the photostability results are nearly the same at 278 K and 287 K (SI-Figure 3.14). For the liquid-cooled glass, however, photoinduced density and birefringence changes occurred more quickly at lower temperature (SI-Figure 3.15), such that the PVD glasses are even more photostable at lower temperature, relative to the liquid-cooled glass. This behavior of the liquid-cooled glass can be attributed to the competition between photoinduced changes and structural relaxation back towards equilibrium.[130] At lower temperatures, structural relaxation becomes slower, allowing illumination to more quickly drive the system away from equilibrium.

3.2.4 Molecular Simulations of PVD Glasses

Molecular simulations of the vapor deposition and photoisomerization processes were performed to understand the mechanism of enhanced photostability in PVD glasses. In order to focus on the key physics responsible for the packing effects observed in our experiments, we propose a simple model to examine isomerization, namely a linearly-connected molecule of four beads that serves as a coarse-grained representation of DO37 (Figure 3.6, inset). During the vapor deposition portion of the simulations, which utilized a procedure employed in previous simulations of PVD glasses,[88, 89, 144, 135] these molecules were held in the *trans* state. Glass films were deposited onto substrates at temperatures ranging from 0.76 T_g to 0.97 T_g, where T_g was determined to 0.66 (in reduced Lennard-Jones units) by simulations in which the liquid was cooled into the glass. (SI-Figure 3.16). Consistent with the experimental results in Figure 3.5b, all the simulated PVD glasses had higher density than the liquid-cooled glass (SI, Table 3.1). During the photoisomerization portion of the simulations, an iterative method mimicking the stochastic process of photoexcitation, described in the Methods section, was then used to test the photostability of each of the glasses formed. In brief, a few molecules are "photoexcited" by instantaneously switching the dihedral potential from the initial state (where *trans* is the stable state) to a new potential (where *cis* is the stable state). Molecular dynamics simulations are then continued with the local packing environment of each molecule determining whether or not the *cis* state can actually be reached. After a period of time (mimicking the excited state lifetime), the potential is switched back to the original one favoring the *trans* state. This process is repeated many times with molecules randomly selected for photoexcitation.

Figure 3.6 shows that the simulated PVD glasses have substantially increased photostability relative to the liquid-cooled glass, in qualitative agreement with the experimental results shown in Figure 3.4. The top panel of Figure 3.6 shows that the PVD glasses, which have higher initial densities than the liquid-cooled glass, maintain their initial density for a greater number of photoexcitation cycles. The middle panel of Figure 3.6 shows the orientation or-

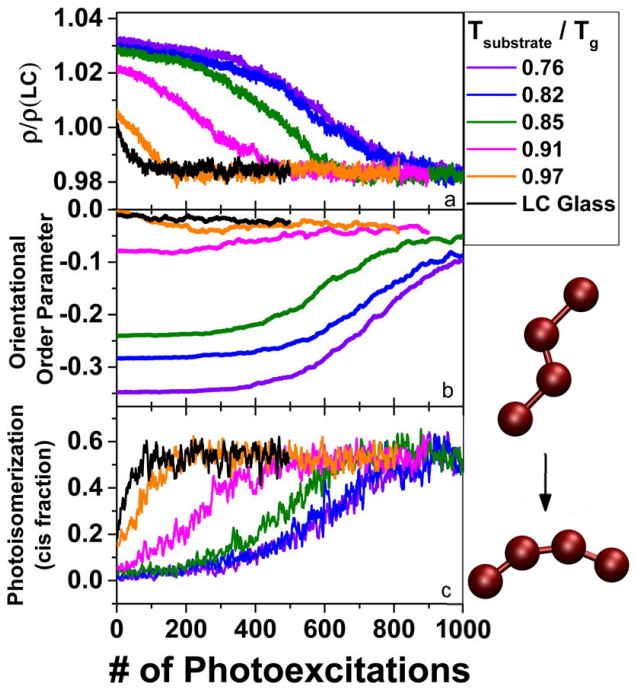

Figure 3.6: Simulations of photostability for vapor-deposited and liquid-cooled (LC) glasses as a function of photoexcitation cycle. (a) Glass density relative to LC glass (ρ/ρ(LC)). (b) Orientation order parameter. (c) Fraction of successful *trans* $\rightarrow$ *cis* conversions in each photoexcitation. Representative structures of the coarse-grained model in *trans* and *cis* states are shown on the right panel.

der parameter, S_z, of the simulated glasses as a function of the number of photoexcitation steps; S_z represents the average orientation of transition dipoles for simulated molecules and can be qualitatively compared with the experimentally measured birefringence. Although only small changes in orientation occur for the liquid-cooled glass, they occur much more quickly than for the PVD glasses. SI-Figure 3.13 quantifies photostability using these results, and shows that the simulated PVD glasses are at least 10 times more photostable than the liquid-cooled glass. In addition, the simulation results display a strong correlation between photostability and glass density, in agreement with experiment (SI-Figure 3.13).

The simulation trajectories indicate that the initial molecular packing of higher density glasses restricts excited molecules from reaching the *cis* state, even though their molecular potential strongly favors the *cis* state. The fraction of successful isomerization events is shown as a function of photoexcitation cycles for each glass in Figure 3.6c. This is loosely

equivalent to the quantum yield for the actual photoisomerization reaction. For the highest density glasses, there is a very low probability for a successful isomerization event and this explains the very slow initial changes in the density and S_z parameter.

3.2.5 Mechanism for Enhanced Photostability

We considered two possible mechanisms for the enhanced photostability of high density PVD glasses shown in Figures 3.4 and 3.5. According to one possible mechanism, photoisomerization to the *cis* state occurs only rarely in the highest density PVD glasses (due to efficient packing) but occurs much more frequently in lower density glasses. For the second possible mechanism, we imagine that photoisomerization to the *cis* state occurs efficiently in all glasses, but that only the low density glasses are restructured as a result. We favor the first mechanism and our simulation results strongly support this view. Figure 3.6c shows that, for the highest density vapor-deposited glasses, the isomerization from *trans* to *cis* is nearly completely prevented in the simulations. In the simulation, photoexcitation provides an intramolecular driving force to leave the *trans* state, but in high density glasses, most molecules are unable to reconfigure due to efficient packing. For lower density glasses, the intermolecular barrier for rearrangement will be lower, allowing molecules to achieve the *cis* state with higher probability.

We performed additional experiments to directly test the hypothesis that molecules in a dense glass rarely reach the *cis* state as a result of photoexcitation. DO37 is a "push-pull" azobenzene, and consistent with other azobenzene derivatives of this type, the lifetime of the *cis* state for DO37 is reported to be less than one second.[85] Our efforts to directly detect depletion of the *trans* state in the absorption spectrum during irradiation were unsuccessful, even for the liquid-cooled glass. A reasonable interpretation of these results is that the steady-state population of the *cis* state in our experiments is always quite low. While we expect that the *cis* state population during irradiation is lower for denser glasses than for the liquid-cooled glass, we have not directly established this.

Our proposed mechanism is consistent with literature evidence that the local packing environment can influence the ability of photoexcited azobenzenes to reach the *cis* state. For example, in a glass of 4,4'-diphenyl azobenzene dispersed in amorphous polycarbonate, it was shown that physical aging for 100 hours caused a ∼5% decrease in the photoisomerization quantum yield relative to the glass prepared by liquid-cooling;[121] because a symmetric azobenzene with a long *cis* lifetime was used in this study, this result could be seen directly as depletion of *trans* state absorption. 100 hours of aging likely increases density by much less than 1.3% and this provides a way to understand the much larger effects on photostability obtained in our study with PVD glasses. In another study, azobenzene derivatives were incorporated into different DNA sequences, so that the local packing could be tuned by changing the neighboring base pairs.[37] In this system, it was demonstrated that the quantum yield of azobenzene photoisomerization decreased with increased restriction of molecular packing, varying by a factor of four. Additionally, the photoisomerization of crystalline *trans*-azobenzene is severely hindered in the bulk crystal.[159] These studies all support the idea that the quantum yield for photoisomerization to the *cis* state decreases with increasing intermolecular barriers for molecular rearrangement.

Considering that literature precedents and our simulations both support the view that denser glasses can prevent photoisomerization, it is useful to estimate the magnitude of the intermolecular barriers for rearrangement in PVD and liquid-cooled glasses. Figure 3.7 shows the energy diagram for photoisomerization of an azobenzene in the gas phase and provides background for our discussion. After a 532 nm photon causes excitation to the S_1 state, the molecule relaxes to a twisted configuration ($\theta = 90^\circ$). Upon transition to the ground sate, the molecule either twists forward to the *trans* state or back to the *cis* state, with roughly equal probability.[102] In a glass, in order for an azobenzene molecule to transition from *trans* to *cis*, it must additionally overcome intermolecular barriers in an environment that is quite rigid and essentially static on the time scale of photoexcitation. Using measurements and estimates of the structural relaxation times, we can estimate the activation free energies

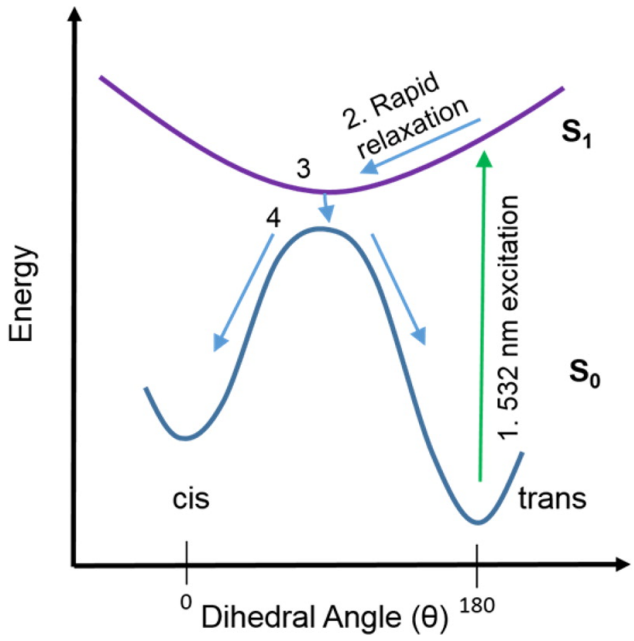

Figure 3.7: Energy diagram of photoisomerization for DO37.

for cooperative rearrangements in the liquid-cooled and PVD glasses to be 34 kT and 51 kT, respectively (see SI). We now imagine adding an intermolecular potential favoring the *trans* state to the diagram in Figure 3.7. As the barrier for rearrangement in the high density glass is a large fraction of the photon energy (94 kT at the experimental temperature), it is plausible that the intermolecular packing blocks any significant progress toward the *cis* state in the dense glass while this mechanism would be less efficient in the liquid-cooled glass. A weakness of this argument is that we have no experimental estimate of the intermolecular barrier associated with photoisomerization, but given the size of the molecular rearrangement required to reach the *cis* state, it is reasonable that it will be not too much smaller than the barrier for structural relaxation. A more detailed theoretical study will be required to examine our proposed mechanism more rigorously.

3.2.6 Mechanical Stress in Films

The change in bulk properties as observed for the density for both the experiments and simulations are examples of a well known "photo-softening" effect for azobenzene contain-

ing glassy materials. Polymer glasses or liquid-crystalline materials containing azobenzene, either covalently bonded into the material or doped within, have been shown to decrease the bulk modulus and induce a type of flow upon photo-excitation below T_g of the material.[79, 42] There is debate as to the specific mechanism of this flow within the literature; however, generally it is thought that the isomerization of the azobenzene units causes an anisotropic stress within the material.[124] To investigate the mechanical stress caused by isomerization within these glass films, the per particle normal stress components were calculated during the isomerization process in the simulations. Each isomerization event, successful or not, excites the selected molecule and puts more energy into the films. Initially for the vapor-deposited glasses the σ_{xx} and σ_{yy} components of the stress tensor within the bulk region go negative and build in magnitude while little change occurs in the density or the average molecular orientation (Fig. 3.8b-d). The σ_{zz} component consistently fluctuates around zero throughout the photoexcitation process, since the free surface allows the system to relax quickly to any perturbation whereas the x and y dimensions are constrained by periodic boundary conditions.

Even though little change occurs in the average molecular orientation or the bulk density of the films during this initial phase for the vapor deposited glasses, there is an instability building within the material. Once these films reach a certain yield stress of about -0.1 LJ reduced units, the film irreversibly transforms towards the relaxed stationary state. After the films have transformed, all the components of the stress tensor fluctuates around zero even while further isomerization events are occurring. It is interesting to note that even in the lower density of the stationary state that all the glasses converge to, only 60% of the selected excited molecules successfully transform to the *cis* conformation (Fig. 3.6). Therefore, in the stationary state there is still local packing that blocks the successful isomerization but the stress induced by the added force is quickly dissipated.

By changing the dihedral potential used for the *cis* state, the driving force and the amount of stress applied to system will change. Four additional *cis* potentials were used on

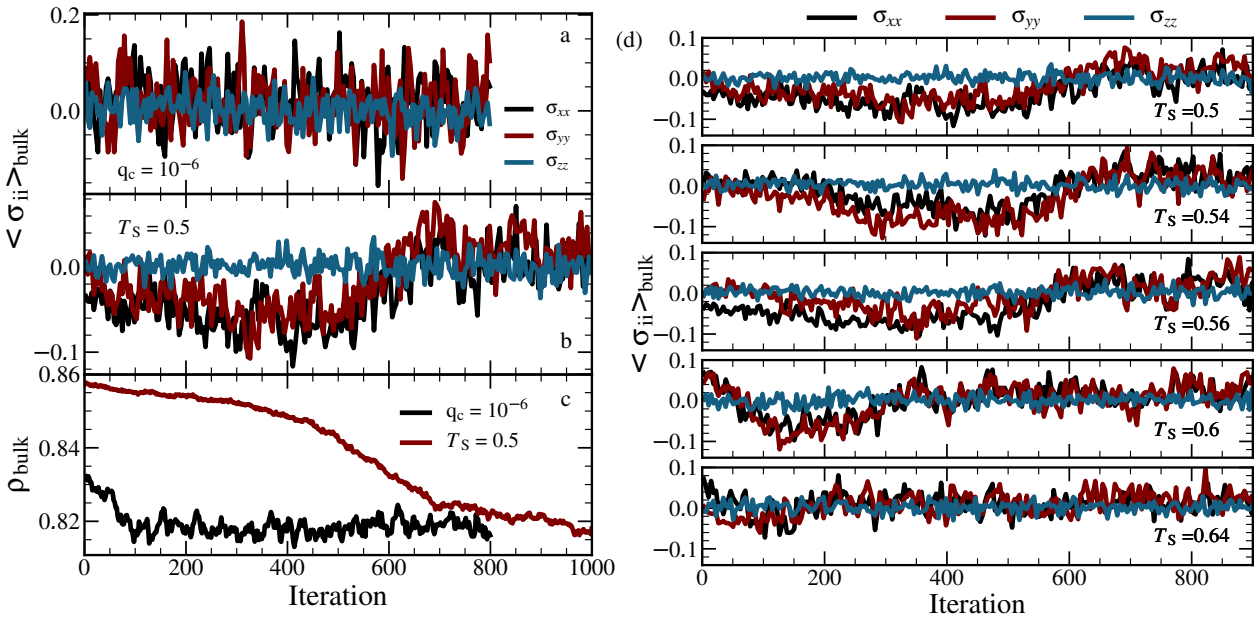

Figure 3.8: Mechanical stress builds during isomerization process. During the initial phase of the isomerization for the vapor-deposited glasses, there is little change occurring in the density or average molecular orientation, but a stress builds within the bulk of the film. The normal stress components of the bulk region (σ_{xx}: black, σ_{yy}: red, σ_{zz}: blue) as function of photoexcitation steps for (a) the liquid-cooled glass and (b) the vapor-deposited glass with $T_\mathrm{s} = 0.5$ ($0.76T_\mathrm{g}$). (c) For comparison, the bulk density (ρ_bulk) from Fig. 3.6 is replotted. (d) The average per particle normal stress components as a function of photoexcitation steps for all T_s studied.

the films deposited at $T_\mathrm{s} = 0.5$ by multiplying either one or both of the dihedral coefficients by 1.5 or 2 (Fig. 3.9a). By only modifying the first coefficient and not the second, the initial plateau around π radians (*trans* state) disappears and a stronger initial force is applied. Even the weakest increase of 1.5 to both coefficients had a drastically reduced lag phase where the stress built in the system (Fig. 3.9b-d). Each potential had the σ_{xx} component of the stress drop to about -0.1 prior to the system relaxing and entering into a stationary state (Fig. 3.9d). The different driving potentials each selected for a different stationary state with different bulk density and percentage of excited molecules successfully transforming to the *cis* conformation (Fig. 3.9e). The stronger potentials force the system to a lower density that allows for a higher percentage of successful isomerization. The lower force of the original potential must stress the system in such a way that it can be dissipated without lowering the

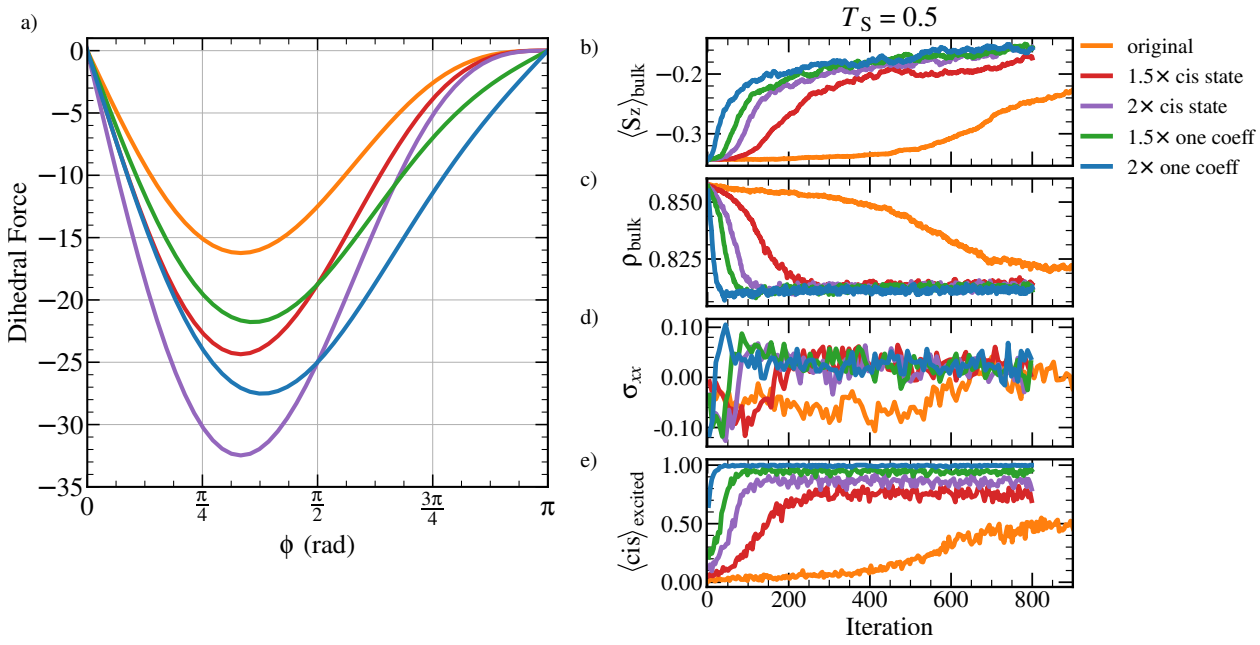

Figure 3.9: Stronger isomerization potentials. A stronger force can be applied which will drive the molecules to more successfully access the *cis* conformation. (a) Four new potentials were applied by either multiplying both coefficients by a factor of 1.5 (red) or 2 (purple) or by multiplying the first coefficient by a factor of 1.5 (green) or 2 (blue). The effect each of the potentials had on the (b) orientation order parameter, (c) bulk density, (d) σ_{xx} stress component, and (e) the proportion of successful isomerizations each iteration.

density or allowing for successful isomerization as the proportion converges to a little more than half. However, due to the strength of the other potentials the only way to dissipate this added energy is to allow for a successful isomerization pushing the system into a lower density to accommodate this.

3.3 Conclusion

In this study, we have established that vapor-deposited organic glasses can be much more photostable than liquid-cooled glasses. While previous work on crystals indicated the important influence of local packing, this is the first demonstration of a significant impact of different amorphous packing arrangements on the photostability of organic molecules. We showed that high density glasses of DO37 can be made by PVD and that the density can be systematically varied through controlling the substrate temperature. The highest den-

sity glass was 50 times more photostable than the liquid-cooled glass and we find a strong correlation between photostability and glass density. We attribute this effect to the high intermolecular barriers for rearrangement that are present in the highest density PVD glasses. This view is supported by molecular simulations of coarse-grained DO37 molecules that successfully reproduced the high density and high photostability of the PVD glasses. The simulations show that, in the highest density glasses, the local packing environment prevents photoexcited molecules from escaping the *trans* configuration.

We expect that enhancement in photostability for vapor-deposited glasses is a general effect that will be observed for many molecular systems beyond the azobenzenes. To date, PVD has prepared glasses with high kinetic stability from more than thirty organic molecules, including several molecules used in the active layers of organic light emitting diodes (OLEDs).[29] In every case where it has been checked, glasses with high kinetic stability also have high density relative to the liquid-cooled glass. Thus we expect that PVD glasses of many organic molecules will show an increased energy barrier for molecular rearrangements that will slow photoreactions. This may be particularly useful in applications where photodegradation leads to deterioration of performance, as in OLEDs and organic photovoltaics. For example, operational lifetime is considered to be a bottleneck to the further improvement of OLED display performance, especially for blue emitters.[24] It has been found that degradation of OLEDs can be caused by self-luminescence,[155] electrochemical reaction[167] and hole injection[108]. We speculate that high density PVD glasses might delay degradation of OLED molecules as a result of any of these processes, as our results indicate that efficient packing can inhibit chemical processes. As OLEDs are already produced by PVD, optimizing the substrate temperature to produce the densest glass might thus increase device lifetime. We do not expect that all organic glasses will show a two order of magnitude enhancement in photostability as a result of optimal vapor deposition. Azobenzenes require a particularly large rearrangement for photoisomerization and it is likely that photodegradation processes that require smaller rearrangements will be less impacted

by the local packing. Future work should investigate the impact of glass packing on a range of different chemical and photochemical processes.

3.4 Experiment and Simulation Methods

3.4.1 Materials

Disperse Orange 37 (99% purity) was obtained from Santa Cruz Biotechnology and used as received. DO37 was selected for these experiments because it has a T_g higher than room temperature; it is a reasonably good glass former, which facilitates glassy thin film preparation via the PVD process. Differential scanning calorimetry (DSC) measurements show that the glass transition temperature (T_g) for DO37 is 296 K, with a 10 K/min cooling and heating rate, which is in good agreement with ellipsometry results. Prior to performing the DSC measurements, the material was first melted then quenched into liquid nitrogen.

3.4.2 Physical Vapor Deposition

PVD was performed in a vacuum chamber with a base pressure of 10^{-7} Torr. Crystalline DO37 was placed in a crucible that was resistively heated. The deposition rate was controlled by tuning the heater power and monitored by a quartz crystal microbalance (QCM). The deposition rate was kept at a constant value of 2 Å/s for all experiments. The final sample thicknesses were about 300 nm. A high throughput method was utilized to prepare a library of glasses with different densities and kinetic stabilities.[27] The substrate (Si wafer) was suspended between two copper fingers; different temperatures were imposed at each finger to create a temperature gradient across the sample during deposition. The substrate temperature range was from 240 K to 305 K.

3.4.3 Kinetic Stability and Density Measurements

Kinetic stability and density of vapor-deposited thin films were characterized by spectroscopic ellipsometry, an optical technique that measures thickness and refractive indices of thin films. For all ellipsometry measurements, three incident angles were used (50°, 60° and 70°), and wavelengths from 370-1000 nm were utilized. To measure kinetic stability, ellipsometry was performed on samples placed on a custom-built hot stage, and the temperature was increased at 1 K/min from near room temperature to 25 K above T_g. The onset temperature, which characterizes the kinetic stability of a glass, was determined from the beginning of the transformation into the supercooled liquid, as shown in Figure 3.1. Immediately after heating, the supercooled liquid was cooled at 1 K/min into the liquid-cooled glass. By comparing sample thickness before and after temperature-cycling, the density of the vapor-deposited glass relative to the liquid-cooled glass can be determined.

3.4.4 Photostability Measurement

The light irradiation experiment used to test photostability of PVD glasses is shown in Figure 3.3. A linearly-polarized 532 nm laser was used as the light source to induce the photoisomerization reaction, at a power level of 11 mW/cm^2. During irradiation, spectroscopic ellipsometry was used to characterize the glass thickness and birefringence, at the same spot where the 532 nm laser irradiated the sample. In this way, photoinduced structural changes of the thin glassy films were monitored in real time. The photostability tests shown in the main text were performed at 287 K (T_g – 9 K). To model the ellipsometric data observed during light irradiation, a biaxial anisotropic Cauchy model was used. This model allows three independent refractive indices, which is necessary since irradiation generates anisotropy in the glass sample along a different axis than the anisotropy generated in the deposition process. In the measurement of photostability, birefringence is defined as the refractive index difference n_z-n_x at 980 nm, where n_z and n_x represent refractive indices for light polarized along the substrate normal and the x direction in the plane of the substrate, respectively;

see Figure 3.3 for coordinate system.

3.4.5 Computer Simulations

Molecular dynamics simulations of a coarse-grained (CG) model of DO37 were performed to study photoisomerization of vapor-deposited glasses at a molecular level. The model consists of four linearly connected Lennard-Jones (LJ) particles (Figure 3.6) with parameters $\sigma_{\mathrm{bb}} = 1.0$ and $\varepsilon_{\mathrm{bb}} = 1.0$. (All units reported for the simulations are reduced LJ units.) The cutoff distance for the potential is $\mathrm{r_c} = 2.5$ with a smooth decay starting at r = 2.4. To mimic the structure of azobenzene, the four particles were held together by three stiff harmonic bonds with the inner bond shorter than the two outer bonds ($l_{inner} = 1.0$, $l_{outer} = 1.5$, $k_b = 1000$). The two bond angles were controlled by a harmonic potential with values that mimic sp^2 hybridization ($\theta = 120^\circ$, $k_{angle} = 1000$). As described below, the dihedral angle potential was switched in order to mimic the photoexcitation process. The dihedral angles for the *trans* and *cis* potentials were defined by:

$$U_{dihedral} = \frac{1}{2}k_1\left(1+\cos\theta\right) + \frac{1}{2}k_2\left(1-\cos 2\theta\right)$$

where $k_1 = 20$ and $k_2 = 8$ for the *trans* state and k_1 = -25 and $k_2 = 6.25$ for the *cis* state.

Vapor-deposited glasses were generated in a simulation box with dimensions of 20 σ_{bb} by 20 σ_{bb} in the plane of the substrate (xy-plane), and at least 10 σ_{bb} larger than the deposited film thickness in the normal direction to the substrate (z-dimension). Periodic boundary conditions were applied to the x and y-dimensions. The substrate was generated from 1,000 randomly placed smaller particles. The potential parameters for the substrate are chosen to minimize any ordering effect on the deposited material while still being able to anchor the growing film.[144] The interaction parameters for substrate atoms are $\sigma_{ss} = 0.6$, $\varepsilon_{ss} = 0.1$, and the interaction parameters for the deposited molecules with the substrate are $\sigma_{sb} = 0.75$ and $\varepsilon_{sb} = 1.0$, with a cutoff distance of 2.5 $\sigma_{\alpha\beta}$, where $\alpha,\beta \in (s,b)$. The substrate

atoms are fixed to their initial position by harmonic springs. The simulated vapor deposition process is analogous to that reported earlier.[88, 89, 144, 135] At least 850 deposition steps were performed for each glass film in order to achieve a film thickness of at least 40 σ_{bb}. The middle section of the film (15 σ_{bb} to 28 σ_{bb} in the z-dimension) was used to calculate bulk glass properties to avoid the influence of the substrate or the free surface. The deposition cycle consists of four repeated steps: (i) introduction of four randomly oriented molecules above, but in close proximity to, the film surface, (ii) equilibration of the newly introduced molecules at high temperature (T=1.25), (iii) linear cooling over 2000 time-units of these molecules to the substrate temperature, and finally (iv) minimization of the energy for the entire system. A separate thermostat is used to maintain the previously deposited molecules and substrate particles at the desired substrate temperature throughout the cycle. For the entire film preparation process described above, the *trans* dihedral potential was utilized. All simulations were performed using the Large-Scale Atomic/Molecular Massively Parallel Simulator (LAMMPS) package[111] in the canonical ensemble with a simulation time step of 0.001 LJ time units. The orientation order parameter, $\mathrm{S_z}$, was used to characterize the average orientation of the simulated films. $\mathrm{S_z}$ is defined as:

$$S_z = \frac{3}{2}\left\langle \cos^2 \delta_z \right\rangle - 1$$

where δ_z is the angle of the molecular end-to-end vector relative to the substrate normal.

An iterative process was used to simulate the photoisomerization reaction. To mimic photoexcitation, a small group of selected molecules have their dihedral angle potential temporarily switched from *trans* to *cis*. During the short molecular dynamics trajectory that follows (mimicking the excited state lifetime), these selected molecules may transition to the *cis* state or their environment may trap them with a dihedral angle close to the *trans* state, i.e., although their dihedral angle potentials were changed to favor the *cis* state, the selected molecules were not forced to the *cis* state. To avoid influences from the interfaces, only the bulk region of the simulated film was considered for the photoisomerization process.

In order to capture the directionality of the polarized light, a director vector was used as a proxy, which pointed 30° off the substrate normal. All photoexcitation simulations were carried out at T=0.6 (0.9 T_g). Each cycle included the following steps: 1) Select a molecule at random; 2) Accept or reject for excitation with probability $\cos^2(\gamma)$, where γ is the angle between the director vector and the end-to-end vector of the molecule; 3) Continue first two steps until 1% of the bulk molecules have been accepted; 4) Switch the dihedral potential for the selected molecules from *trans* to *cis*; 5) Run molecular dynamics for 100 time units; 6) Return all dihedral potentials to the *trans* potential (Fig. 3.10).

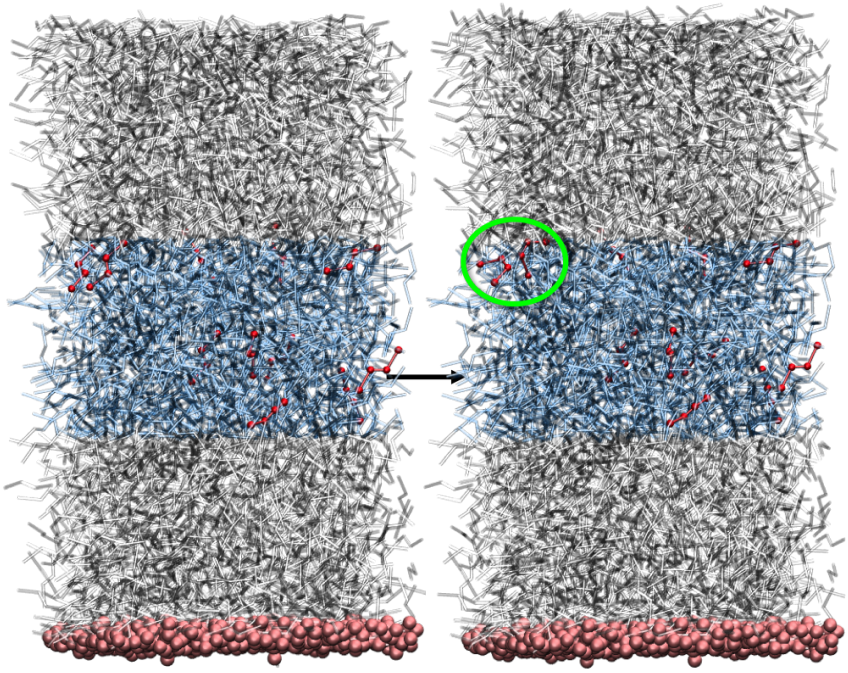

Figure 3.10: The simulated films before (left) and after (right) one iteration simulated photoexcitation. The substrate atoms are colored pink, the coarse-grained azobenzene molecules are colored white and/or blue, where the blue designates the bulk region. Molecules selected for isomerization are colored in red. Two molecules that successfully transformed into the *cis* state are circled.

3.5 Supporting Information

3.5.1 Effect of light polarization on photo-stability of PVD glasses of DO37

In the main text, we demonstrated that PVD glasses of DO37 display significantly enhanced photo-stability in experiments that utilized *s*-polarized irradiation. Here we show that similar photo-stability results in experiments using *p*-polarized light. Figure 3.11 shows the density (ρ) and birefringence (Δn) changes of both vapor-deposited and liquid-cooled glasses as a function of time during *p*-polarized irradiation. For liquid-cooled glasses (black curves), ρ and Δn change immediately after irradiation, on the time scale of tens of seconds. In contrast, PVD glasses change much more slowly. For example, for glasses vapor-deposited at 0.88 T_g (green curves), it takes thousands of seconds for significant changes to occur.

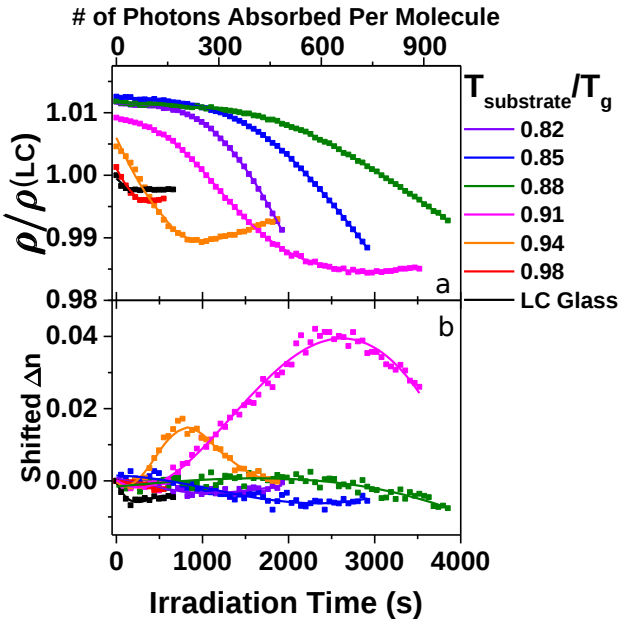

Figure 3.11: *P*-polarized light measurements of photo-stability as a function of irradiation time for vapor-deposited and liquid-cooled (LC) glasses of DO37. (a) Relative density (ρ/ρ(LC)) in comparison to the LC glass. (b) Changes in the birefringence Δn. Lines are guides to the eye.

3.5.2 Initial birefringence of PVD glasses of DO37

For DO37 PVD glasses, initial birefringence depends on the substrate temperature ($T_{\text{substrate}}$). This phenomenon is not unique for DO37, and has been reported for PVD glasses of other molecules.[29, 27, 161] At $T_{\text{substrate}} > T_{\text{g}}$, the initial birefringence is nearly zero, consistent with the random molecular orientation inherited from the super-cooled liquid. At $T_{\text{substrate}} < T_{\text{g}}$, the birefringence of the as-deposited glass is less than zero, which indicates that the molecular axis with maximum polarizability tends to lie in the plane of the substrate. Here birefringence is defined as the difference in refractive index between the extraordinary and ordinary direction of the thin films.

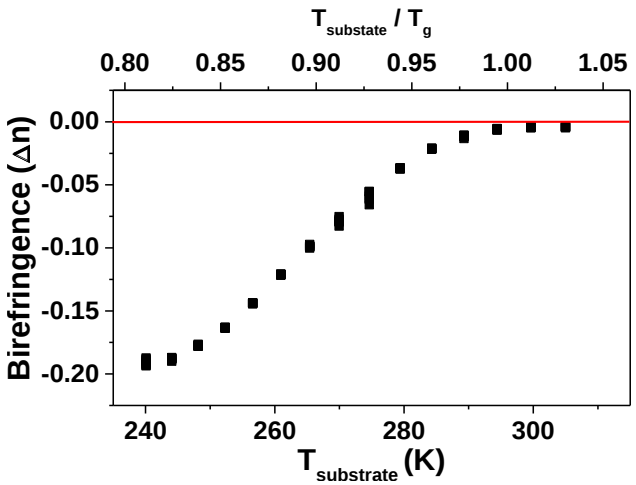

Figure 3.12: Initial birefringence as a function of substrate temperature ($T_{\text{substrate}}$) for vapor-deposited glasses of DO37, as determined by ellipsometry.

3.5.3 Simulation results for the correlation of photo-stability with glass densities

The molecular simulations described in the text show a strong correlation between glass density and photo-stability, similar to the correlation observed in the experiments. Figure 3.13 shows the number of excitation iterations required for 1% density and 5% orientational order parameter (S_z) changes, respectively. The most photo-stable glass is about a factor of 20 slower to isomerize than the liquid-cooled glass. The density for glasses vapor-deposited at different substrate temperatures relative to the liquid-cooled glass are shown in Figure 3.13b. At $T_{\text{substrate}} < T_{\text{g}}$ the density of vapor-deposited glasses is greater than that of the liquid-cooled glass.

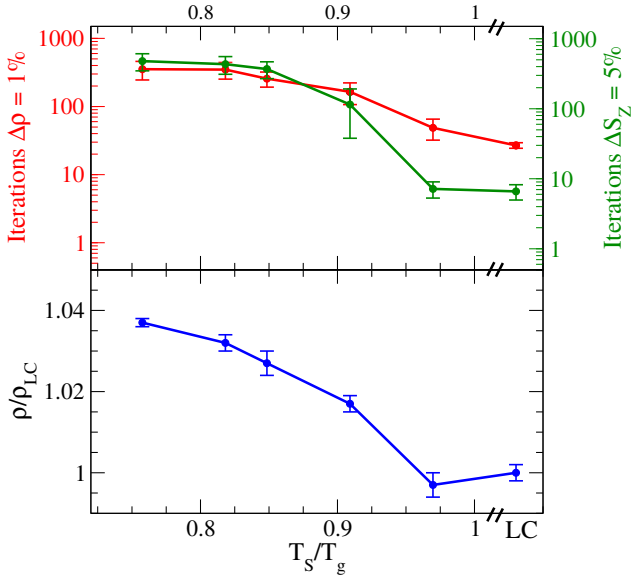

Figure 3.13: Correlation of photo-stability with glass density as a function of normalized substrate temperature for vapor-deposited and liquid-cooled (LC) glasses in computer simulations. (a) Number of photoexcitation iterations required for a 1% change in density (red) and 5% change in the order parameter (green). (b) Density of as-deposited (AD) glasses relative to the LC glass.

3.5.4 Stable glass photo-stability at a lower measurement temperature

In the main text, all the photo-stability data presented was collected during irradiation at 287 K, which is 9 K below the T_g. Here we show that, when the measurement temperature is lowered to 278 K, the PVD glass shows almost no difference in photo-stability. Figure 3.14 shows the density (ρ) and birefringence changes (Δn) during light irradiation for DO37 films vapor-deposited at $T_{substrate} = 0.91T_g$. The time required for changes of 0.1% in density, and 0.005 in birefringence, are nearly the same for the two measurements.

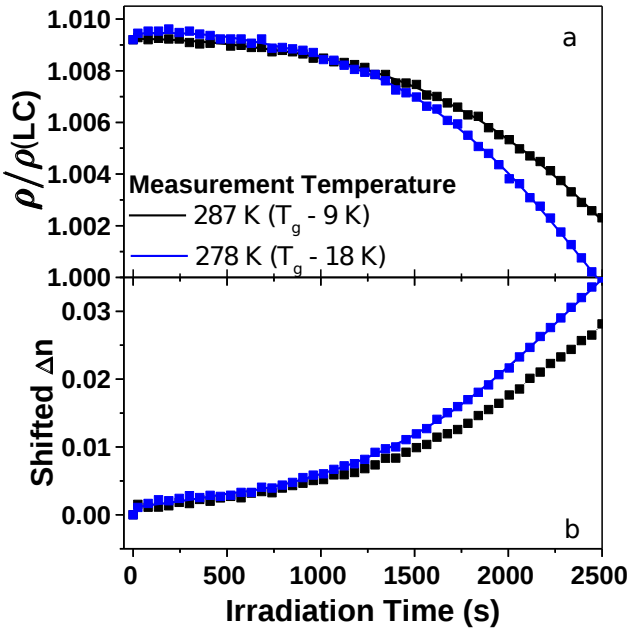

Figure 3.14: Photo-stability as a function of irradiation time for glasses vapor-deposited at $T_{substrate} = 0.91\ T_g$ at different irradiation temperatures. (a) Relative density (ρ/ρ(LC)) changes (b) Birefringence (Δn) changes. Lines are guides to the eye.

3.5.5 Liquid-cooled glass photo-stability at different measurement temperatures

The photo-stability of liquid-cooled glasses was assessed at different irradiation temperatures. We observe in Figure 3.15 that photo-induced changes in ρ and Δn are accelerated at lower temperatures. Lowering the temperature from 287 K to 278 K speeds photo-induced changes in liquid-cooled glasses by about a factor of two.

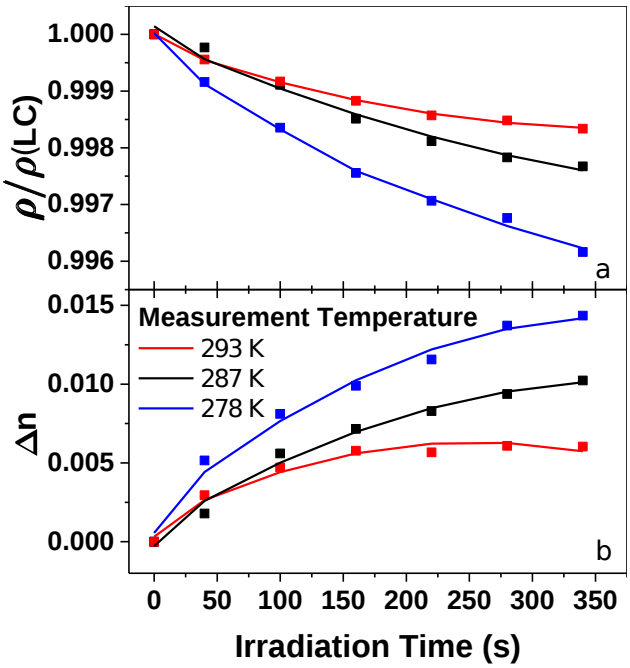

Figure 3.15: Photo-stability as a function of irradiation time for liquid-cooled (LC) glasses at different irradiation temperatures. (a) Change in relative density. (b)Change in birefringence Δn. Lines are guides to the eye.

3.5.6 Simulated liquid-cooled glass transition at different cooling rates

For comparison with the experiments, the glass transition temperature of a film of coarse-grained DO37 molecules was determined for the simulations as shown in Figure 3.16. In the figure, one can see the cooling rate dependence of T_g. The T_g corresponding to the slowest cooling rate is used in the main text and elsewhere in the supporting information. The cooling rates (q_c) are presented in units of LJ temperature/LJ time-unit.

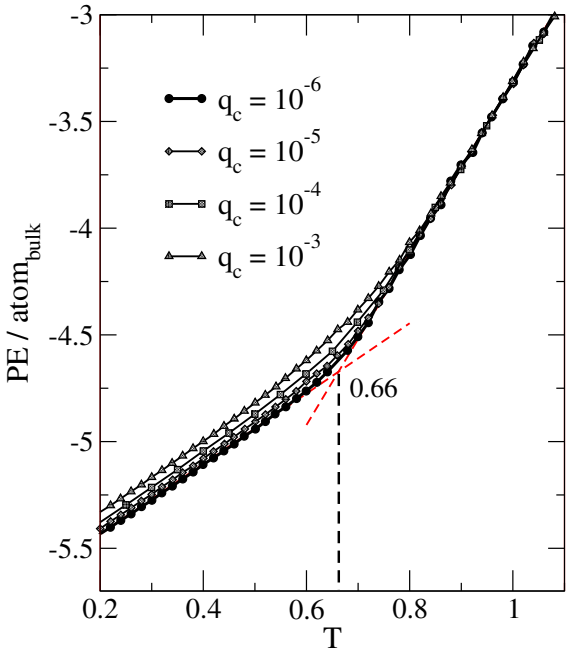

Figure 3.16: The intensive potential energy was calculated for the bulk region as a function of temperature. Four different quenching rates (q_c) were used. The glass transition temperature (T_g) was calculated from intersection of the liquid and glass lines as shown.

3.5.7 Properties of simulated vapor deposited glasses

Simulated vapor depositions were performed at various substrate temperatures ranging from 0.76 T_{g} to 0.97 T_{g} as described in the main text. For each substrate temperature, five sample films were produced. To compare the properties of the vapor-deposited films to the liquid-cooled glass, the average inherent structure energy and the average density are calculated; both of these quantities are evaluated in the bulk portion of the film. Table 3.1 compares these properties with the liquid-cooled glasses prepared at the three lowest cooling rates. All the vapor deposited glasses have higher density and lower inherent structure energies. The liquid-cooled glass at the lowest cooling rate is used as a reference point.

$\boldsymbol{T_s/T_g}$	$\boldsymbol{E}_{\mathrm{IS}}$	$\boldsymbol{\rho/\rho_{LC}}$
0.76	-0.244 ±0.010	1.037 ±0.001
0.82	-0.229 ±0.002	1.032 ±0.002
0.85	-0.210 ±0.010	1.027 ±0.003
0.91	-0.139 ±0.013	1.017 ±0.002
0.97	-0.004 ±0.008	0.997 ±0.003
$\mathbf{q_c}$		
10^{-6}	0.000 ±0.002	1.000 ±0.002
10^{-5}	0.026 ±0.006	0.997 ±0.002
10^{-4}	0.056 ±0.002	0.993 ±0.002

Table 3.1: Comparison of CG-4mer vapor deposited glasses and liquid-cooled glasses. The substrate temperatures $T_{\mathrm{substrate}}$ are all relative to T_{g} (0.66) and there are three different quenching rates (q_c) in terms of LJ temperature/LJ time-units. The inherit structure energies (E_{IS}) are all shifted such that the slowest q_{c} is the zero energy point. The densities (ρ) are reported relative to the slowest q_{c}. Error reported by calculating the standard deviation from five independent films.

3.5.8 Estimation of the activation free energy associated with glass packing:

We estimate the activation free energy for molecular rearrangements in the glass by utilizing the temperature dependence of the structural relaxation or alpha relaxation time (τ_α). τ_α is the characteristic time for intermolecular rearrangements in supercooled liquids and glasses. At T_g, the supercooled liquid has a τ_α that is equal to 10^2 s. At infinitely high temperature, $\tau_{\alpha,\infty}$ is estimated to be about 10^{-13} s, which represents the fastest movement that a molecule can achieve in the condensed phase. From the following equation,

$$\ln \tau_\alpha \left(T_g\right) = \ln \tau_{\alpha,\infty} + E_a/kT_g$$

we estimate the activation free energy for the supercooled liquid at T_g to be about 34 kT_g. Since the liquid-cooled glass inherits its structure from the supercooled liquid at T_g, 34 kT_g ($\cong 34kT_g$ at the irradiation temperature) is also a good estimate of the activation free energy for molecular rearrangements in the liquid-cooled glass.

For the highest density glass of DO37, we use previous measurements on indomethacin to estimate the activation free energy. Both DO37 and indomethacin have the same optimum deposition temperature (0.85 T_g) and show similar density increases compared to the liquid-cooled glass. For indomethacin, τ_α at the temperature of preparation (0.85 T_g) can be estimated to be 10^{13} seconds.[31] Using this value and the following equation,

$$\ln \tau_\alpha \left(0.85T_g\right) = \ln \tau_{\alpha,\infty} + E_a/\left(0.85kT_g\right)$$

we estimate the activation free energy for the highest density PVD glass at about 51 kT_g ($\cong 51kT_g$ at the irradiation temperature.)

CHAPTER 4

DYNAMIC ACTUATION OF GLASSY POLYMERSOMES THROUGH ISOMERIZATION OF A SINGLE AZOBENZENE UNIT AT THE BLOCK COPOLYMER INTERFACE

In this chapter a thin glassy layer is created and manipulated for controlled nano-encapsulation and release. An amphiphilic block copolymer, *b*-PEG-azoB-PLA, with hydrophilic polyethyleneglycol (PEG) and the hydrophobic poly-DL-lactide (PLA) blocks connected by an azobenzene unit was synthesized and shown create vesicular assemblies. We were able to encapsulate guest molecules into the interior lumen of the vesicles or within the hydrophobic membrane of the polymersomes. Using dye as the guest molecules, we demonstrate that with photo-excitation of the azobenzene group these vesicles will either leak their contents (during photo induced isomerization) or remain tightly sealed (no irradiation). Combining experimental interrogation and molecular simulations of the formed bilayers, we evaluate the possible mechanisms for this controlled release and investigate the physical features of import in the system. For instance, the PLA is found to form a glassy thin film which acts as both a strong barrier to leakage but also acts as a conduit for propagating the mechanical disturbance of photoisomerization.

All experiments and synthesis were performed by Dr. Mijanur Rahaman Molla and Dr. Poornima Rangadurai and the computational studies were all developed and performed me.

Mijanur Rahaman Molla[†], Poornima Rangadurai[†], Lucas Antony[†], Subramani Swaminathan, Juan de Pablo, S. Thayumanavan "Dynamic actuation of glassy polymersomes through isomerization of a single azobenzene unit at the block copolymer interface". *Nature Chemistry* (2018) DOI:10.1038/s41557-018-0027-6

[†]contributed equally

4.1 Introduction

Nature relies on specific molecular recognition events on a cellular surface to transmit signals from the extracellular space into the intracellular lumen. Inspired by these innate abilities of biological systems, here, we have sought to develop a robust, reversible system where highly localized conformational transitions at an interface propagate throughout a material. We utilize azobenzene to disrupt the interface's fidelity owing to its reversible photo-induced configurational change. Azobenzene-based homopolymers have been exploited for photo-induced changes in volume and shape of the soft materials, in addition to their dichroism and birefringence.[103, 157] In this report, we rely on a different mechanism, namely the sensitivity of non-equilibrium glassy films to interfacial mobility, to achieve unique photo-induced mechanical effects with extremely low loadings of azobenzene (just one unit per polymer chain), and in the self-assembled solution state. Recent studies show that high interfacial mobility can lead to well-equilibrated glasses, where the structure of the interface can be imprinted into the bulk material.[141, 135, 29] There are also recent reports on photo-softening of vesicles, and directional softening of liquid crystalline systems due to azobenzene photoisomerism.[158, 48] Here we turn that concept around, and show that by targeting the interface of a pre-formed glassy material selectively, one can create mobility fronts that propagate across the material, leading to transport processes that can be activated or turned off, through the application of external cues. We refer to this process as interface-induced dynamic facilitation. Azobenzene-containing assemblies have been studied for photoinduced morphoplogical changes.[38, 154, 86, 44, 77] We have taken it a step further to investigate in detail the mechanical property changes responsible for reversibly stabilizing and breaching the membrane. We demonstrate that the light-induced isomerization of functional groups confined into a molecularly thin layer at the interface of a supramolecular assembly can cause pronounced ripple effects that are transmitted over long length and time scales across a glassy polymeric membrane. The proof-of-concept principles proposed here present new avenues for reversible breaching of polymer-based membrane barriers.

4.2 Results and Discussion

An amphiphilic block copolymer, *b*-PEG-azoB-PLA (**P2**, Figure 4.1a), with hydrophilic polyethyleneglycol (PEG) and the hydrophobic poly-DL-lactide (PLA) blocks, was targeted with an azobenzene unit at the interface (M_n(NMR) = 16,000 g mol^{-1}, PDI = 1.32, weight fractions: 29% PEF; 71% PLA) (Fig. 4.1 and SI-Fig. 4.22). Self-assembly of **P2** was achieved via a co-solvent method to attain ∼140-150 nm vesicles with a bilayer membrane thickness of ∼8 nm, as verified using transmission electron microscopy (TEM) (Fig. 4.1b). Dynamic light scattering (DLS) suggested the presence of spherical aggregates with an average hydrodynamic diameter (D_h) of ∼165 nm (Fig. 4.1c). With the radius of gyration (R_g) from static light scattering (Fig. 4.1d), the R_g/R_h ratio of 0.93 shows that these are indeed hollow spherical particles.[110] The morphology was further supported by atomic force microscopy (AFM) (SI-Fig. 4.8) and comparative ^{1}H NMR in D_2O and $CDCl_3$ (SI-Fig. 4.9).

The vesicular-construct offers to validate the interfacial actuation ideas proposed here through simple, cross-membrane molecular transport measurements. We examined whether the membrane could serve as a reservoir for hydrophobic molecules (Fig. 4.2a) by incorporating water-insoluble 1,1'-dioctadecyl-3,3,3',3'-tetramethylindocarbocyanine perchlorate (DiI) within it. Although the resolution of fluorescence optical polarization microscope (OPM) does not allow for determining the precise location, the red emitting spherical particles confirmed the dyes presence within the assembly (Fig. 4.2d). Both absorption and emission intensities of the encapsulated DiI did not change over 15 days, suggesting high encapsulation stability, comparable to covalently crosslinked assemblies (Fig. 4.2b,c).[105]

The aqueous lumen inside these vesicular assemblies can also accommodate hydrophilic molecules, such as rhodamine 6G (R6G). After encapsulation, the fluorescence of the dialyzed solution was evaluated to confirm the presence of R6G inside the lumen. The emission intensity of R6G at 555 nm is much lower within the assembly than the absorbance-matched free dye in aqueous phase (Fig. 4.2f, g), which is attributed to encapsulation-induced increase in local concentration of the self-quenching R6G.[81, 125] OPM images further confirm R6Gs

presence within the assembly interior (Fig. 4.2h). The high stability of encapsulation with R6G, too, suggests that the amphiphilic polymer at the interface provides a robust barrier for molecular transport across the membrane.

The morphology of the assembly localizes the photosensitive azobenzene[11] unit at the interface between the membrane and the aqueous phase in both the lumen and the bulk media, as shown in Figure 4.1a. Irradiation of the solution with a 360 nm light (photon flux 10^{16} $cm^{-2}s^{-1}$, 2 mW power, 5.55 $mW{\cdot}cm^{-2}$ density) for 4 hours, resulted in a gradual decrease in DiI absorbance (Fig. 4.2j, k) indicating release of the hydrophobic molecule (SI). No such release was observed from the assembly in dark (SI-Fig. 4.10). Similar irradiation caused negligible changes in cetyltrimethylammonium bromide micelles, suggesting that the decrease is not due to photobleaching of DiI (SI-Fig. 4.10). These results provide the first indication that the observed molecular release may be attributed to the photoinduced *trans-cis* isomerization of azobenzene.

A plausible explanation for the observed release could be that the *cis*-azobenzene polymer, formed during photoisomerization, is not a good host for DiI; because of *cis*-azobenzenes higher dipole moment by 3.0 D, which renders *cis* to be less hydrophobic than the *trans* form.[94] However, the typical quantum yield of small molecule azobenzene photoisomerization is ∼0.3-0.7.[47, 7] At the irradiation fluence used, this isomerization should be complete in less than one second. Even possible reductions in quantum yield due to incorporation into a polymer fail to explain the molecular release that is sustained over 3-hours. Alternatively, it is possible that the molecular release occurs only during the isomerization process. If the former scenario was the operating mechanism, then upon irradiating the sample for a short time the assembly would continue to release guest molecules in the dark, because the initial isomerization required to compromise the membrane barrier would have been achieved. In the latter scenario, molecular release would depend on the presence of light, ceasing when the light is off, and restarting when the light is back on. To distinguish between these two limiting possibilities, the DiIloaded vesicles were irradiated for an hour, at which time

there was ∼40% molecular release (Fig. 4.3a, b). The solution was monitored for further release in dark for 2.5 hours, during which no change was observed. When the irradiation was restarted, the molecular release indeed resumed. Here, the work is performed through an energy input, falling back into a dynamically-arrested glassy state in its absence. This behavior is reminiscent of other systems that operate far from equilibrium.[45, 15, 92]

It is conceivable that a perturbation at the interface of the block copolymer could cause molecular release, since the hydrophobic guests are right at the interface in the membrane. It is also interesting to investigate the effect of interfacial activation on the entire membrane barrier, *i.e.* the effect on the encapsulation stability of the hydrophilic guests in the aqueous lumen. Temporal release of hydrophilic R6G was indeed observed upon continuous irradiation at 360 nm, which is measured as increased fluorescence due to decreased self-quenching upon release (Fig. 4.2f, g); further evidence for release was obtained through OPM imaging (SI-Fig. 4.11). The molecular release occurred only when the light was on, confirming non-equilibrium behavior (Fig. 4.3e, f). These experiments indicate that the localized, molecular-level actuation event that occurs at the interface of the glass can propagate through the membrane and induce diffusion through an otherwise glassy material.

Visible light irradiation (2 mW, 450 nm) also resulted in the release of ∼80% DiI molecules over a period of 480 minutes (Fig. 4.2l, m). The rate of release was slower, relative to 360 nm, which is attributed to the lower absorptivity of azobenzene at higher wavelengths. To test this idea, we evaluated the release rate with higher number of lower energy photons. Indeed, the release rate increased (SI-Fig. 4.12), likely due to the higher number of molecules undergoing photoisomerization. When irradiated at 650 nm, where azobenzene does not undergo photoisomerization. We did not observe any guest release even at 6 mW power (SI-Fig. 4.12). Also, the size and morphology of the assemblies before and after exposure to light remained intact (SI-Fig. 4.13). Collectively, these observations demonstrate that these supramolecular vesicles release their guest molecules only during active photoisomerization.

The following two limiting mechanistic possibilities can be invoked to interpret the ob-

served behavior: (*i*) the azobenzene chromophore in **P2** contains an amine donor and a carboxylic ester acceptor, which makes it a donor-acceptor chromophore. The barrier for thermally activated *cis* to trans back-isomerization is known to be low for such donor-acceptor chromophores.[104] Therefore, the photo-generated *cis* isomer can convert rapidly back to the trans form. In this scenario, if this transient *cis* isomer does not form a stable assembly, it causes the molecular release to occur far from equilibrium through rapid forth-and-back transitions that become a source of mobility at the interface; (*ii*) The photoinduced isomerization process at the interface causes a change in the hydrophobic packing, thereby compromising the integrity of the membrane barrier through fluctuations of density.

Typical azobenzene absorption maximum is centered around 350 nm for the *trans* isomer and ∼450 nm for the *cis* form, attributed to their π-π^* and n-π^* transitions respectively. But these spectral bands are known to overlap for the push-pull azobenzenes.[104] The absorption, corresponding to the azobenzene unit, did not change in response to 360 or 450 nm irradiation (SI-Fig. 4.13). This result supports the first mechanistic pathway proposed above. However, this behavior by itself does not suggest that the possible transient *cis* isomer is the reason for the observed actuation behavior. To test this, polymer **P4** was synthesized where both phenyl rings in azobenzene contain alkoxy units (SI-Scheme 4.6, Fig. 4.4e). The lack of donor-acceptor character and the increased bond length alternation[90] allows for the discrete formation and characterization of the *trans* and *cis* azobenzene based polymers. Polymer **P4**, which self-assembles similar to **P2** into ∼135 nm vesicles (SI-Fig. 4.14), exhibited an absorption maximum at ∼340 nm corresponding to the *trans*-azobenzene. Photoirradiation of the vesicular assembly in aqueous phase resulted in a decrease in absorption at 340 nm with a concurrent increase at ∼440 nm, which corresponds to the *cis* isomer (SI-Fig. 4.14). The photostationary *cis*-rich state was reached in less than 5 minutes. As anticipated from the electronics of the substituents, the *cis*-isomer did not thermally relax back to *trans*-isomer even after 4 hours (SI-Fig. 4.14).

If the transient formation of the *cis*-isomer is the reason for the poor membrane fidelity in

the **P2** assembly, then the stable formation of the *cis* isomer in **P4** should cause continuous release of the guest molecule even in dark. However, here too, both hydrophobic molecular release from the membrane and hydrophilic molecular release from the lumen were found to be dependent on energy input. When the irradiation discontinued (*cis*-rich state), there was no molecular release, but resumed upon restarting the photo-irradiation (Fig. 4.4a-d). This non-equilibrium behavior is independent of whether the resting state of the assembly is the *trans*- or the *cis*-isomer. These results unambiguously rule out the transient isomer formation hypothesis.

The results above serve to underscore our hypothesis that isomerization-induced interfacial mobility leads to transient relaxation of the glassy membrane material in the presence of light. To further substantiate this hypothesis, molecular dynamics (MD) simulations were performed on the assemblies described above. In our calculations, the PLA block constitutes the hydrophobic membrane barrier. This block is particularly sensitive to the disruption caused by the surface activation at the block copolymer interface. Therefore, factors that affect the packing and permeability of this block in its self-assembled state are of interest. Simulation studies were performed using the all-atom optimized potential for liquid simulations (AA-OPLS) force field with TIP4P water model.[72, 69] Each polymer consisted of 20 ethyleneglycol monomers in PEG, along with hydrophobic blocks varying in size of with 20 to 50 lactide monomers (as defined in Fig. 4.1a), respectively. Due to system size constraints for atomistic simulations, we focused on a small section of the bilayer (Fig. 4.4k). Pristine PLA has an experimental T_g in the range of 330 K to 345 K[39, 5] and the experimental T_g of PLA in **P1** was found to be slightly lower, consistent with that found in the case of PLA in block copolymers.[163, 168] To account for the T_g of PLA, an annealing run was performed from 450K to 298K. An iterative procedure was used to simulate photo-excitation and isomerization, where the stochastic nature of photo-excitation was not enforced, given the time scales accessible to simulations, and the focus was on the structural and dynamic changes that occur during successful isomerization events.

The glass transition and glassy nature of materials all depend on the observation timescales. In all-atom simulations, these timescales are on the order of nano-seconds, which are much shorter compared to those in experiments. Therefore, the T_g in all-atom simulations is generally calculated as the lowest simulated fictive temperature (T_f) for the material, *i.e.*, as the intersection of the equilibrium super-cooled liquid extrapolated to lower temperatures, and the glass line extrapolated to higher temperatures. For PLA, the T_f was calculated by examining the density of the system and the Debye-Waller (DW) factor for PLA as a function of temperature, evaluated during the cooling of the 20-unit PLA chains (SI-Fig. 4.16). The average mean-squared-displacement of the hydrogen atoms for a set Δt=10 ps was used to calculate the DW factor, which provides a measure of local mobility. A T_g of 390 K was estimated from our simulations, which is approximately 45-60 K higher than the experimental T_g for the polymer (SI-Fig. 4.16). This difference is expected for all-atom simulations – when one considers that T_g is known to change by approximately 3 to 5 K per decade of cooling rate. The mobility of the water molecules in and through the bilayer is not only dependent on the temperature of the system, but is also strongly dependent upon whether the PLA is in a glassy state or not. Once the PLA falls out of equilibrium and enters a glassy state, the mobility of the water in the PLA decreases drastically. Rather than being diffusive, water motion consists of rare hopping events, which are characteristic of transport in glassy polymers (SI-Fig. 4.16).

The mobility of various components of the system was calculated throughout the photoexcitation process. In Figure 4.4l-n, the mobilities of the PLA molecules and water within the PLA region were calculated as a function of time for the 20-unit chains. During the 20 ns prior to the light perturbation, there is little change in the DW factors for either the PLA or the water within the PLA region. Once the photo-excitation process is initiated, both DW factors increase appreciably, in a step-like manner (Fig. 4.4m,n). After the photoexcitation process is over, the DW factors of the PLA and water contained within the PLA region relax to their original value, before the excitation process. The increase in DW factors depends

on the proportion of azo groups undergoing isomerization (Fig. 4.4m,n). Such increases are appreciable; if one estimates the temperature change that would be necessary to achieve a comparable DW factor increase and finds that the change should be on the order of tens of degrees (SI-Fig. 4.16). Note that similar effects are observed for the two higher molecular weight systems considered in this work (SI-Fig. 4.19).

These results show that the photoinduced isomerization event causes an increase in the mobility of the azo groups, which then propagates to the PLA, thereby increasing the mobility of water in the PLA region. These mobilities can be reasonably implicated in the triggered compromise of the hydrophobic barrier that facilitates cross-membrane transport of water-solvated and membrane-bound molecules. Note that, in our experimental system, additional effects could further increase the enhanced mobilities themselves, such as the possible local heating caused by the non-radiative, thermal relaxation of the photoexcited azobenzene moieties at the interface of the polymer. In simulations however, the temperature is deliberately held constant through the use of a thermostat, and the increased mobility throughout the PLA domain is caused by the mechanical actuation, induced through the isomerization events at the interface. Note that in this process of interface-induced dynamical facilitation, only a subset of the azobenzene groups located in a molecularly thin layer need be isomerized in order to enhance mobility and transport. To test the possibility of thermal effects, simulations were performed without a thermostat in the microcanonical ensemble. A temperature increase of 1 K for the system was observed during the isomerization (SI-Fig. 4.18). This temperature increase is easily absorbed by having a thermostat act on the water molecules and, given the thermal diffusivity of water and PLA, it is dissipated on the timescale of a few pico-seconds (SI-Fig. 4.18). A temperature rise of such a small magnitude is unlikely to enhance mobility considerably beyond the effects that are attributable to mechanical actuation alone.

To experimentally test this theory, *i.e.* whether molecular release can be achieved by simply taking PLA above its T_g due to local heating, hydrophobic molecular release from

the membrane and the hydrophilic molecular release from the lumen of the assembly were monitored at different temperatures. Even at temperatures above the T_g of PLA, there was no molecular release in either of these cases (Fig. 4.4i). A control PEG-PLA block copolymer without the photoactive azobenzene at the interface was synthesized (Fig. 4.4g, SI-Scheme 4.7) and hydrophobic azobenzene small molecules were non-covalently incorporated as guest molecules, along with DiI, within the vesicular membrane of this polymer (Fig. 4.4f, SI-Scheme 4.7). When these non-covalent azobenzenes are photoexcited, the non-radiative, thermal relaxation of these guest molecules did not cause local heating of the PLA domains, as there was no molecular release from the membrane (Fig. 4.4 4h). Additional support for our photo-activated molecular release kinetics comes from experiments at different temperatures. The molecular release process exhibits a linear Arrhenius behavior, including in the temperature range above and below the T_g of PLA (SI-Fig. 4.15). Here it is important to note that transport in glasses generally exhibits an Arrhenius temperature dependence in the vicinity of the glass transition temperature, consistent with our experimental observations. Moreover, there is evidence within the literature of athermal photo-fluidization, where the isomerization of azobenzene causes a glassy system to flow without a measurable temperature increase.[42, 113] We therefore view our proposed explanation of mechanical actuation at the interface as the operating mechanism for the observed processes.

Finally, we demonstrate the potential utility of this molecular scale actuation-based, nonequilibrium process can result in a macroscopically observable event. Here, we protect one of the two reactive components in the assembly, which is then released on-command to encounter its complementary reactant. Hexamathylene diamine was encapsulated within the aqueous lumen of the supramolecular capsule, while sebacoyl chloride was dissolved in hexane. If unprotected in a biphasic mixture, these two components rapidly react at the interface to produce nylon. However, since the diamine is protected by the capsule membrane, no nylon formation was observed. Upon exposure to light to actuate the membrane, rapid formation of nylon is indeed seen. This process can be iteratively performed to control the

degree of nylon formation, until the diamine is exhausted in the assembly. Overall here, we cause a molecular scale configurational change in an azobenzene unit (∼1 nm) to cause mobility fronts in a membrane (few nm), which causes a nanoscale vesicle (∼100 nm) to leak its contents and generate nylon fibers (μm thick and mm long). In addition to bridging the length scales, the truly biomimetic feature of this demonstration also arises from the fact that this transformation is carried out far-from-equilibrium.

4.3 Conclusions

Our results show that a single functional group at the hydrophobic/hydrophilic interface of a membrane can be utilized to dynamically propagate a molecular level actuation event across a glassy polymeric nanomaterial. In this work, we introduce a novel mechanism for actuation of glassy materials at interfaces. We show that actuation about a single chemical bond can cause perturbations of a membrane that are felt over distances that surpass 500 chemical bonds in the PLA domain. The fact that the membrane barrier is activated only in the presence of an energy input also suggests that these events take the system into an active, out-of-equilibrium state that can be turned off in the absence of external cues. Computer simulations have been used to establish a detailed correspondence between the surface-induced activation mechanism and the dynamic facilitation that is observed in homogeneous glass films. In the systems considered here, we propose that in the absence of light activation, the azobenzene groups are tightly packed and create an interface of low mobility. Upon isomerization, the interface undergoes a sudden increase of mobility that rapidly propagates into the bulk of the PLA-based glassy membrane, partly as a result of the oriented nature of the PLA chains in the assemblies considered here. The principles developed here have implications in applications such as controlled release and cryptic catalysis.

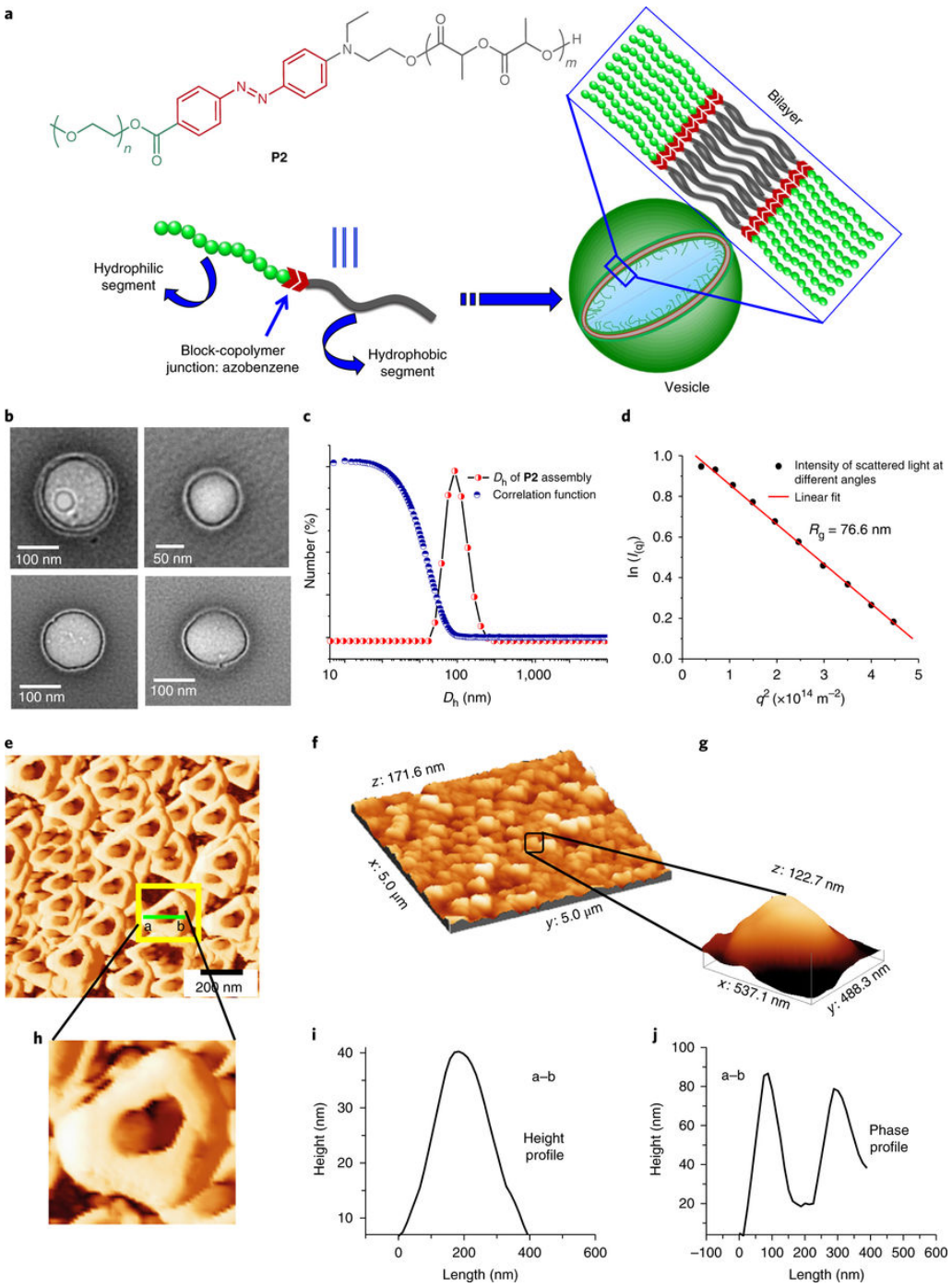

Figure 4.1: Structure and characterizations of the block copolymer, P2 **a.** Chemical structure of the block copolymer **P2** and cartoon representation of the vesicle with zoomed region representing bilayer formation. **b.** TEM images of self-assembled **P2** polymer, negatively stained with uranyl acetate. **c.** Size distribution and autocorrelation function of **P2** aggregates determined by DLS in aqueous medium. **d.** Partial Zimm plot to determine radius of gyration, R_g. **e** and **f.** AFM phase and height images of **P2** vesicle. **g** and **h.** Zoomed version of one vesicle. **i**, AFM height profile. **j.** AFM phase profile. a-b is the line drawn on a vesicle for cross-sectional analysis.

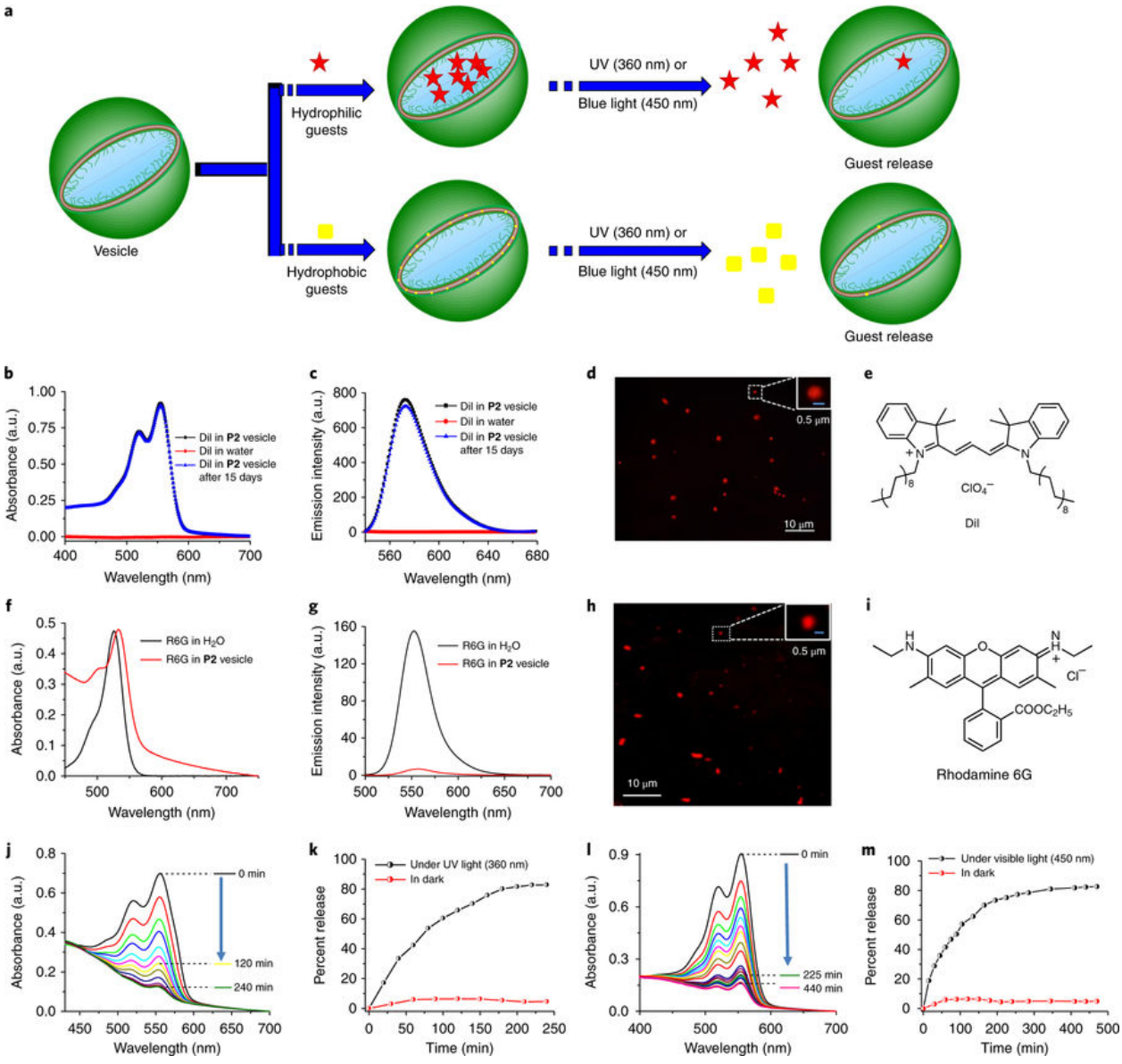

Figure 4.2: Encapsulation ability and stimuli-responsive behavior of P2 vesicles **a.** Schematic representation of hydrophilic and hydrophobic guest encapsulation and release from **P2** vesicles, stars indicate hydrophilic guests and squares indicate hydrophobic guests. **b.** Absorption and **c.** Emission spectra of DiI encapsulated **P2** vesicles **d.** OPM image of DiI loaded vesicle. **e.** Chemical structure of DiI molecule. **f.** Absorbance matched spectra and **g.** Emission spectra of R6G in water and R6G in **P2** vesicles. **h.** OPM image of the R6G encapsulated **P2** vesicles. **i.** Chemical structure of R6G. **j.** Decrease of DiI absorption intensity with time in presence of UV light and **l.** Visible light from **P2** v. **k.** % release of DiI in presence of UV light and **m.** visible light from **P2**.

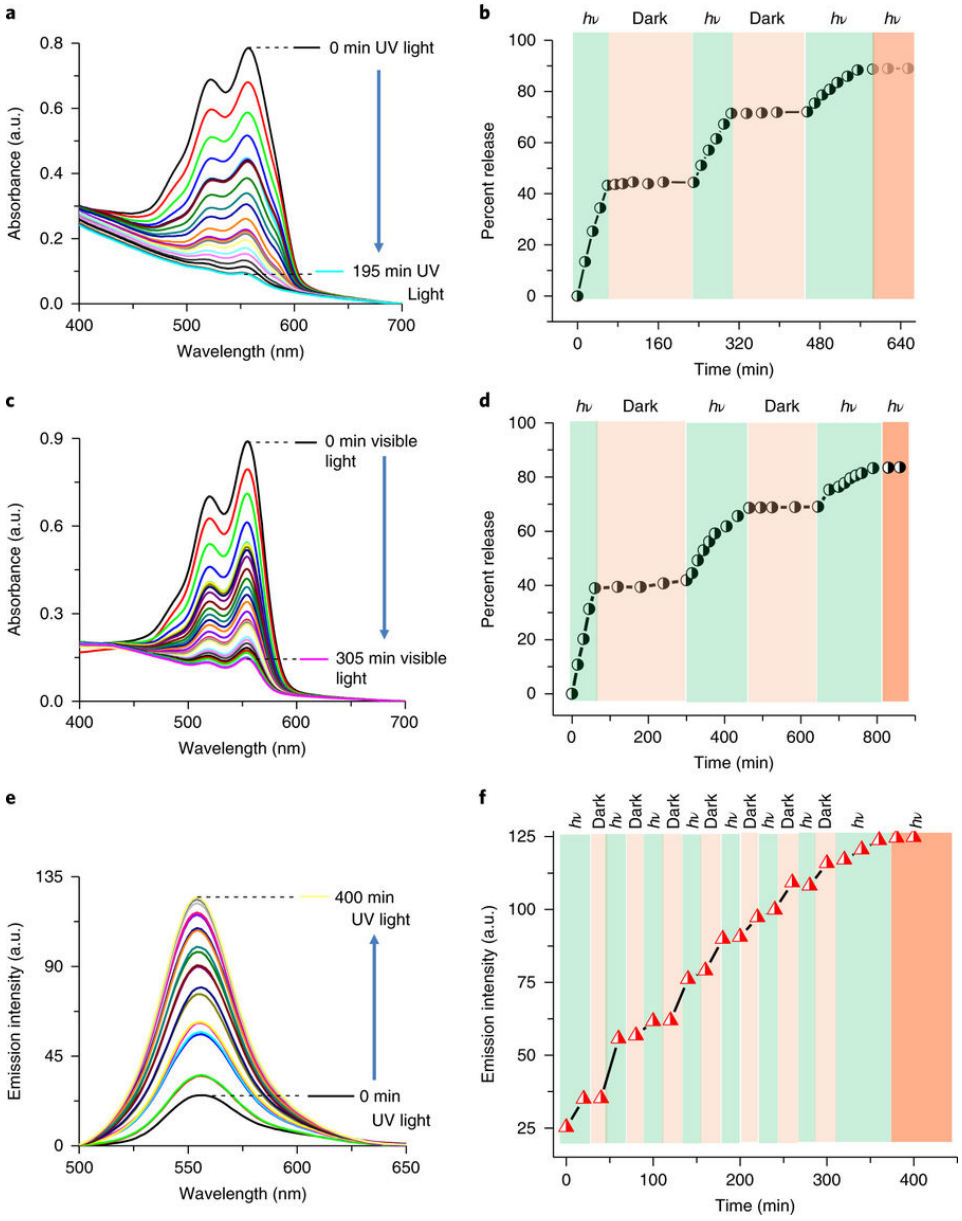

Figure 4.3: P2 vesicles demonstrating non-equilibrium behavior. Absorption spectrum indicating DiI release from **P2** vesicles during alternating cycles of **(a)** UV light and dark and **(c)**, visible light and dark. % release profile of DiI from **P2** vesicles in the alternating presence of **(b)** UV and dark, and **(d)**, visible light and dark. **e.** Increase in the emission intensity of R6G as a result of its release from **P2** vesicle, controlled by alternating cycles of UV and dark. **f.** Emission intensity profile of R6G during light and dark cycles. Orange portions of **b, d** and **f** indicate release saturation.

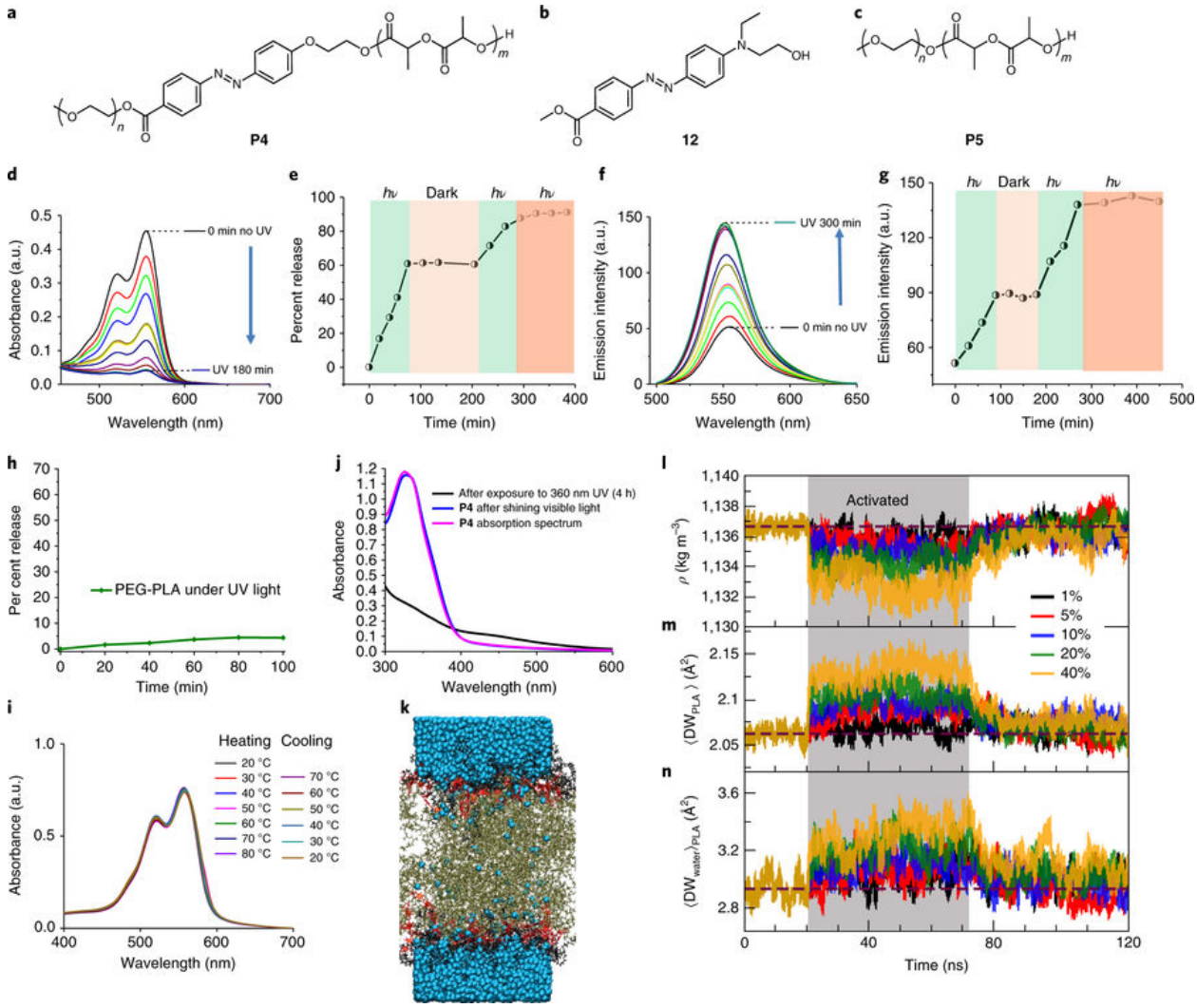

Figure 4.4: Mechanistic investigations to understand the P2 release mechanism Structure of **(a) P4 (b)** small molecule azobenzene (**12**) and **(c)** PEG-PLA **P5. d.** Control of DiI release from **P4** vesicles, **e.** Percent release of DiI from **P4** vesicles. **f.** R6G release from P4 vesicles, and **g.** Emission intensity of R6G from **P4** vesicles. (Orange portion indicates release saturation),under UV light. **h.** % release in PEG-PLA (**P5**) with small molecule (**12**) and DiI co-encapsulated under UV light. **i.** Absorption spectra of DiI encapsulated **P2** through a heating and cooling cycle **j.** Absorption spectrum showing the *trans-cis-trans* switchability of **P4**. **k.** AA-OPLS simulation model. Snapshot of the bilayer with 20 PLA monomers. There are some water molecules (blue) that enter into the PLA region (ochre) during equilibration. PEG is colored black and the azobenzene linkers are colored red. **l, m, n**. Indicates 20-PLA chain photoexcitation process. Gray box indicates simulated photo-excitation. **l** the density (ρ) of the system, **m** indicating the mobility of PLA and **n** indicating the mobility of water molecules in the PLA region during the excitation.

4.4 Supplementary Information

4.4.1 Materials and Methods

All the reagents were purchased from commercial sources and used as such without further purification. ^{1}H NMR spectra was recorded on a Bruker DPX-400 MHz NMR spectrometer and all the spectra were calibrated against trimethylsilyl (TMS) standard. Dynamic Light Scattering (DLS) measurements were carried out on a Malvern Nanozetasizer. TEM images were recorded on a JEOL-2000FX machine operating at an accelerating voltage of 100 kV. Fluorescence emission spectra were recorded on a JASCO (FP-6500) fluorimeter. UV-Vis spectra were recorded in a Carry 100 Scan spectrometer. Optical fluorescence microscopic images were captured on Olympus Fluorescence Microscope (BX51). Mass spectrometric data were acquired by an electron spray ionization (ESI) technique on a Q-tof-micro quadruple mass spectrometer (Micro mass). Atomic force microscopy (AFM) images were obtained on DI 3000 AFM Four machine.

4.4.2 Synthesis Details

Synthesis of Compound 2[56]: Poly (ethylene glycol) monomethyl ether ($M_n = 5000$) (5 g, 0.001 mol) and triethylamine (0.05 g, 0.005 mol) were taken in a 100 mL round bottomed flask and dissolved in 30 mL dry dichloromethane and the reaction mixture cooled to 0 °C. Then 4-toluenesulfonyl chloride (0.95 g, 0.005 mol) was added to the reaction mixture and it was allowed to go on for 2 h at 0°C followed by 12 h at room temperature (RT). The reaction was then terminated, the product precipitated from diethyl ether and recrystallized from ethanol (yield = 95 %).

^{1}H-NMR (400 MHz, DMSO-d6, TMS): δ (ppm) = 7.78 (d, 2H), 7.48 (d, 2H), 4.10 (t, 2H), 4.34 (t, 2H), 3.67 (t, 4H), 3.52-3.40 (m, 446H), 3.23 (s, 3H), 2.42 (s, 3H).

Synthesis of Compound 4[56]: Compound 2 (3 g, 0.6 mmol) and 3 (0.4 g, 2.9 mmol) were taken in a round bottomed flask and dissolved in 50 mL dry dimethylformamide along

with activated potassium carbonate (0.4 g, 2.9 mmol). The reaction mixture was placed in a preheated oil bath at 50 °C and stirred for 24 h. Then the reaction was stopped and poured into an excess of cold diethyl ether to precipitate the product. It was recrystallized in ethanol to get pure product in 72% yield.

^{1}H-NMR (400 MHz, DMSO-d6, TMS): δ (ppm) = 7.63 (d, 2H), 6.56 (d, 2H), 5.97 (s, 2H), 4.26 (t, 2H), 3.68 (t, 4H), 3.52-3.40 (m, 446H), 3.23 (s, 3H).

Synthesis of Compound P1: Aqueous solution (1 mL) of compound 4 (0.63 g, 0.13 mmol) was cooled to 0 °C temperature and 0.1 mL of concentrated hydrochloric acid (HCl) was added along with aqueous solution of sodium nitrite ($NaNO_2$) (45 mg in 0.5 mL water). Then cold DMF solution of compound 5 (0.145 g, 0.9 mmol) was added dropwise to the reaction mixture and allowed to stir at RT for 72 h under inert atmosphere. The reaction mixture was diluted with 20 mL chloroform and washed with water (3 x 30 mL) and brine (1 x 30 mL). The organic layer was collected and dried over anh. sodium sulfate (Na_2SO_4). The chloroform layer was then precipitated from diethyl ether to get red color solid product in quantitative yield.

^{1}H-NMR (400 MHz, DMSO-d6, TMS): δ (ppm) = 8.10 (d, 2H), 7.87 (d, 2H), 7.80 (d, 2H), 6.86 (d, 2H), 4.84 (t, 2H), 4.42 (t, 2H), 3.77-3.43 (m, 454H), 3.23 (s, 2H), 1.16 (t, 3H). GPC (DMF): M_n = 6000 g mol^{-1}, PDI = 1.10.

Synthesis of Polymer P2[99]: Lactide monomer (3,6-Dimethyl-1,4-dioxane-2,5-dione) was first recrystallized several times from ethyl acetate and dried thoroughly. Then 190 mg (1.3 mmol) of the monomer and the catalyst, tin (II) 2-ethylhexanoate ($Sn(Oct)_2$)(12 mg, 0.2 mmol), were taken in a Schlenk flask and dissolved in 0.6 mL of dry toluene. The macroinitiator P1 (70 mg, 0.013 mmol) was dissolved in dry toluene (0.5 mL) and added to the reaction mixture. The resulting reaction mixture was placed in a preheated oil bath and stirred at 120 °C temperature under argon atmosphere for 48 h. The reaction was stopped, cooled to room temperature and the product precipitated from cold diethyl ether. To remove the unreacted macroinitiator, it was dialyzed (MWCO 7000 Da) against water for 48 h while

water was changed every 6h. The resulting solution was lyophilized to get orange color solid polymer.

^{1}H NMR (400 MHz, $CDCl_3$, TMS): δ (ppm) = 5.21 (broad peak, 1H), 3.70 (PEG protons), 3.40 (s, 3H), 1.57 (broad peak, 2H). GPC (DMF): M_n = 18000 g mol^{-1}, PDI = 1.32.

Synthesis of compound 7: Compound 2 (700 mg, 0.67 mmol) and *p*-nitro phenol (94 mg, 0.67 mmol) were taken in a round bottomed flask along with activated potassium carbonate (94 mg, 0.67 mmol). All the reactants were dissolved in 50 mL dry DMF and the reaction mixture was placed in a preheated oil bath at 60 °C and stirred for 30 h. Then the reaction was stopped and poured into an excess of cold diethyl ether to precipitate the crude product as a yellow color solid. It was dialyzed (MWCO 3500 Da) against water for 24 h to remove unreacted nitro phenolate. The dialyzed solution was lyophilized to get pure product as off white color solid in 75% yield.

^{1}H NMR (400 MHz, $CDCl_3$, TMS): δ (ppm) = 8.25 (d, 2H), 7.01 (d, 2H), 4.30 (t, 2H), 3.90 (t, 2H), 3.8-3.5 (m, PEG protons), 3.41 (s, 3H).

Synthesis of compound 8: Compound 7 (500 mg, 0.09 mmol) was dissolved in 50 mL of ethanol in a reaction bottle. 150 mg of Pd/C was added slowly to the methanol solution of compound 7. The reaction bottle was then connected to a shaker hydrogenator apparatus under the pressure of 40 psi. After 24 h reaction was terminated, filtered through celite and the solvent was evaporated to get the pure product in quantitative yield.

^{1}H NMR (400 MHz, $CDCl_3$, TMS): δ (ppm) = 6.81 (d, 2H), 6.45 (d, 2H), 4.20 (t, 2H), 3.90 (t, 2H), 3.81-3.52 (m, PEG protons), 3.41 (s, 3H).

Synthesis of compound 9: Aqueous solution (1 mL) of compound 8 (400 mg, 0.05 mmol) was cooled to 0 °C and 0.1 mL of concentrated HCl was added to it along with an aqueous solution of $NaNO_2$ (45 mg in 0.5 mL water). In a separate vial, phenol (145 mg, 1.54 mmol) was dissolved in aqueous solution (1 mL) of sodium hydroxide (150 mg, 3.75 mmol) and added dropwise to the solution of compound 8. The resulting reaction mixture was stirred at room temperature for 15 h. The reaction was stopped and dialyzed (MWCO 3500 Da)

against water for 24h to remove unreacted excess phenolate. The dialyzed solution was lyophilized to get pure product as light yellow color solid in 90% yield.

^{1}H NMR (400 MHz, DMSO, TMS): δ (ppm) = 7.81 (d, 2H), 7.54 (d, 2H), 7.21 (d, 2H), 6.91 (d, 2H), 4.55 (d, 2H), 4.30 (t, 2H), 3.90 (t, 2H), 3.8-3.5 (m, PEG protons), 3.41 (s, 3H).

Synthesis of P3: Compound 9 (220 mg, 0.042 mmol) and 3-bromo 1-propanol (23 mg, 0.17 mmol) were taken in a round bottomed flask along with activated potassium carbonate (20 mg, 0.14 mmol) and catalytic amount of potassium iodide. All the reactants were dissolved in 10 mL dry DMF and the reaction mixture was placed in a preheated oil bath at 60 °C and stirred for 24 h. The reaction was stopped and dialyzed (MWCO 3500 Da) against water for 24 h to remove any unreacted 3-bromo 1-propanol. The dialyzed solution was lyophilized to get pure product as light yellow color solid in 85% yield.

^{1}H NMR (400 MHz, DMSO), TMS): δ (ppm) = 7.84 (d, 1H), 7.55 (d, 1H), 7.42 (d, 1H), 7.11 (d, 1H), 4.58 (2H, t), 4.14 (2H, t), 3.7-3.45 (PEG protons, and $-CH_2OH$ protons, m), 3.24 (3H, m), 2.1 (2H, m). GPC (DMF): M_n = 6000 g mol^{-1}, PDI = 1.10.

Synthesis Polymer P4[99]: Before the polymerization reaction was set up, lactide monomer was recrystalized from ethyl acetate. Then, lactide monomer (200 mg, 1.38 mmol) and catalyst tin (II) 2-ethylhexanoate ($Sn(Oct)_2$) (12 mg, 0.21 mmol) were taken in a Schlenk flask and dissolved in 0.5 mL dry toluene. The macronitiator P3 (60 mg, 0.011 mmol) was dissolved in dry toluene (0.5 mL) and added to the reaction mixture. The final reaction mixture was placed in a preheated oil bath and stirred at 120 °C temperature under argon atmosphere for 48 h. The reaction was stopped, cooled to RT and precipitated from cold diethyl ether. To remove unreacted macroinitiator, it was dialyzed (MWCO 7000 Da) against water for 48 h while water was changed every 6 h. The resulting solution was lyophilized to get orange color solid polymer.

^{1}H NMR (400 MHz, $CDCl_3$, TMS): δ (ppm) = 5.20 (broad peak, 1H), 3.71 (PEG protons), 3.41 (s, 3H), 1.55 (broad peak, 2H). GPC (DMF): M_n = 10000 g mol^{-1}, PDI = 1.30.

Synthesis of compound 12: Aqueous solution of compound 10 (Fig. 4.10) (1g, 6.6 mmol)

was cooled to 0 °C and 0.1 mL conc. HCl was added to it slowly with stirring, followed by an aqueous solution of $NaNO_2$ (1.3g, 19.8 mmol). A cold solution of compound 11 in DMF was added dropwise to the reaction mixture. The reaction was allowed to proceed for 6 h and then diluted with chloroform and washed with water and brine. The chloroform layer was concentrated and run through a purification silica gel column to get compound 12 in quantitative yield.

^{1}H NMR (400 MHz, $CDCl_3$, TMS): δ (ppm) = 8.2 (d, 2H), 8 (d, 2H), 7.8 (d, 2H), 7 (d, 2H), 4 (s, 3H), 3.8 (t, 2H), 3.5 (t, 2H), 3.3 (q, 2H), 0.9 (t, 3H)

Synthesis of compound P5: Lactide monomer was recrystallized from ethyl acetate and used for polymerization. Lactide monomer (1g, 6.9 mmol), poly(ethylene glycol)methyl ether (347mg, 0.069 m.mol, Mn:5 kDa) and catalyst tin (II) 2-ethylhexanoate ($Sn(Oct)_2$) (34 uL, 0.104 mmol) were taken in a Schlenk flask and dissolved in 1 mL dry toluene. The reaction mixture was placed in a preheated oil bath and stirred at 120 °C temperature under argon atmosphere for 48 h. The reaction was stopped, cooled to RT and precipitated from cold diethyl ether to obtain the polymer.

^{1}H NMR (400 MHz, $CDCl_3$, TMS): δ (ppm) = 5.20 (broad peak, 1H), 3.71 (PEG protons), 3.41 (s, 3H), 1.55 (broad peak, 2H). GPC (DMF): M_n = 16,000 g mol^{-1}, PDI = 1.30.

4.4.3 Characterization Studies

Dynamic Light Scattering (DLS) Study: For the DLS measurements, 0.5 mg of the polymer P2 was dissolved in 200 μl of acetone and, 1 mL water was added to it drop-wise for 10 minutes with constant stirring. The solution was kept open for 12 h to evaporate acetone. It was then filtered using hydrophilic membrane (pore size 0.450 μm) before the measurements were recorded.

Transmission Electron Microscope (TEM) Study: The same polymer solution that was prepared for the DLS study was used for TEM measurements. The sample was drop-casted on a carbon coated copper grid and air dried for 12 h. The average diameters of the

vesicles by TEM were found to be slightly lower than the hydrodynamic diameter by DLS measurements owing to shrinkage of the membrane in the dried state.

Atomic Force Microscopy (AFM) Study: One drop of the polymer solution (made for DLS) was placed on silicon wafer and dried in air for 12 h before images were taken. Considerably lower height of the vesicle compared to the width, and larger size compared to the TEM and DLS sizes can be attributed to the flattening of the hollow soft vesicular particle due to adsorption on the surface.[127]

Static Light Scattering (SLS): Static light scattering (SLS) measurements were performed on a ALV/SP-125 goniometer instrument. The same solution, prepared for DLS was also used for SLS study. Here, data was collected for different angles (30°, 40°, 50°, 60°, 70°, 80°, 90°, 100°, 110° and 120°) of incident light source, keeping the concentration of the solution same in all the measurements. The radius of gyration (R_g) was estimated from partial Zimm plot using the equation shown below.

$$I^{-1} = C(1 + R_g^2 q^2/3) \tag{4.1}$$

Where $I = I' \sin(\theta)$; I' = intensity of scattered light; θ is the angle of scattered light, C a constant; R_g is the radius of gyration; q is the magnitude of the scattering wave vector; $q = 4\pi n \sin(\theta/2)/\lambda_0$ (n is the refractive index of the liquid and λ_0 is the wavelength of light in vacuum). From the slope of this plot, R_g was estimated.

Self-Assembly Studies by NMR: 2 mg of polymer P2 was dissolved in 200 μl of acetone and 1 mL D_2O was added drop wise to the acetone solution. The solution was kept open for 12 h to evaporate acetone from the solution and the ^{1}H NMR was recorded.

Fluorescence Microscopy Studies: In a typical fluorescence microscopic experiment, 50 μl of dye encapsulated vesicle solution was placed on a cleaned glass slide, and a cover glass was placed on it. Images were captured on a fluorescence microscope (OLIMPUS BX-51) in 40 × magnification.

UV and Photoluminescence Studies: All the experiments were carried out at 25°C using a quartz cuvette of 0.2 cm path length.

DiI Encapsulation: To the vesicle solution of P2 polymer, 10 μl of DiI solution in acetone was added and stirred for 12 h at 25°C temperature. The vial was kept open to evaporate the acetone from the solution. The solution was then filtered through a hydrophilic membrane (pore size: 0.45 μm) before any experiment was performed.

Optical polarization microscopy (OPM) was also performed to confirm dye encapsulation. A drop of 0.1mg/mL polymer with DiI encapsulated, was placed between a glass slide and a cover slip. Although the resolution of optical microscopy does not allow us to determine the precise location of the dye molecules, the red emitting spherical particles under the fluorescence optical polarization microscope (OPM) confirmed its presence within the assembly (Fig. 4.2d).

The dye by itself is insoluble in water, therefore we cannot see any absorbance or emission corresponding to it (Fig. 4.2b and c, Red). However, when the dye is encapsulated in the hydrophobic pockets of the vesicle, one can observe the absorbance and emission. The dye release from the vesicle upon irradiation of light can be observed from the absorbance and emission spectrum. The intensity goes down as the dye is released from the vesicle, rendering it insoluble. The release % can be quantified from the absorbance spectrum using the following equation: $[(I_0 - I_t)/I_0] \cdot 100$ where I_0 is the initial intensity of absorbance and I_t is the absorbance intensity at any time t.

R6G Encapsulation: 1 mg of R6G was dissolved in 100 μl MeOH and the MeOH was evaporated to make a thin film of R6G. To this thin film, vesicle solution of P2 (1 mg/mL) was added with constant stirring. The solution was stirred for 2 h and the resulting mixture was dialysed against water for 3 days while the water was changed in every 6 h interval. This dye encapsulated solution was used for optical spectroscopic measurements.

Rhodamine 6G is a water soluble dye. After encapsulation of R6G, the polymer solution was extensively dialyzed against water to get rid of excess unencapsulated dye. Fluorescence of the dialyzed solution was then evaluated to confirm the presence of the guest molecules in the lumen. The emission intensity of the dye molecule at 555 nm within the assembly is much lower than the absorbance-matched solution of the free dye in the aqueous phase (Fig. 4.2f, g). This reduced emission is attributed to the encapsulation-induced increase in local concentration of the self-quenching R6G guest molecules. Upon irradiation, the R6G molecules upon release into the bulk, will experience much less self-quenching which can be observed with a recovery in the fluorescence intensity (Fig. 4.3e).

OPM images also confirm the presence of the dye molecules within the assembly interior (Fig. 4.2h)

Calculation of Dye Loading Efficiency and Loading Capacity : The dye loading efficiency (DLE) and dye loading capacity (DLC) were calculated by absorption spectroscopy using the following equations:

DLE (%) = [weight of dye in vesicles/weight of dye in feed]$\times$100%

DLC (%) = [weight of dye in vesicles/weight of dye loaded vesicles] $\times$ 100%

The dye loading capacity of the P2 vesicles were found to be 29% and 2%, and their dye loading efficiencies were 40% and 13% for DiI and R6G respectively. The guest encapsulation capacities of these assemblies were 29 wt% and 2 wt% for DiI and R6G, respectively. The large difference in this capacity is attributed to the fact that the bulk aqueous medium provides a competitive solvation environment for R6G, but not for the hydrophobic DiI molecule.

Light Responsive Dye Release Studies: Dye encapsulated vesicle solution was taken in a quartz cuvette and kept under UV light (360 nm), visible light (450 nm) or the appropriate aforementioned light source, separately. Release of the dye molecules were monitored by absorption and fluorescence spectroscopy. A small stir plate with temperature control was used inside the UV chamber, for the Arrhenius fit studies. For each set of measurements, an

oil bath was preheated inside the UV chamber, inside which the sample was clamped, with constant stirring for each measurement.

Thermal studies: Thermogravimetric analysis (TGA) was performed using a TGA Q500 system from TA Instruments Inc. under a N_2 atmosphere from 0-500 °C at a heating rate of 5 °C /min.

Differential Scanning Calorimetry (DSC) was performed using a DSC Q200 RCS system from TA Instruments Inc. with refrigerated Cooling System. The sample was heated with constant ramp rate of 10 °C/min between -30 °C and 90 °C.

From the DSC data, we can see that during the first heating cycle, there is a sharp melting endotherm at 46.3°C. The PLA T_g transition overlaps in this region, thus we cannot see it in the DSC.

4.4.4 Molecular Dynamics Simulations

Molecular dynamics simulation studies: All-atom simulations of the PEG-AZO-PLA bilayer were performed using the all-atom optimized potential for liquid simulations (AA-OPLS) force field with TIP4P water model [69, 72]. Updates to the OPLS force field parameters for PLA were applied to the PLA polymer block[93]. Each polymer consisted of 20 PEG monomers, and three different cases were used for the length of the PLA end: 20, 30, and 50 PLA residues (as defined in the main text). Bilayers were constructed in vacuum with either 6×6 polymers, for the 20 and 30-unit cases, or 8×8 polymers, for the 50-unit case, in each leaflet with the PLA blocks of the separate leaflets in close proximity, where the normal of the leaflet is in the z direction. During construction, the chirality of the stereo centre within each PLA monomer was randomly chosen to ensure that the polymers were atactic. The energy of the entire system was then minimized using the conjugate-gradient method. A short isothermal isobaric run (3-5 ns) was performed at 450 K with just the polymers. During this run, a moving restraint on the center-of-mass distance between the two PLA leaflets was used to draw them together prior to solvation, and also to relax the x and y

dimensions. The bilayer was then solvated with enough water molecules such that a layer of only water, approximately two nanometers thick, separated the PEG leaflets (Figure 4.4j). After solvation, all water molecules in the PLA region were removed. The energy of the system was minimized, after which a 5 ns long isothermal-isobaric run at 450 K was carried out to relax the system.

PLA has an experimental T_g in the range of 330 K to 345 K. Due to this high T_g (discussed further below), an annealing run was performed from 450 K to 298 K. For equilibration purposes, two separate thermostats were used during these simulations, one that acted on the water atoms and another for the polymer atoms. The water atoms were kept at 298 K, while the temperature of the polymer atoms was elevated to increase the mobility of the PLA region and allow the structure to better relax on simulation timescales. The polymer atoms were initialized to 450 K and allowed to relax to this elevated temperature for 10 ns. Following this slight temperature equilibration, these atoms were cooled from 450 K down to 298 K at a rate of 10 K/ns and held at 298 K for 5 ns. By the end of this equilibration procedure, the x and y dimensions were found to be approximately 6.5 nm, and the z dimension was found to be around 13 nm for the 20 PLA-unit chains. An iterative procedure was used to simulate photo-excitation and isomerization. In this procedure, the stochastic nature of photo-excitation was not enforced, but rather we concentrated on the structural change that occurs during successful isomerization events. Photoisomerization was induced using moving harmonic restraints, $k_{\text{harmonic}} = 1000$ kJ/mol, on the C-N-N-C dihedral angle within the azobenzene group. Each iteration consisted of the following steps:

1. Random selection of a predetermined proportion of azobenzene groups
2. Using the pulling restraint, the selected torsion was moved from a trans-conformation to a cis-conformation over a period of 5 ps
3. A restraint was applied to the cis-conformation for 500 ps
4. The pulling restraint was applied to move the torsion back to the trans-conformation

in 5 ps

This procedure was repeated throughout the simulation when the light perturbation was enacted. In the absence of light excitation, no external restraint was applied to the dihedral to keep it in the trans-conformation. The time period of 250 ps and 1000 ps was also tested for step 3 of the isomerization procedure (Figure 4.20). The thermal relaxation time back to the trans state for azobenzene depends upon the local environment and the chemistry, and measurements range from pico-seconds to microseconds. Our simulations are restricted to timescales on the order of pico-seconds to nano-seconds. With these considerations in mind, and given that the 3 time intervals examined exhibit comparable results, the time interval of 500 ps was selected. The reference temperature during photo-excitation production runs was held at 298 K. During all production runs, temperature coupling was achieved using velocity rescaling with a stochastic term[16]. A semi-isotropic pressure coupling was used for all runs, where the x and y dimensions were coupled together separate from the z dimension, as is common for constant pressure simulations of bilayers. The equilibration runs were performed using mainly the Berendsen barostat, which can handle large fluctuations more readily, and production runs were performed with the more thermodynamically consistent Parrinello-Rahman barostat [13, 109]. Coulombic forces were calculated using the particle mesh Ewald method.[41] All simulations were performed with a time step of 2 fs and periodic boundaries were applied in all dimensions. Molecular simulations were carried out using the GROMACS 5.1.1 simulation package with the PLUMED 2.2 plug-in for the moving restraints.[59, 112, 107, 1, 147]

Simulation studies on the longer PLA chain P2:

The response to isomerization for PLA chains of different molecular weights was also considered. The results are shown in Figure 4.19. Specifically, the PLA block was increased to 30 residues, which is about a third of the experimental length, and subjected to the same simulation procedure that was implemented for the 20-residue case. One can appreciate in the figure that both systems exhibit a very similar response when subjected to a 20%

activation rate (Fig. 4.19a,b). The length of the PLA chains was further increased to 50 residues, or little more than half the experimental length. In that case the system size was increased from 6×6 polymers in each leaflet to 8×8 in order to accommodate the longer molecules, thereby resulting in simulations with more than 300,000 atoms. Given these large sizes, and the higher simulation costs, the isomerization period was reduced from 50ns to 10ns (Fig. 4.19c). The equilibration and preparation of the 50-residue case led to membranes with slightly higher density around the azobenzene groups, which required the transition time for isomerization to increase from 5 ps to 30 ps and that a smaller harmonic constant be used, namely k_{harmonic}=200 kJ/mol. The enhanced-dynamics profile for the 50-residue case displays the same behaviour as observed for the 20 and 30-residue case, even in the presence of these changes (Fig. 4.19). Moreover, the enhanced dynamics are more pronounced than in the shorter-chain systems.

4.4.5 Controlling Interfacial Nylon Formation

A control reaction of just sebacoyl chloride in hexane (concentration of 0.0010mg/mL), and hexamethylene diamine in water (concentration of 0.0014mg/mL), were gently mixed (by pouring the hexane solution gently down the sides of the vial containing the water layer). Instantaneously, long strands of nylon could be picked from the interface using a tweezer. 0.01 mg of hexamethylene diamine was encapsulated in 0.1mg/mL polymer solution, and the resultant solution was extensively dialyzed against water for two days, changing water every 8 hours. After encapsulation, the sebacoyl chloride in hexane (coloured with Nile Red dye for clear video) was added very slowly along the sides of the vial. No nylon strands could found at the interface. The vial was then kept in the UV chamber for 45 minutes to ensure complete release of the encapsulated hexamethylene diamine. After irradiation, however, there were few strands of nylon that could be picked from the interface of the two solvents (did not have to stir or vortex).

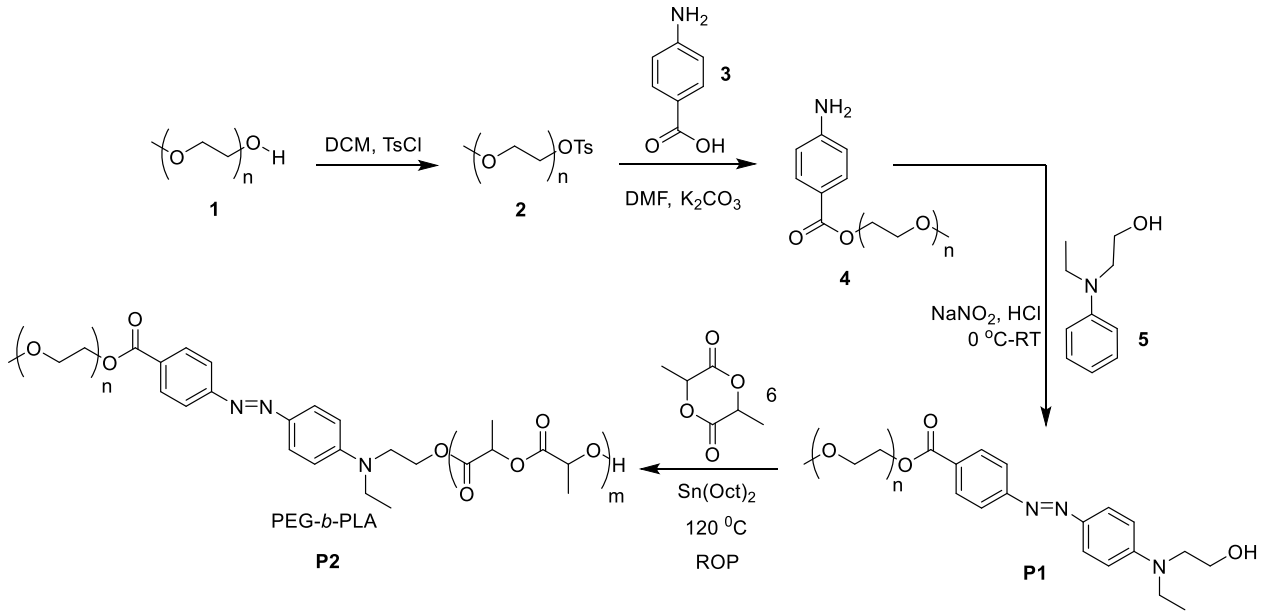

Figure 4.5: Synthetic route for the polymer P2.

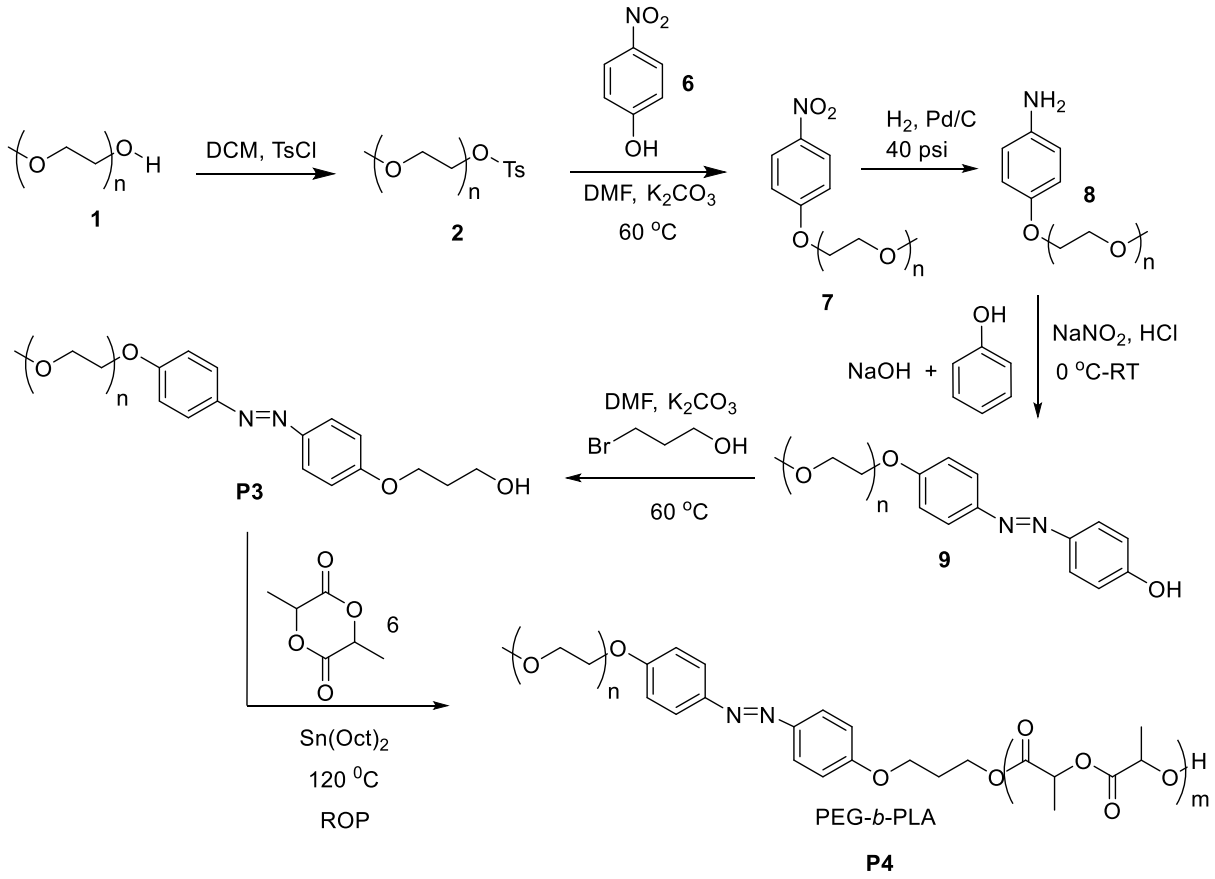

Figure 4.6: Synthetic route for the control polymer P4.

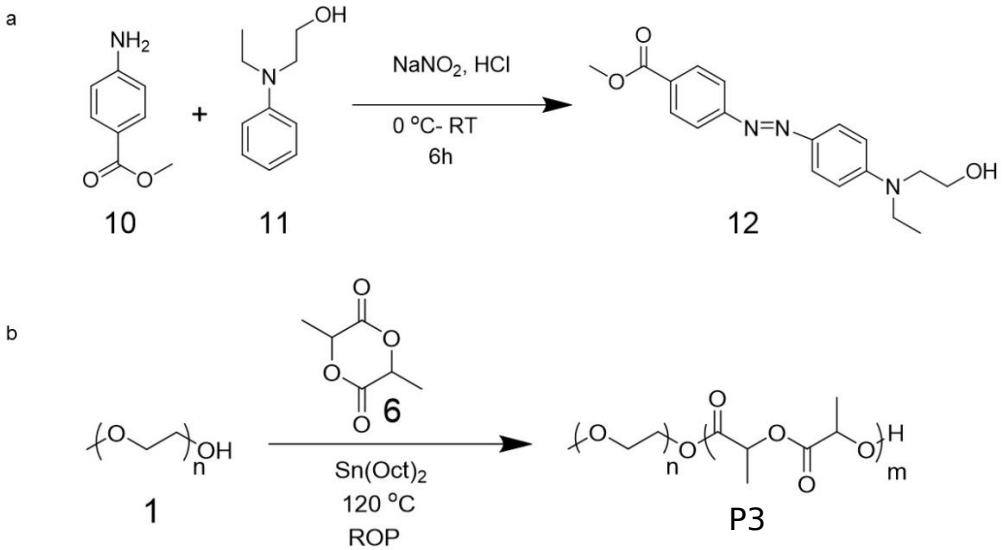

Figure 4.7: **a.** Synthesis of the small molecule DA azobenzene 12. **b.** Synthesis of the PEG-PLA block copolymer P5.

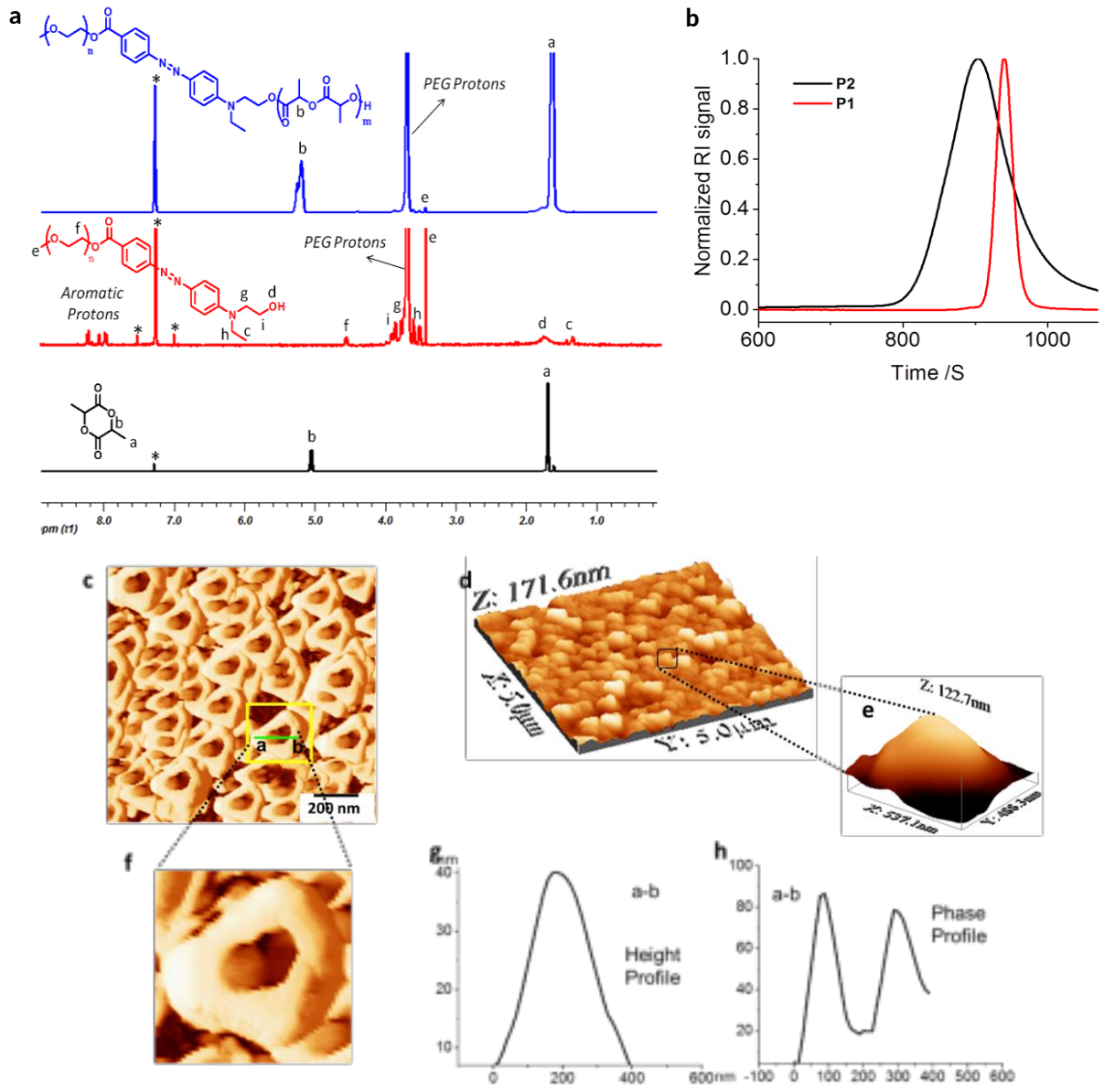

Figure 4.8: **a.** ^{1}H-NMR spectra of monomer, macro-initiator and polymer P2. Black, red and blue spectra correspond to monomer, macro-initiator and polymer P2 respectively. * indicates solvent peak. **b.** GPC chromatogram of macroinitiator P1 and polymer P2. Red and black spectra correspond to macro-initiator and polymer respectively. Solvent = DMF, Temperature = 25 °C, Molecular weight and PDI were calculated with respect to PMMA standards. **c** and **d.** AFM height and phase images of P2 vesicle. **e** and **f**. Zoomed version of one vesicle. **g**, AFM height profile. **h**. AFM phase profile.

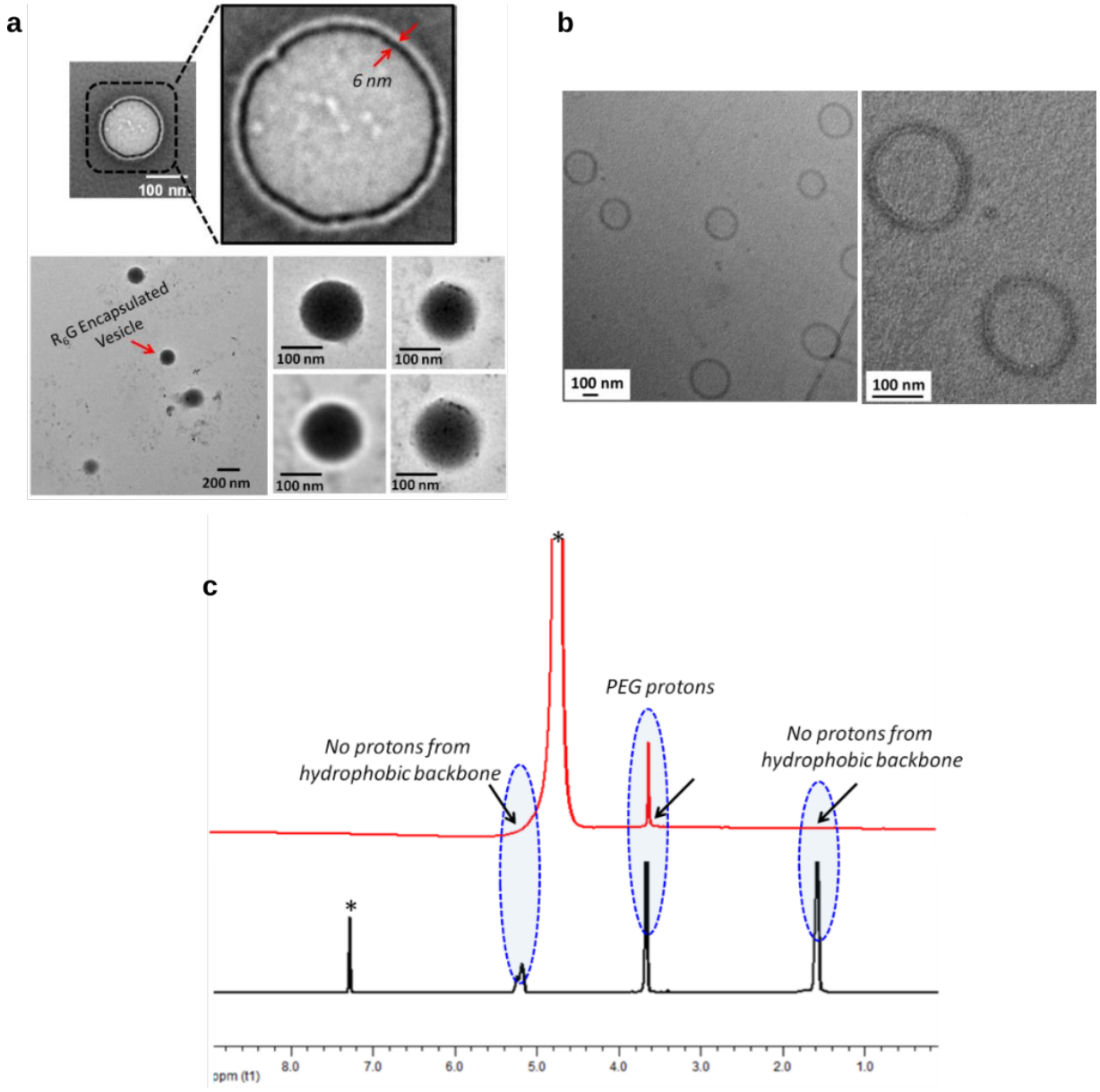

Figure 4.9: **a.** Empty P2 vesicles and R6G loaded vesicle. **Top**. Zoomed version of TEM image of a vesicle (negatively stained with Uranyl Acetate). **Bottom**. TEM image of R6G loaded vesicle. **b**. TEM images of P2 vesicles without negative staining. **c**. ^{1} H-NMR stack plot of non- aggregated (Black) and aggregated P2 polymer (Red). * indicates solvent peak.

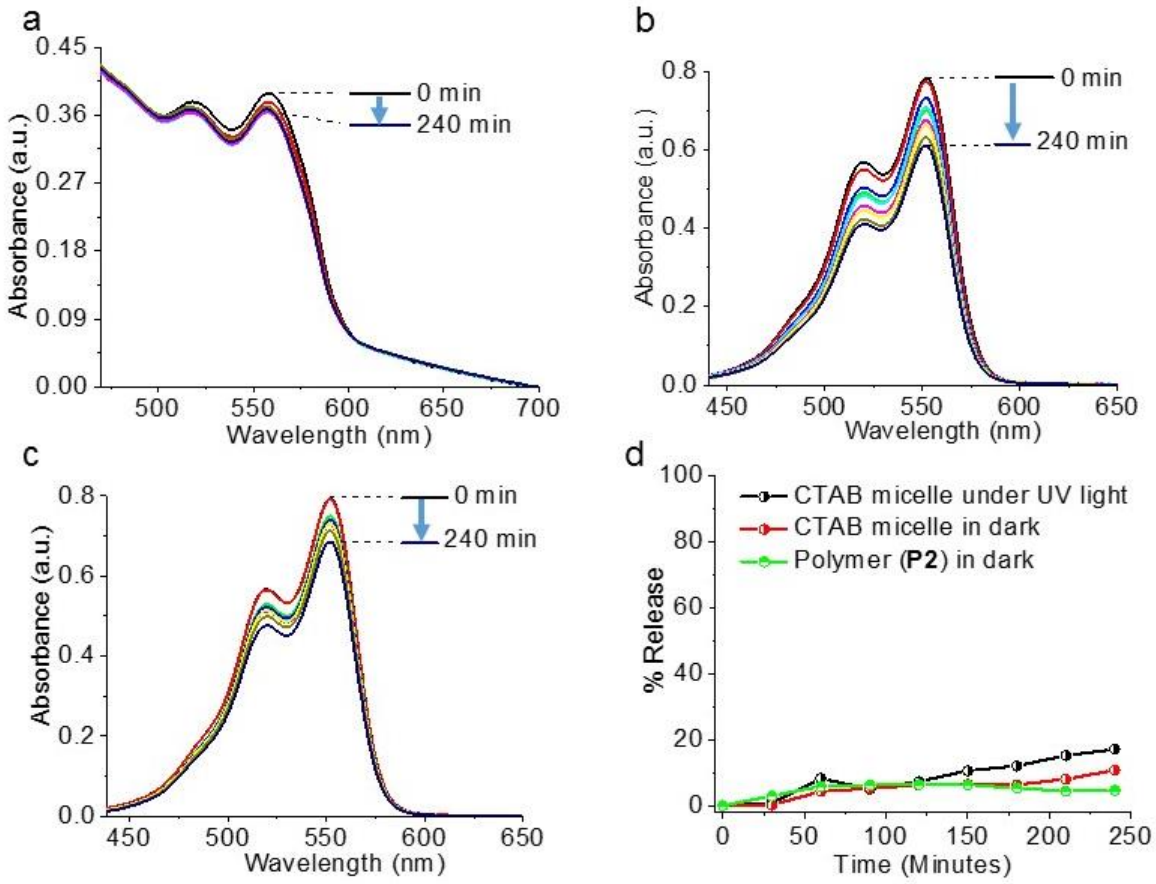

Figure 4.10: **a.** Release of DiI molecules from **P2** vesicle in dark. **b**. Release of DiI from CTAB micelle in presence of UV light and in **c.**, dark. **d.** % Release of DiI from P2 vesicle in dark and from CTAB micelles in presence of UV light and dark as well.

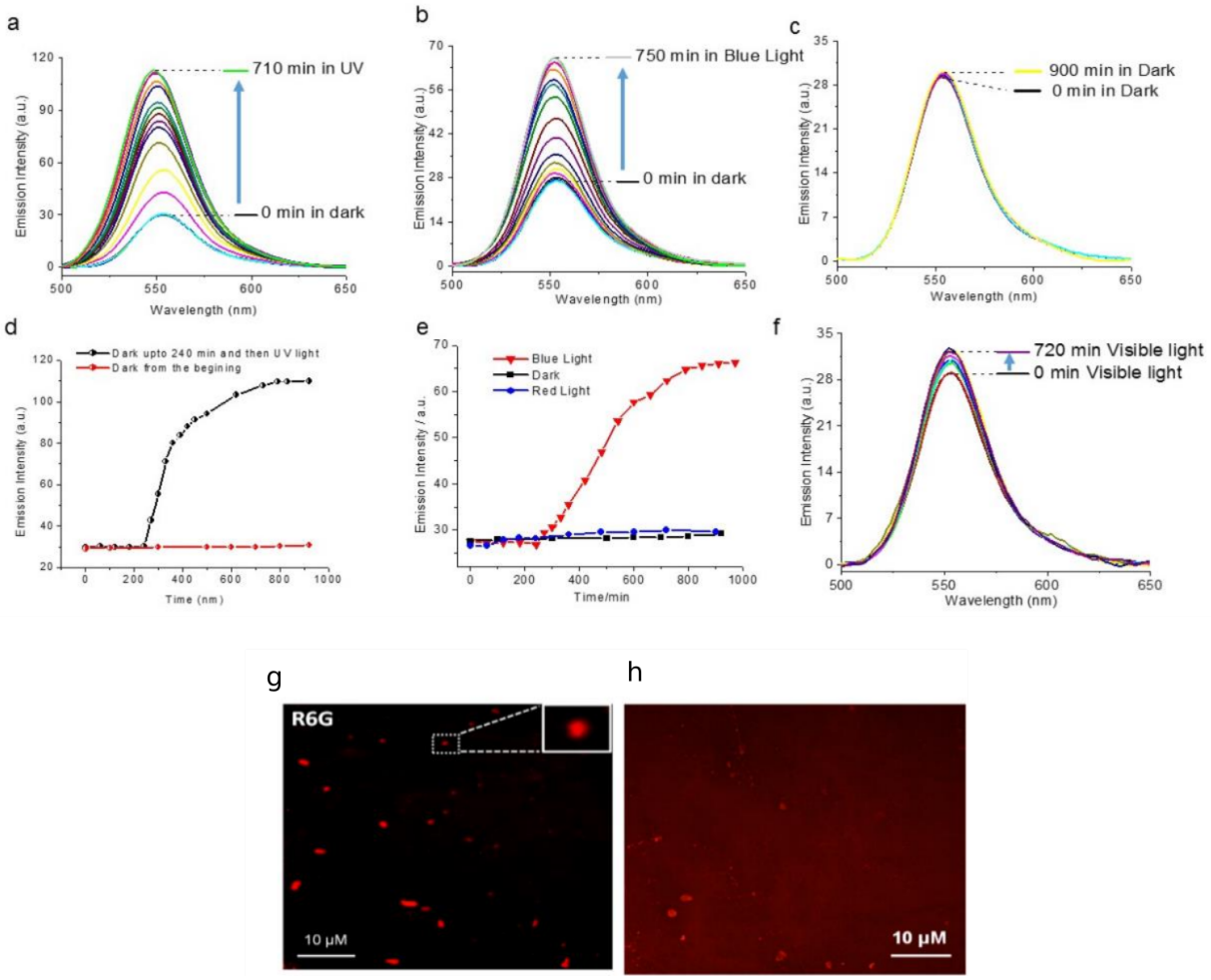

Figure 4.11: R6G release experiments in presence of UV/Visible light. **a.** Release of R6G in presence of UV light. **b.** R6G release in presence of a visible light (blue and wavelength = 450 nm). **c.** Control experiment in dark. **d** and **e.**, Change of emission intensity with time in presence of UV/Vis light. **f.** Control experiment using visible light (red) of 650 nm wavelength where photoisomerization does not happen. **Optical polarization microscopic (OPM) images. g.** Image of R6G encapsulated P2 vesicle. Red particle indicates R6G loaded P2 vesicle. **h.** Image after the UV irradiation of the R6G loaded vesicle. Red background indicates release of the R6G in the bulk water.

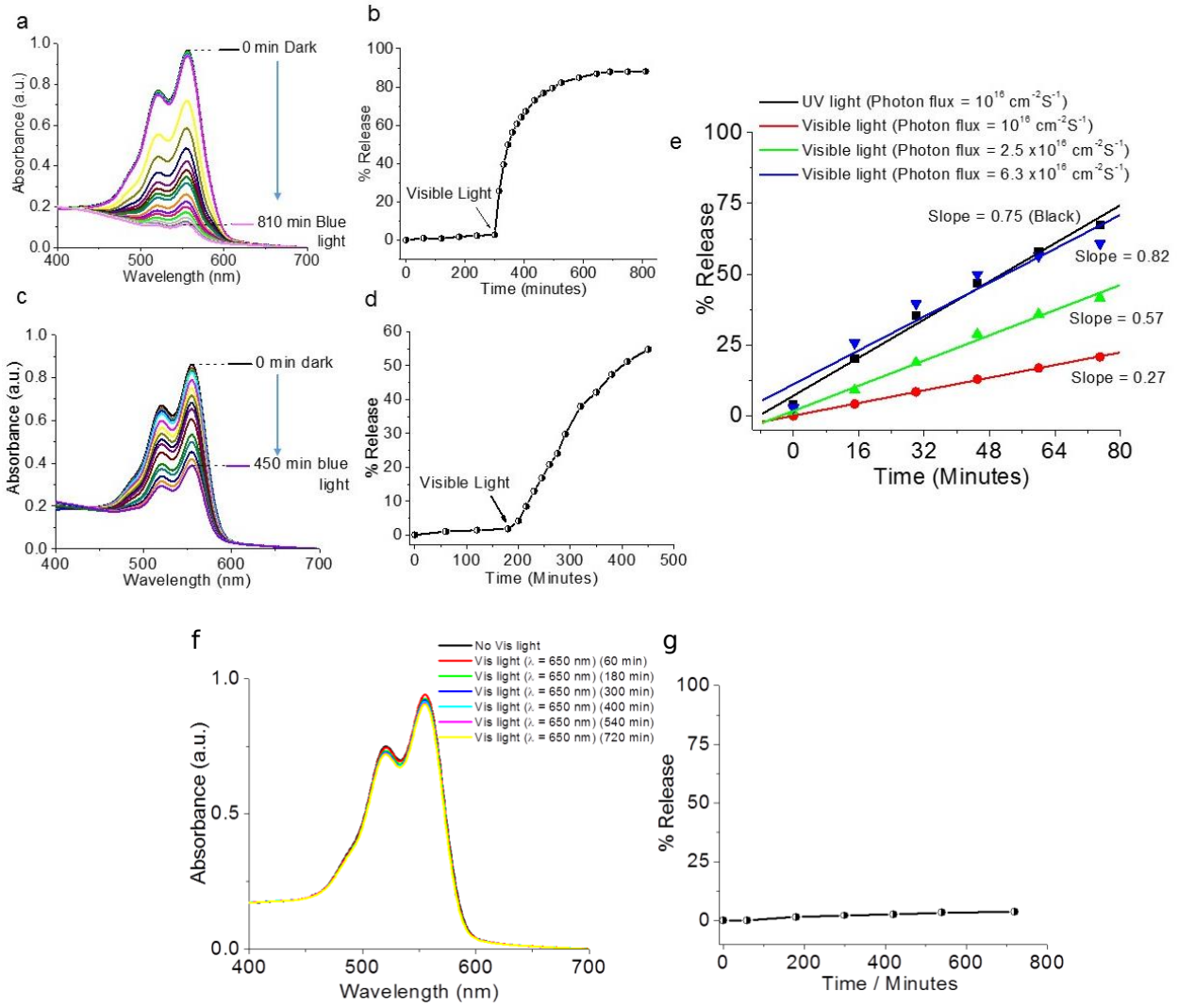

Figure 4.12: DiI release from P2 by varying number of photons from visible light. **a.** and **c.** Change of absorption intensity of DiI in presence of visible light (450 nm, **a**, photon flux = 6.3×10^{16} $cm^{-2}s^{-1}$ and **c**, photon flux = 2.5×10^{16} cm^{-2} s^{-1}). **b** and **d.** % release of DiI in presence of visible light (**b**, photon flux = 6.3×10^{16} $cm^{-2}s^{-1}$ and **d**, photon flux = 2.5×10^{16} cm^{-2} s^{-1}). **e**, Determination of release rate by varying the number of photons from visible light. Rate of release increases with the increase of number of photons. **Release in presence of a visible light of 650 nm wavelength**. **f.** Release of DiI from P2 vesicle in presence of 650 nm wavelength light. **g.** Plot of % release with time.

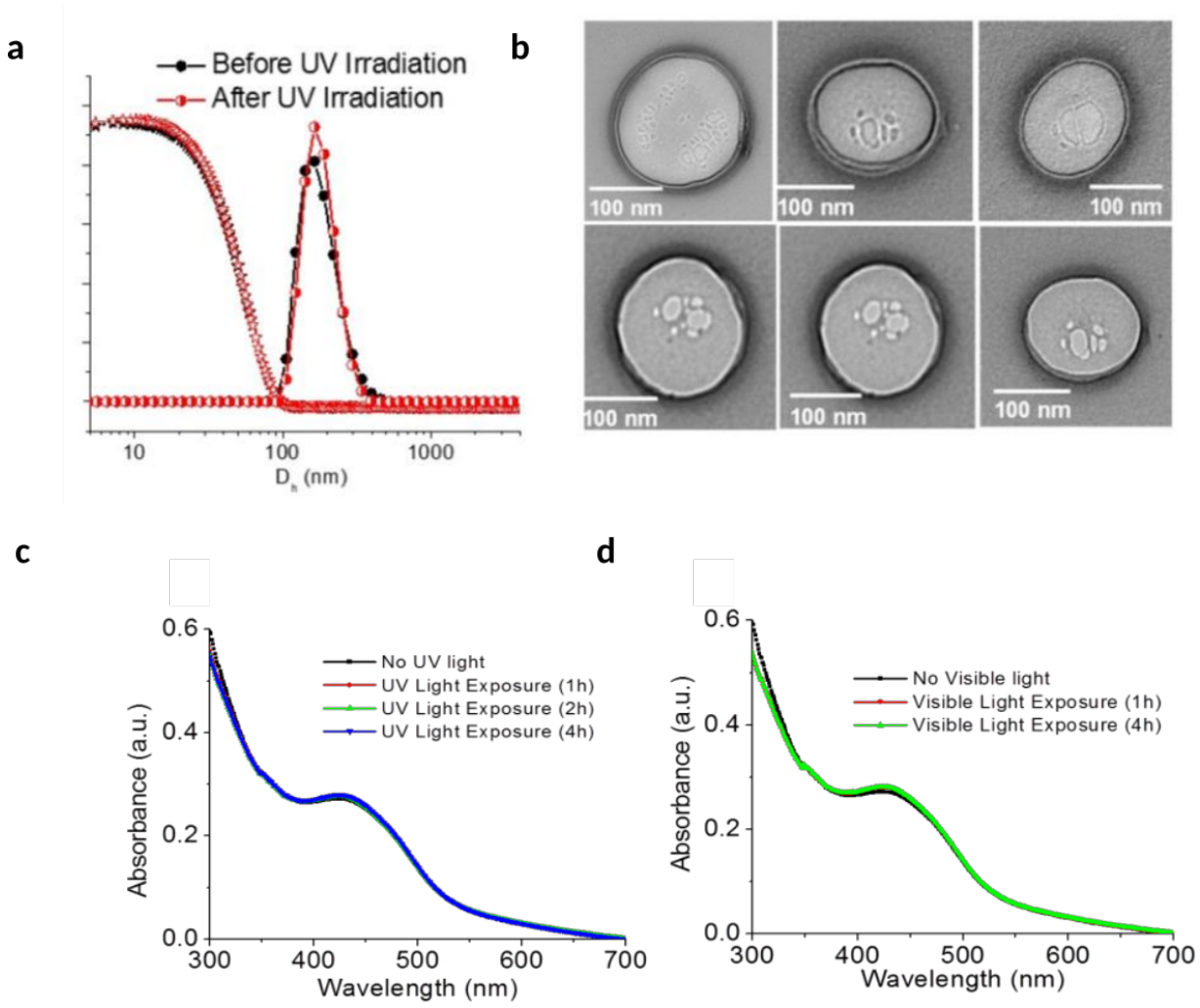

Figure 4.13: Size and morphology of P2 vesicle after 6h exposure to UV light. **a.** Comparison of DLS profile of P2 vesicle before and after the UV light exposure with the corresponding correlation functions on the left. **b.** TEM image (negatively stained with Uranyl Acetate) of P2 vesicle after treated with UV light. **Photoisomerization in presence of UV/Visible light. c.** Time dependent absorption spectra of P2 vesicle solution in presence of UV and **d.** visible light respectively.

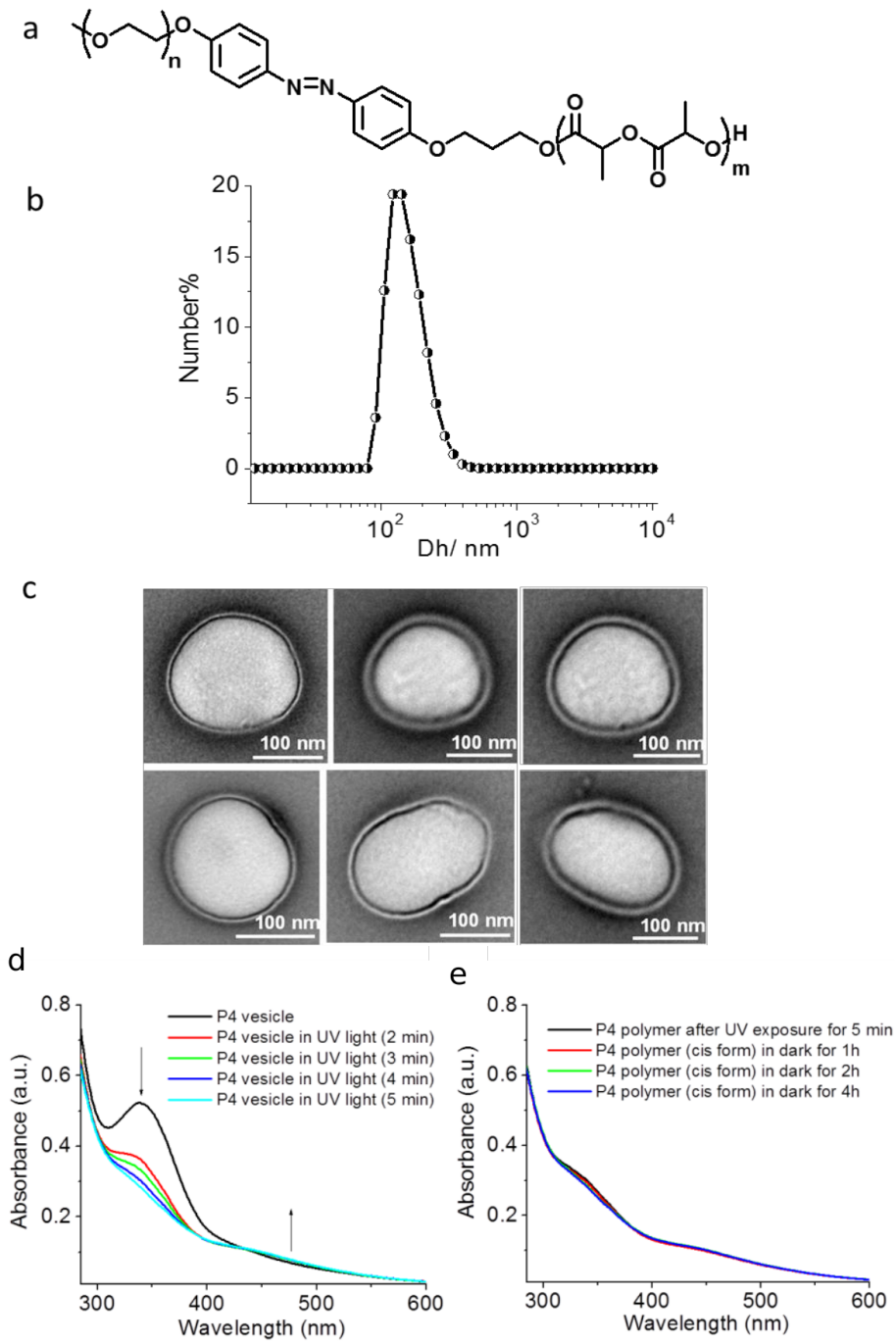

Figure 4.14: Chemical structure, size and morphology of control polymer P4. **a**, Structural representation of control polymer P4. **b**, DLS profile of the self-assembled P4 polymer. **c**, TEM images (negatively stained with Uranyl Acetate) of self-assembled P4 polymer. **Photoisomerization of P4 polymer in presence of UV light**. **d**, Under UV light *trans* isomer converts to *cis* isomer within 5 minutes. **e**, Change of absorption spectra of *cis* isomer in dark, over 4h.

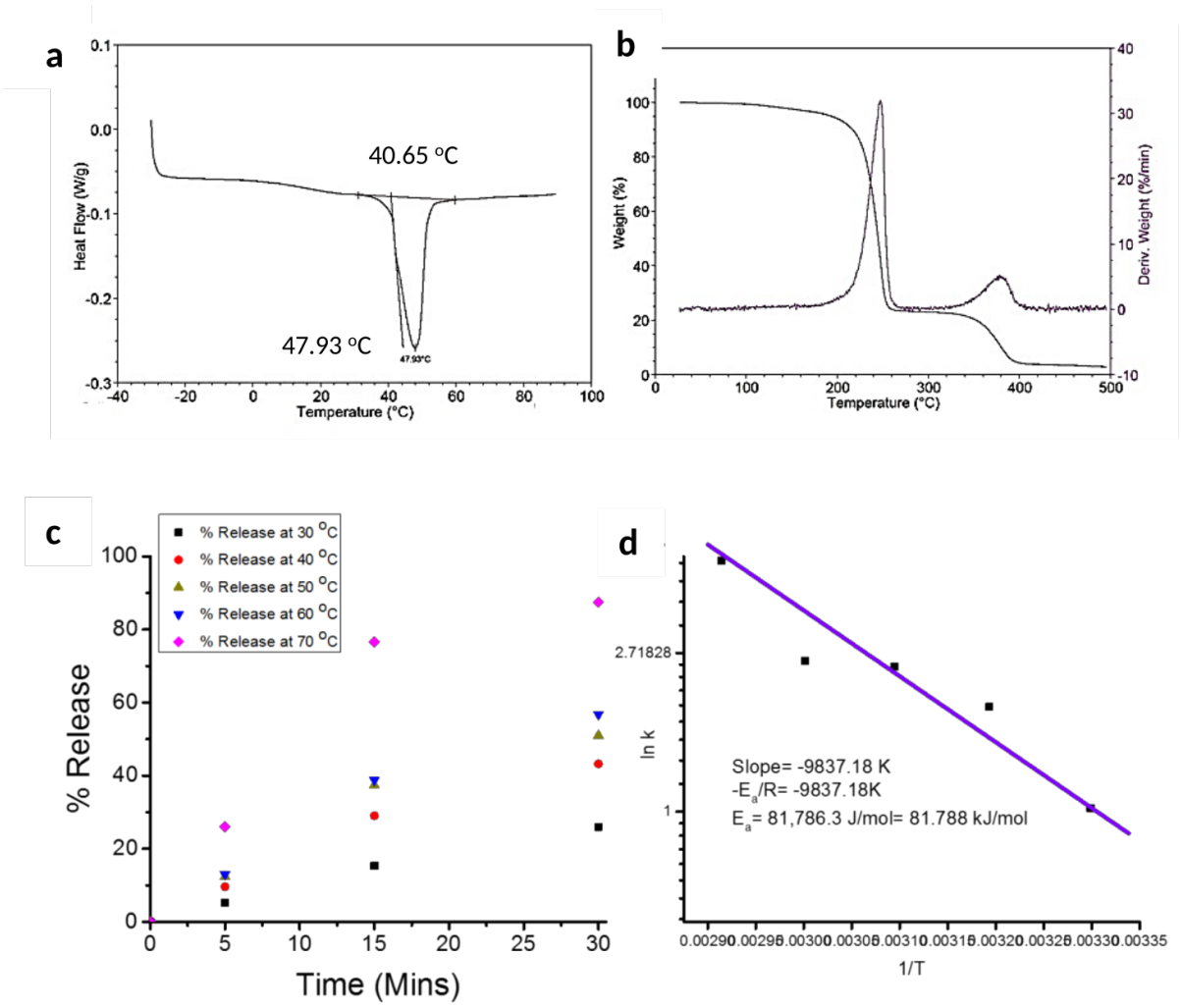

Figure 4.15: Thermal behavior of P2. **a**, DSC plot showing a melt endotherm at 47°C. **b**, TGA plot of P2 showing the % weight loss of PLA from 210°C and PEG % weight loss from 350°C. **Testing Arrhenius behavior of P2**. **c**, % release of DiI from P2 equilibrated at different temperatures, under UV stimulus. **d**, ln k vs 1/T displaying a linear Arrhenius fit.

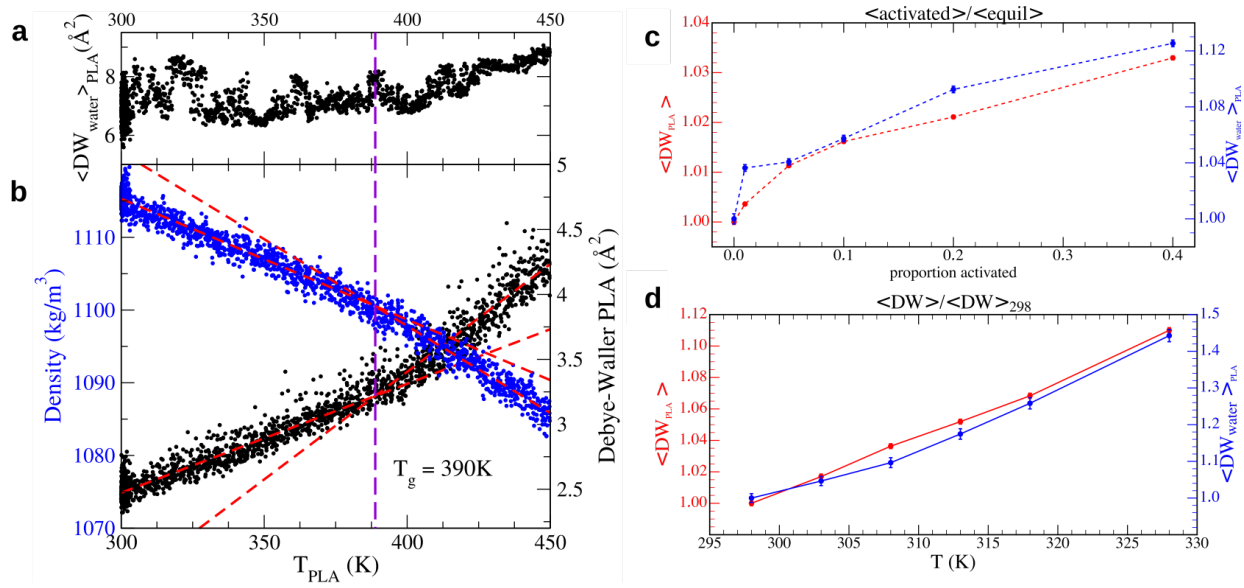

Figure 4.16: Cooling runs of the PLA block for 20 PLA unit chains. **a**, The average Debye-Waller factor for water atoms located within the PLA region as a function of temperature. **b**, Extrapolations (dashed red lines) of the liquid-cooled lines and glassy state lines for the density of the system (blue) and the Debye-Waller factor (black) as a function of temperature were used to calculate the simulated T_g for PLA. **20 PLA unit photo-excitation response**. **c**, The proportion increase in the DW factor for the PLA (red) and the water contained inside it (blue) as a function of proportion activated. **d**, The proportion increase in the average Debye-Waller factor when the polymer molecules are subjected to a heat shock at different temperatures relative to the averaged DW factor at 298 K.

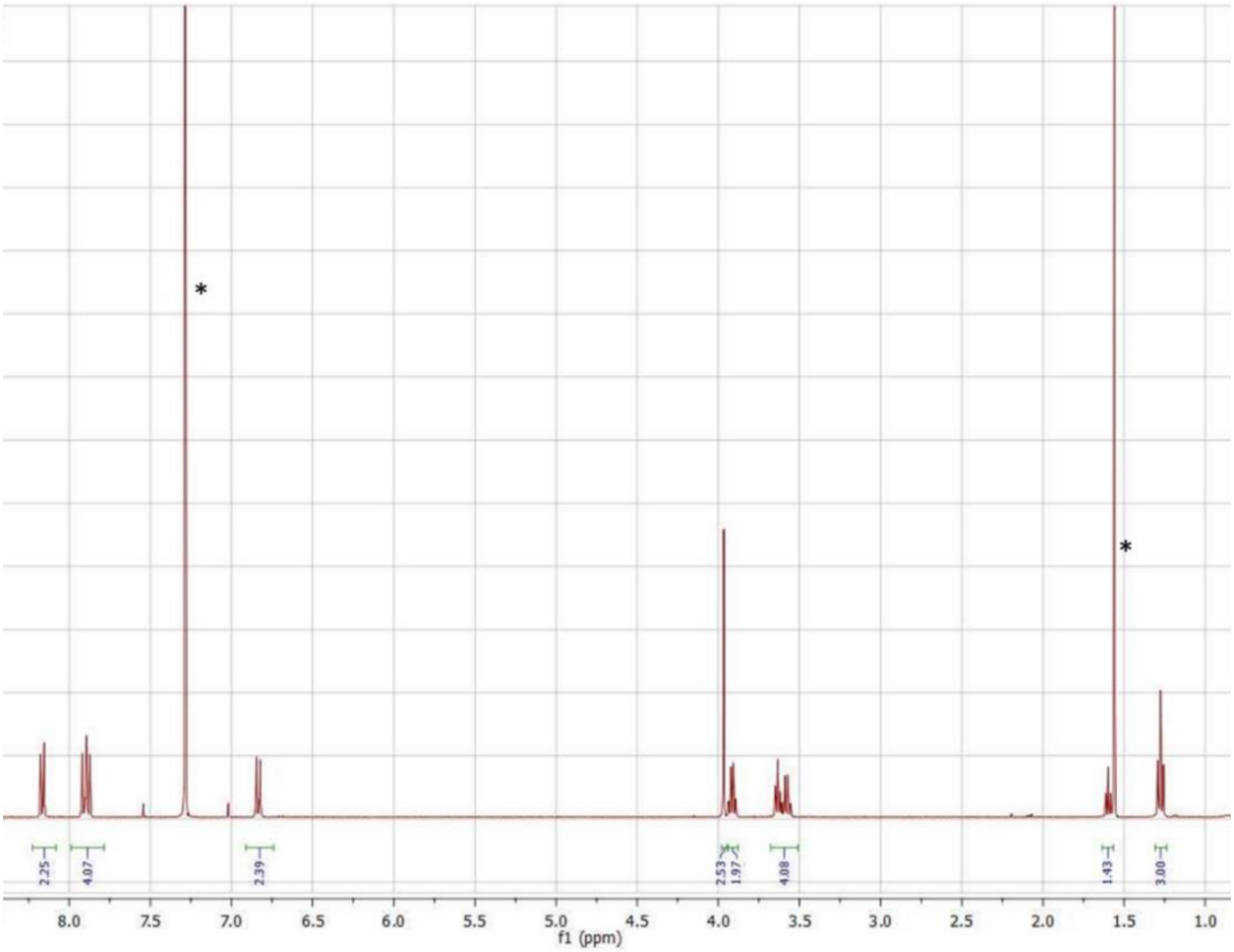

Figure 4.17: Proton NMR of compound 12. The * indicates solvent peaks.

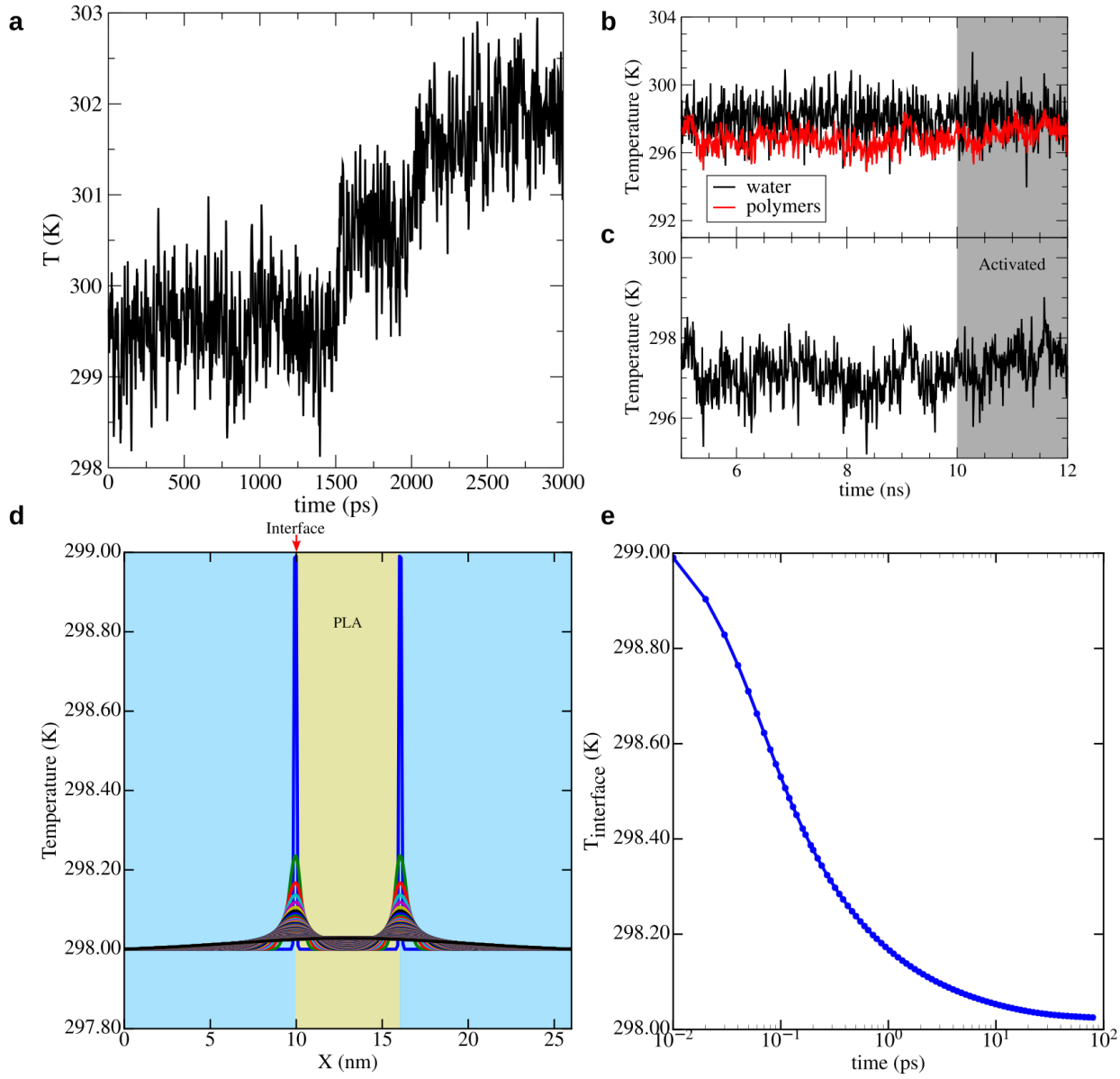

Figure 4.18: Local heating in simulations. **a**,Temperature of the system during one isomerization iteration where 20% of the azobenzene groups are isomerized when there is no thermostat algorithm applied, i.e. NVE simulation. **b**, Temperature of the water (black) and polymer (red) atoms where only the water atoms are coupled to a thermostat set at 298 K and the polymer atoms are NVE. Panel **c** is the temperature for the entire system and the gray box indicates the isomerization events are occurring. **One dimensional heat equation.** The 1D heat equation was solved numerically using the Crank- Nicolson method with $\Delta x = 0.1$ nm, $\Delta t = 0.001$ ps and Dirichlet boundary conditions. **d**, The state of the system every 0.5ps. The blue region used the thermal diffusivity of water (0.143 nm^2/ps) and the yellow/PLA region used the diffusivity of PLA estimated from 55 Fig. 7 (0.95 nm^2/ps). **e**, The temperature at the interface marked on (**d**) as a function of time.

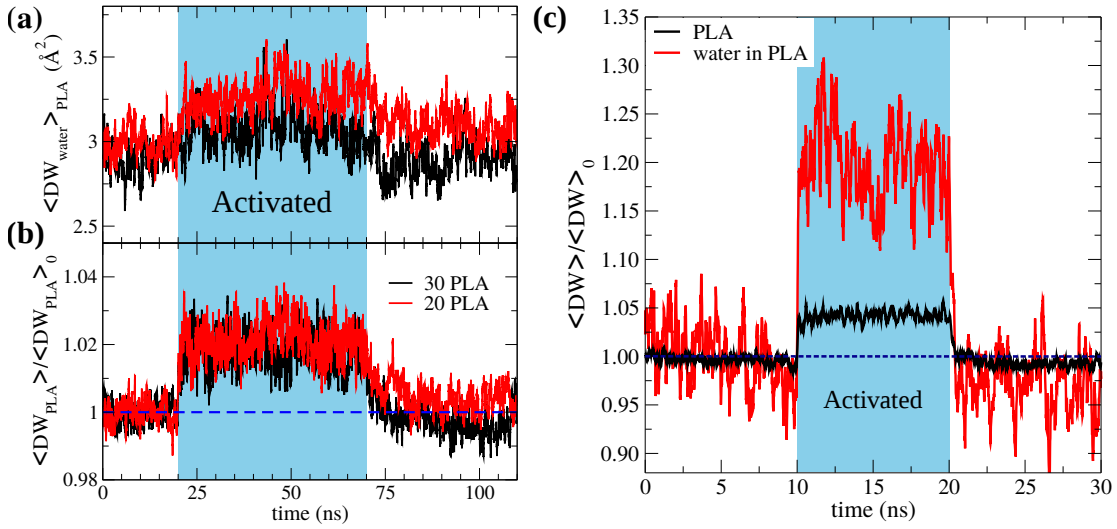

Figure 4.19: System Size Comparison. **(a)**, The average Debye-Waller (DW) factor of the water molecules within the PLA region and **(b)** the PLA molecules calculated as a function of time for the 30- lactide case (black) and the 20-lactide case (red). The DW factors are normalized by the value prior to isomerization. **(c)** The DW factors for the PLA (black) and the water contained within (red) for the system with 50 PLA residues per polymer chain. The blue region serves to highlight the period of simulated photoisomerization, where 20% of azobenzenes are being excited.

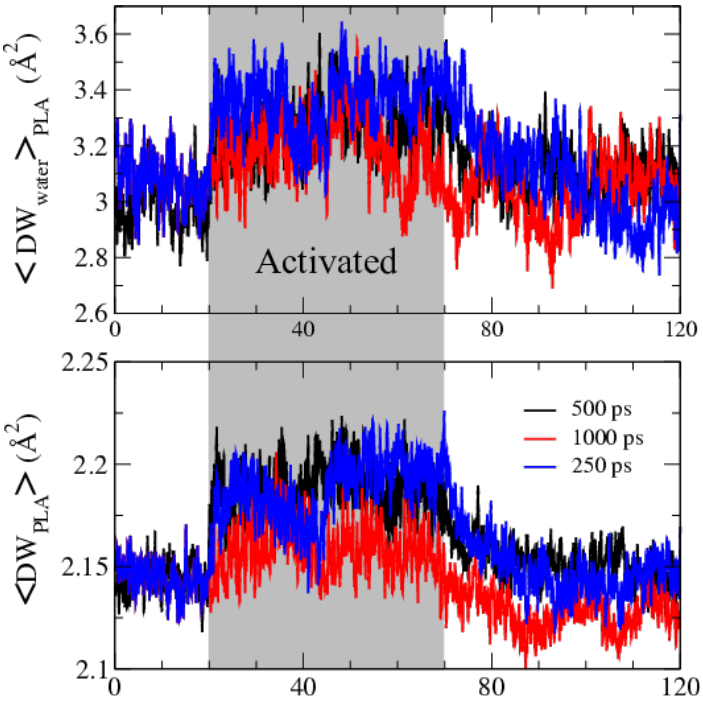

Figure 4.20: Time Interval Comparison. **Top**. The Debye-Waller factor of the encapsulated water and (**Bottom**) PLA molecules as a function of time for *cis* times 500 ps (black), 1000 ps (red), and 250 ps (blue). The time during simulated photoisomerization is highlighted by the grey block.

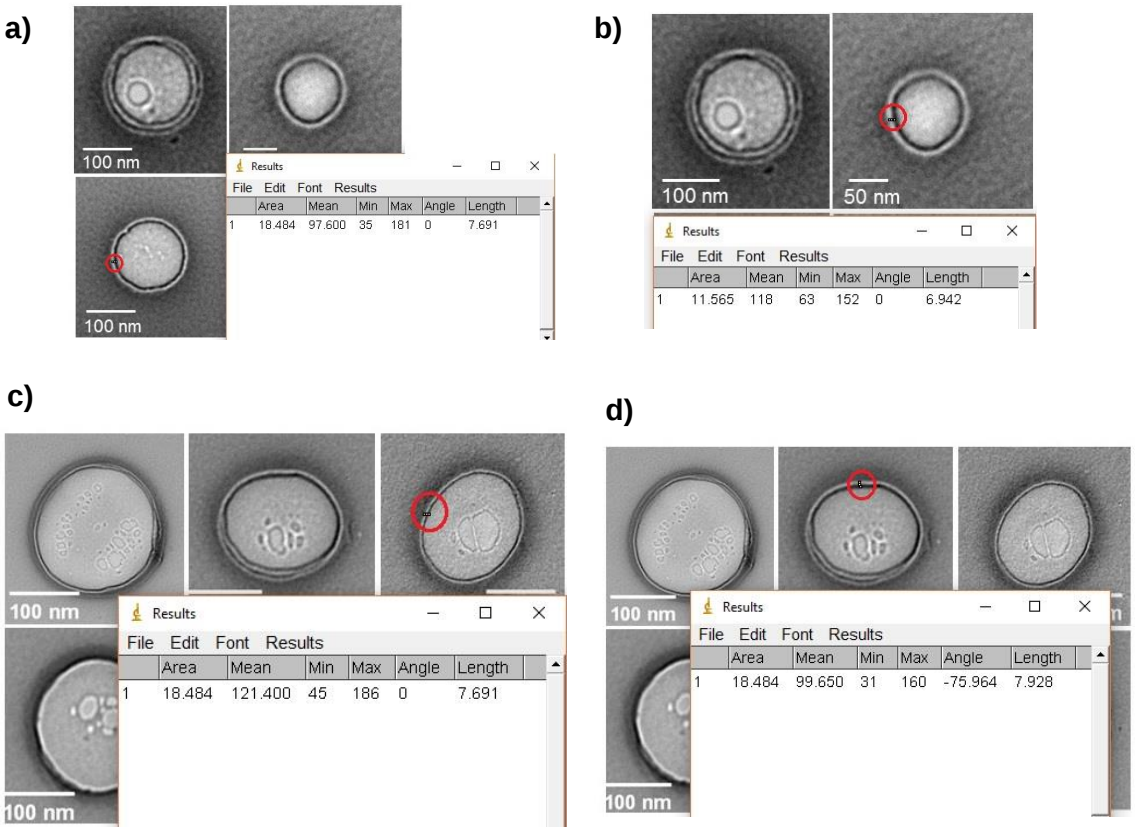

Figure 4.21: Bilayer thickness comparison, analyzed using Image J software: **(a)** and **(b)** before irradiation (Figure 4.1), **(c)** and **(d)** after UV irradiation (SI-Fig. 4.13).

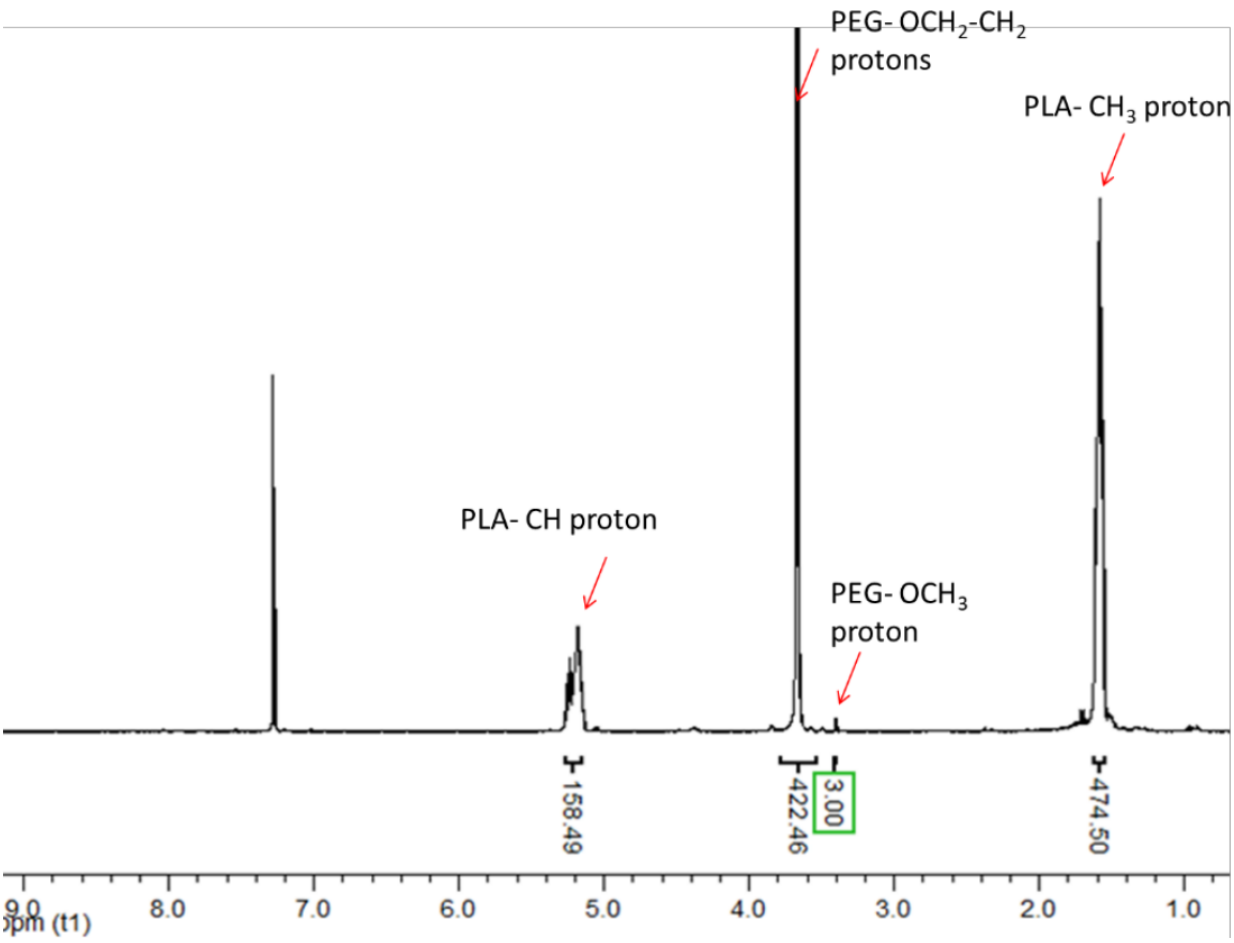

Figure 4.22: NMR characterization of P2. Calculation of molecular weight of P2. Number of PEG repeats: 423/4=106. The molecular weight of the PEG block was 106×44 (M_w of one PEG repeat) = 4670 Da. Number of PLA repeats (defined in supplementary scheme 1)= 158/2= 79. Molecular weight of the PLA block= 144(M_w of one PLA repeat unit) × (159/2) = 11, 376 Da. Therefore, the molecular weight from NMR= 16, 046 Da.

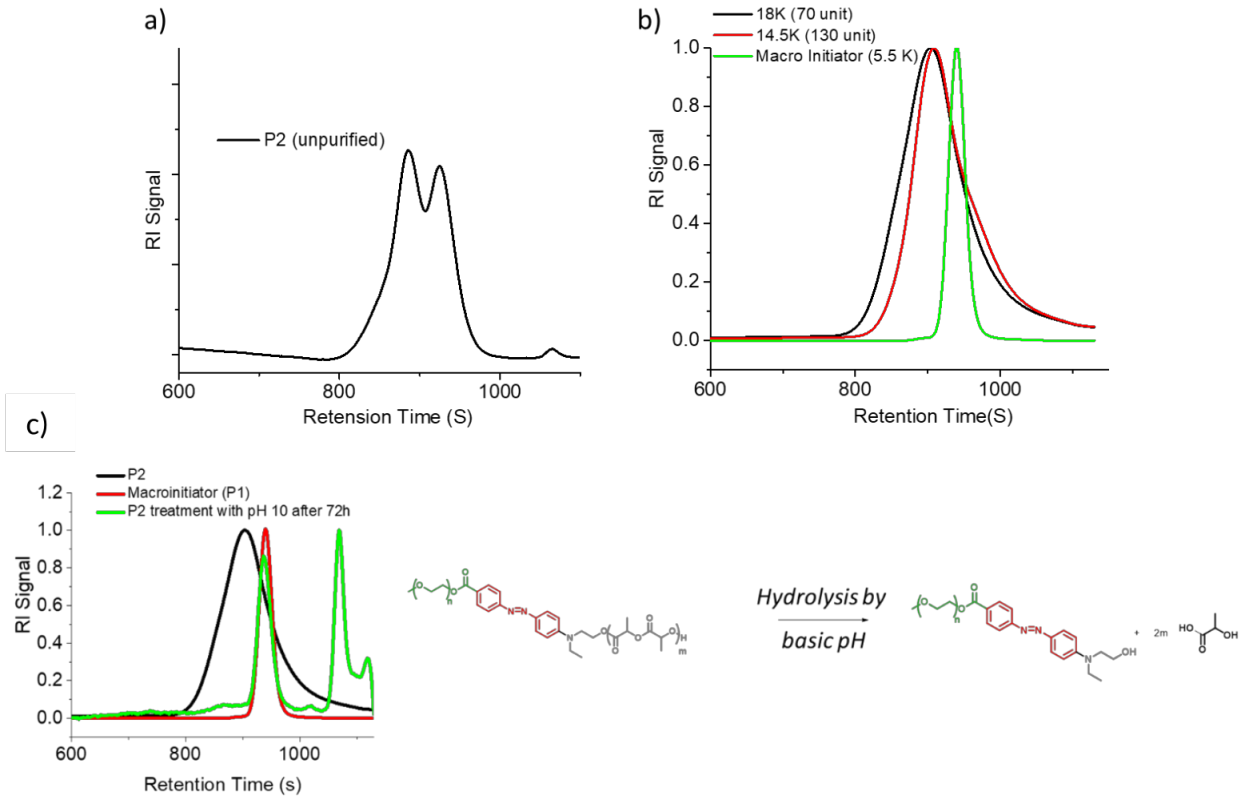

Figure 4.23: PC characterization of P2. **a.** A bimodal distribution was observed in the GPC before the polymer was purified by dialysis. **b.** Molecular weight of two different batches of PEG-Azo-PLA synthesized. The 18K batch was used for all the analysis in this report. **c.** GPC analysis of P2 after treatment with NaOH, pH 10. The PLA segments get hydrolyzed in these conditions and the reappearance of the P1 peak and smaller molecular weight aggregates, confirms the presence of PEG and PLA blocks in this polymer.

CHAPTER 5

CHEMICAL STRUCTURE EFFECTS TO MOLECULAR GLASS PHOTO RESISTS

This chapter is the culmination of a short internship with IBM at their research facility in Almaden, CA. While there, under the advisement of Jed Pitera, I simulated molecular glass systems that were previously studied internally, and worked with some of the experimentalist like Daniel Sanders. These were no longer industrial relevant, but had similarities to molecules still being studied, however, are proprietary. In this chapter there are references to experimental results, these were shared communications with me while I was there. Unfortunately, there is no paper or shared data to reference for it.

5.1 Introduction

Photolithography has been one of the main driving forces in miniaturization and advancement within the semiconductor industry. In this process, a mask and ultra-violet light is used to create a number of copies featuring nano-sized features by imprinting nano-sized features onto a photosensitive substrate, which is coated on a silicon wafer.[2] This photosensitive material, also known as photoresists or resists, are chemically altered in the exposed regions, typically changing the solubility of the region. This process is limited by the wavelength of light used, however the 193 nm ArF excimer lasers have been used for over a decade due to further advancements such as immersion technology[123] and multi-patterning technology[156, 71, 166] for resolution enhancement.

Industry is always pushing for continually shrinking length scales, with the current 10 nm node and soon 7 nm node release, which has feature sizes on the tens on nanometers. Currently, polymer based chemically amplified resists are the most commonly used photoresist material. However, as the features enter into the sub-10nm range new materials for resists may need to be considered. Resist performance is measured by a number of factors including,

but not limited to: resolution, line width roughness (LWR), line edge roughness (LER), and defectivity control.[84] The large size and poly-dispersity of polymeric resists have been identified as a limiting factor in resolution, which can cause undesirable fluctuations increasing LER.[34]

Molecular glass resists have been proposed as a possible alternative to the current polymeric systems. These materials can have the desired high thermal stability and glass transitions temperatures with smaller molecular weight and more reproducible chemical structure. Thus the material is mono-disperse and smaller molecular weight, which has been associated with lower LER.[34] As stated in Ref. 34, the more "pixel" like structure of the molecular glasses compared to the polymeric systems is believed to improve the resolution of the resists and capture the smaller feature designs.

In this study we look at three candidates for molecular glass photo-resists, or at least the base structures for future development. The three molecules, 1,3,5-tris(3-ethynylphenyl)benzene, 1,3,5-tris(2-phenylethynyl)benzene, and 1,3,5-tris-(4-ethynylphenyl)benzene, have the same molecular weight and vary only based on location of ethynyl group. The 1,3,5-tris(2-phenylethynyl)benzene molecule has been reported before as a high-temperature thermoset.[22] This comparative study will give information on how simply changing the location of a triple bond, which effects the stiffness and radius of gyration of the molecule, has on the glass and structural properties of the system. The ethynyl group is not only of interest for its effect on the molecules rigidity, but it is the active locations for the photo-resist. Under the right conditions and UV irradiation, these sites can cross-link form joint networks. The reaction and intermediates are still not well understood for these molecules, but it is known that acetylene can thermally trimerize to benzene, for instance.[149] Thus the structural differences between the molecules and the confinement effects has on the structural properties, particularly those involving the ethynyl coordination, are of special interest.

5.2 Methods

All-atom simulations were performed using the all-atom optimized potential for liquid simulations (AA-OPLS) force field.[69, 72] An updated dihedral potential across the bond between two phenyl rings was used.[25] Following a similar procedure to Ref. 25, a weak dihedral potential was calculated and implemented for across the triple bond between two phenyl rings as shown in the supporting information (Fig. 5.4). Bulk simulations were conducted using a Nosé-Hoover thermostat and barostat for constant temperature and pressure, respectively.[91] All simulations were performed using the Large-Scale Atomic/Molecular Massively Parallel Simulator (LAMMPS) package[111] with a simulation time step of 0.001 ps. The covalent hydrogen bonds were constrained by the SHAKE algorithm[122] and electrostatics were solved using the Particle-Particle-Particle-Mesh algorithm[61]. Each system had 1200 molecules (57,600 atoms) and the box lengths at 450K were on average about 9.3nm for the more dense molecules considered. The longest internal molecular distance for 1,3,5-tris-(4-ethynylphenyl)benzene, or the para case, is about 16 Å. Thus, the box length was typically about 5 to 6 times the molecular length of the molecules considered. The unmodified AA-OPLS parameters gave a simulation T_{g} of about 378K for the para case with a cooling rate of 10 K/ns. This value is higher than the reported melting temperature of $\approx$ 360K, as stated in the supporting information of Ref. 146, which is unphysical. In order to correct for this, the σ and ϵ Lennard-Jones values for the carbon atoms were reduced by 5% from the original values in the AA-OPLS force field for all molecules considered. After this change, a reasonable simulation T_{g} of about 350K for the para case at the same cooling rate is obtained.

The bulk of a trench was simulated by imposing a lower and upper wall in the z coordinate at a fixed width of 10 or 5 nm, whereas the x and y dimensions were periodic and coupled to a Nosé-Hoover barostat. Molecules were added to the system until the equilibrium lengths for the x and y dimensions were between 9 and 10 nm at a pressure of 1 bar and temperature of 450 K. The walls interacted via a 9-3 Lennard-Jones potential with parameters used for

silicon[151], ϵ = 0.584 Kcal/mol and σ= 3.3855Å, and a cut-off of 14Å. A slab geometry with slab volfactor of 3.0 was used for the electrostatics calculation.[160]

5.3 Results and Discussion

Cross-linking reactions are dependent on the location of the ethynyl groups within the molecules. In order for the reaction to occur, the proper coordination needs to be reached for the reaction to proceed and the intermediate transition states to be obtained. Three molecules of the same molecular weight were studied 1,3,5-tris(3-ethynylphenyl)benzene, 1,3,5-tris(2-phenylethynyl)benzene, and 1,3,5-tris-(4-ethynylphenyl)benzene, which will be referred to as meta, interior, and para, respectively, from here on. As the names indicate, these structures differ only by the location of the ethynyl groups as highlighted in Figure 5.1. This modification in chemical structure causes major changes in the phase behavior and properties of the material. The para and interior case both are more prone to crystallization than the meta case. Moreover, the interior case has a higher glass transition temperature (T_g) than the para and meta cases, and the meta case has a lower T_g than the para case.

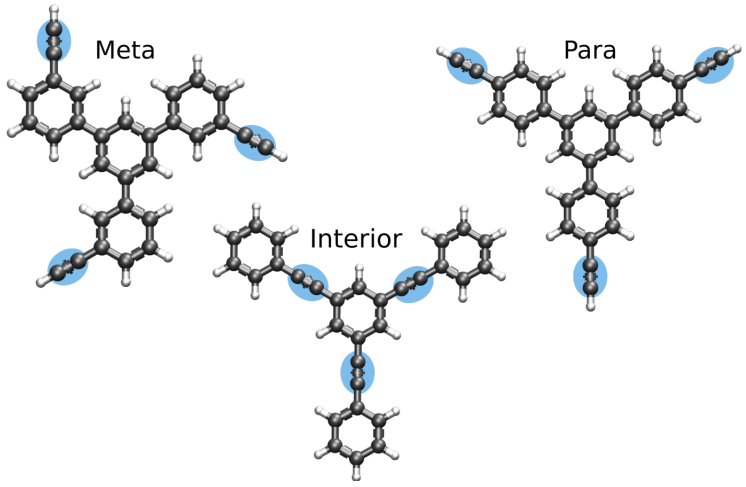

Figure 5.1: The three different molecules considered herein are drawn with all atoms in the same plane. Each differ based on the location of the triple bond ethynyl groups (highlighted in blue). From left to right: 1,3,5-tris(3-ethynylphenyl)benzene (**Meta**), 1,3,5-tris(2-phenylethynyl)benzene (**Interior**), and 1,3,5-tris-(4-ethynylphenyl)benzene (**Para**).

Bulk homogeneous simulations were conducted of each molecule as described in the Methods section. Rotational autocorrelations were calculated based on the unit normal of the center phenyl ring as described in the supporting information. This acts as a measure of local relaxation, as the molecules are able to rotate around and lose memory of its initial position. Moreover, it is an easily accessible measure of the materials relaxation times for evaluating if the material is in a glassy state on simulation timescales. Cooling runs with a cooling rate of 10K/ns were also used to estimate the fictive temperature (T_{f}), at which the material falls out of equilibrium and becomes glassy. This temperature will be referred to as the simulated glass transition temperature or simply T_{g} from here on. For comparison, the rotational relaxation, τ_{rot}, is listed for temperatures 450K and 400K and the calculated T_{g} in Table 5.1. In agreement with experimental results, the interior case has the highest T_{g} whereas the meta and para cases have very close T_{g} values. However, the τ_{rot} for the para case is consistently higher than the meta case by almost a factor of two for all temperatures measured (supporting information). This implies that the para case would fall out of equilibrium at a higher temperature than the meta case and this deviation could possibly widen as they reach experimental timescales.

Molecule	$\rho_{450\ \mathrm{K}}$ (g/cm^3)	$\tau_{\mathrm{rot,\ 450K}}$ (ns)	$\tau_{\mathrm{rot,\ 400K}}$ (ns)	T_{g} (K) 10 K/ns
Interior	0.946 ± 0.003	0.929	11.8	364
Para	0.991 ± 0.004	0.622	4.45	351
Meta	0.989 ± 0.004	0.369	2.31	349

Table 5.1: Glass Properties for each molecule. The average density, ρ, is calculated at 450K. The rotational relaxation τ_{rot} is calculated from the rotational autocorrelation function of the unit normal vector of the center benzene ring. A stretched exponential, $\exp(-(\frac{t}{\tau_{\mathrm{rot}}})^{\beta})$, is then fit to the resulting curve (supporting information). The T_g is calculated from a cooling run with a cooling rate of 10 K/ns.

The ability to cross-link is of interest, and thus we wanted to evaluate the differences in structural properties of the different materials. Radial distribution functions (rdf) were calculated for both the ethynyl group atoms and the center-of-geometry (COG) of the phenyl rings at a temperature of 450K (Fig. 5.2). This temperature was chosen as all systems are

able to locally relax and proper ensemble averaging can be attained. The interior case has a much sharper peak at about 5.5Å in the phenyl ring rdf than the meta and para case (Fig. 5.2a). The ethynyl groups cause some steric hindrance in the meta and para case whereas the interior case the external phenyl groups are more exposed and are able to more freely rotate. The first peak and exclusion area afterwards occur at the same distance for all three molecules. Related to the ability to cross-link, the rdf of the ethynl groups provide structural information for the liquid state as to how close these groups are coming into contact. For both the meta and para case, the initial peak occurs at a little under 4Å. From there the two rdf's diverge as meta has more of an exclusion between the first and second shell relative to the para case. In the para molecule, the positions of the ethynyl groups are all relatively fixed; however, in the meta case the ethynyl groups move with the rotation of the biphenyl dihedral. There is more variation in the relative distances between intramolecular ethynyl groups. This variation causes the second peak in the rdf to be lower relative to the para case. Based on steric repulsions, it was thought that the interior case would not be a good cross-linker. However, it has been seen experimentally to cross-link efficiently and even though the first peak is lower than 1 in the rdf it is about 0.8 only shifted slightly farther away to about 5Å relative to the para and meta case.

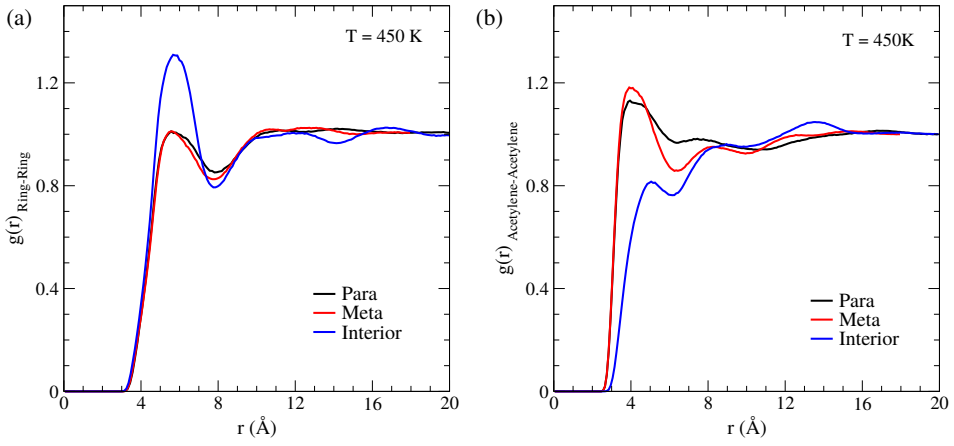

Figure 5.2: Radial distribution functions calculated at 450 K of the intermolecular (a) center-of-mass of the benzene rings and (b) the ethynyl groups for the para (black), meta (red), and interior (blue) molecular structures.

Confinement effects caused by shrinking feature sizes were explored by mimicking the bulk region of trench as depicted in the insert of Fig. 5.3c. The meta case was only explored as the other two molecules have been observed to be prone to crystallization. The width of the trench was fixed at either 10 or 5 nm wide and the walls interacted via a 9-3 Lennard-Jones potential with parameters set to mimic silicon.[151] Figure 5.3(a-f) display the density profile, Debye-Waller factor, and the S_z average orientation order parameter as a function of z, where the walls are located at the min and max values of z. The Debye-Waller factor is the average mean-squared-displacement of the hydrogen atoms for a fixed time step, in this case a time step of 10 ps was used. For orientation information is given by the S_z order parameter defined as

$$S_z = \langle P_2(\mathbf{n} \cdot \mathbf{n}_z) \rangle = \frac{3}{2}\langle \cos^2(\alpha) \rangle - \frac{1}{2} \tag{5.1}$$

where P_2 is the second Legendre polynomial, $\mathbf{n}$ is the unit normal of the center phenyl ring, and $\mathbf{n}_z$ is the unit vector normal to the walls. S_z values range from -0.5 to 1.0, where -0.5 indicates that unit normals average to be completely perpendicular to $\mathbf{n}_z$, a value of 1.0 for perfect alignment with $\mathbf{n}_z$, and 0 for when the average orientation is random. In all plots of Fig. 5.3(a-f), there is a layering effect caused by the surface of the trench. The denisty profiles for both the 10nm and 5nm cases show 3 distinct peaks near the interface, and according to the S_z profiles the molecules are oriented such that the normals of the center ring is mostly aligned on average with the normal of the wall surface. The peaks all decay as you move further into the film, and appear to have the strongest effect within 10Å of the wall. However, in the 5nm case there is still noticeable peaks above the noise near the center of the film as shown in insert of Fig. 5.3f. Thus, the layering effect is not able to decay completely. Moreover, the Debye-Waller factor, which is associated with local mobility and free volume, also does not have a plateau region in the 5nm case as it does in the 10nm case.

The rdf's of the phenyl rings or the ethynyl groups in the center bulk regions of the trenches do not change much given the slight layering effect in the 5nm case (Fig. 5.3g). However, the rdf's do not extend into the decay region as the rdf's do not converge to 1.0

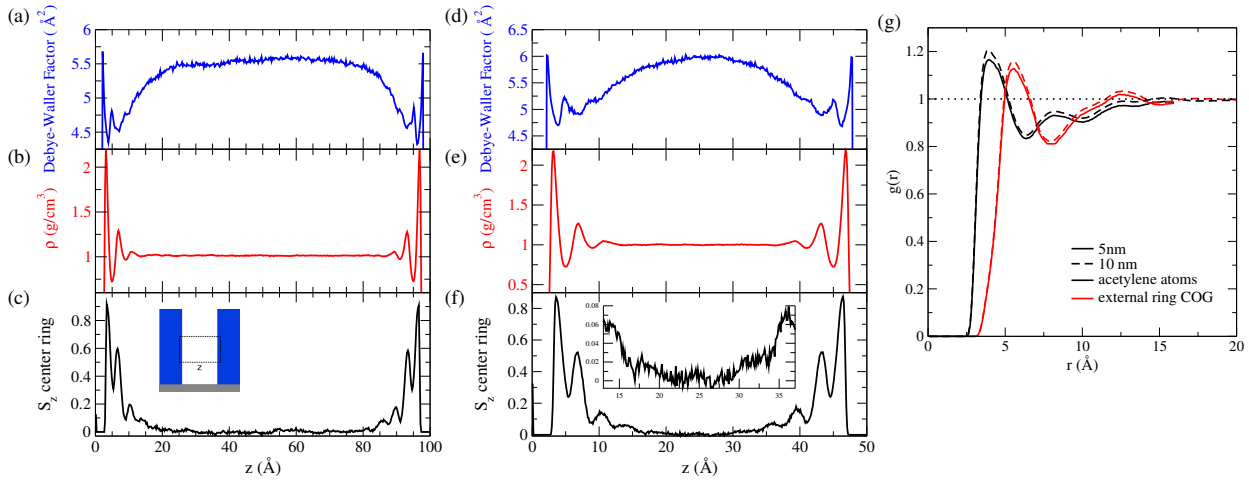

Figure 5.3: Two wall confinement of the meta case, simulation of the bulk region of a trench as pictured in the insert of (c) for (a-c) 10nm wide and (d-f) 5nm wide trench. The Debye-Waller factor (a and d), the density (b and e), and the molecular orientation order parameter (c and f) relative to the normal of the center benzene ring as functions z location. The insert in (f) is a zoomed in plot of the S_z order parameter in the middle of the trench. (g) The ethynyl (black) and external benzene ring (red) radial distribution function for both 5nm (solid) and 10nm (dashed) case.

until about a distance of 16Å as seen in Fig. 5.2 as well. Given the slight layering affect that is already noticeable in the bulk region for the 5nm case and the distance it takes for the rdf to converge to 1.0, any trench width less than 5nm would have strong layering effects all the way through the material. Already for the 5nm case, about half the material falls into the region within 1 nm of the walls that have high alignment as observed in the S_z profiles. This may have negative effects on the materials ability to cross-link with the low bulk percentage. The 10 nm case still has a larger percentage that can be considered bulk and likely would not suffer much from confinement effects.

5.4 Conclusions

The simulations performed herein, demonstrate some of the property changes observed experimentally for changing the location of the triple bonded ethynyl group. The T_g and susceptibility to crystallization of of the material is dependent upon the location as well as the ability to cross-link. Even though the ethynyl groups are more sterically shielded in

the interior case, the rdf suggests that these groups still come within the same distance as those of the para and meta cases, just more depleted. However, this restrictive structure could cause the neighboring molecules to be in a more aligned relative configuration for cross-linking for the intermediate state to form, which may explain the good cross-linking behavior observed experimentally for the interior case. The trench simulations suggests that, as far as the material is concerned, confinement effects will not distort the bulk region of a molecular glass until around a width of 5nm.

5.5 Supporting Information

5.5.1 Ethynyl Dihedral

The dihedral potential across the triple bond connecting the two phenyl rings in the interior case was calculated using Gaussian[30, 46] and slowly rotating the dihedral angle. The OPLS dihedral potential is then numerically fit to the calculated potential. The resulting coefficients in kcal/mol were:

$$V_1 = \text{-}0.0048,\ V_2 = 0.6347,\ V_3 = 0.0045\ ,\ \text{and}\ V_4 = \text{-}0.0035$$

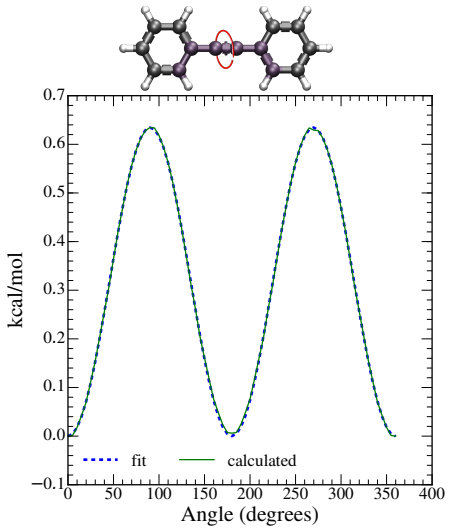

Figure 5.4: The calculated dihedral potential via stepwise Gaussian calculations (solid) and the corresponding fit (dashed). Dihedral calculated is highlighted above.

5.5.2 Rotational Relaxation

A relaxation time τ_{rot} was calculated by fitting a stretched exponential,

$$\exp\left(-\left(\frac{C(\theta,t)}{\tau_{\text{rot}}}\right)^{\beta}\right),$$

to the rotational autocorrelation function with respect to the unit normal of the center ring as pictured in Fig. 5.5. The τ_{rot} and β for each fit are provided in the corresponding plots.

In Figure 5.5, $\cos(\theta)$ is defined as

$$C(\theta, t) = \langle \mathbf{n}_0 \cdot \mathbf{n}_t \rangle = \langle \cos(\theta, t) \rangle$$

such that $\mathbf{n}_0$ and $\mathbf{n}_t$ are the unit normals of the center ring at time zero and time t, respectively. Thus, θ is the average angle between the two vectors at time t.

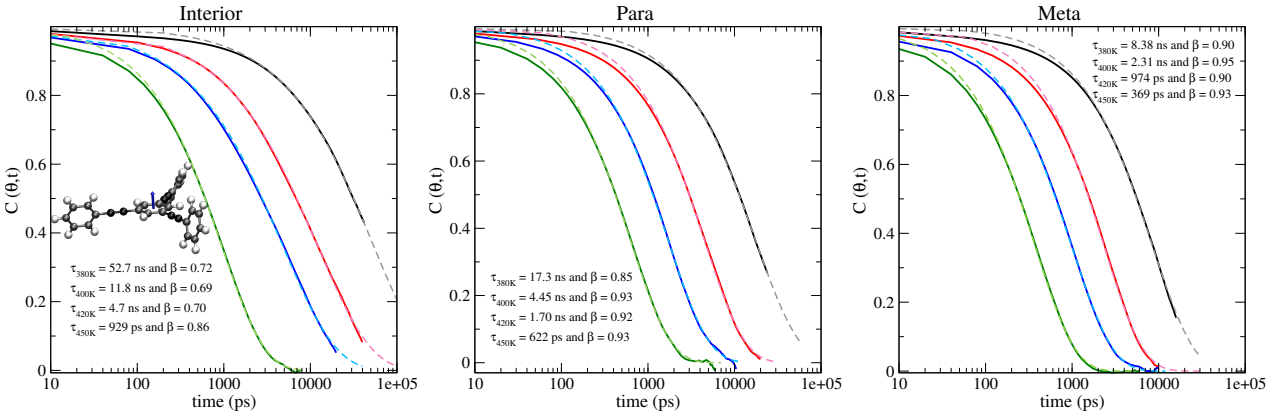

Figure 5.5: The rotational autocorrelation functions for the interior, para, and meta case (from left to right) with respect to the unit normal of the center benzene ring as shown within the interior case plot. Four different temperatures were measured: 450K (green), 420K (blue), 400K (red), and 380K (black). Stretched exponentials were fit to each plot (dashed lines) and the fit parameters are listed within each plot.

CHAPTER 6

CONCLUSIONS AND FUTURE WORK

To conclude, this thesis has been about investigating different ways to tune or change the properties of an organic glass. Either through the formation process of physical vapor-deposition (PVD), using photo-isomerization to either act as a switch (Chapter 4) or irreversibly change the glass (Chapter 3), or by changing the chemical structure of the molecule itself (Chapter 5). Each of the projects presented herein can be expanded and explored further.

In Chapter 2 we were able to provide the first all-atom molecular dynamics simulation of an experimentally verified stable glass former. Vapor deposition led to films with enhanced kinetic stability and lower inherent structure energies relative to the liquid-cooled glasses; the onset temperatures were found to be up to 11 K above those of the liquid cooled films. Even the small molecular structure of ethylbenzene displayed anisotropic ordering at the vacuum interface with the equilibrium liquid, which was then "frozen" into the films at different points depending on the substrate temperature used, which is consistent with, and further enforces, the mechanism proposed in Reference 88. The properties associated with charge transport, the distribution of site-energies and the transfer integrals between molecular sites, were shown to improve for the vapor deposited glasses relative to those of the liquid-cooled. This improvement seemed to be attributed to both the anisotropic ordering of the molecules as well as the increased density observed for PVD. Similar studies should be performed for more industry relevant organic semiconductors, where their large molecular structure may favor a higher degree of anisotropy in the films. Moreover, pi-stacking is more favorable for the more common organic semiconductors, which may lead to more favorable configurations in the better equilibrated vapor-deposited glasses.

Continuing the study of the effect vapor-deposition has on the glass properties. We demonstrated in Chapter 3 that PVD glasses can be much more photostable than those formed by liquid-cooling. The improvement in stability was highly correlated with the im-

proved density observed for stable glass formers. This led us to believe that the efficient packing formed by vapor deposition causes a higher energy barrier for molecular rearrangement. In the simulations, we were able to show that the behavior will become similar in the limit of a really strong driving force for isomerization, which overcomes whatever barriers the packing creates. Further studies of PVD effects on photo-reactivity of the glasses have been performed by my collaborator Yue Qiu, showing PVD films to be more resistant to photodegradation.[114] It is of interest to see how doping a stable glass former with a photo-reactive azobenzene derivatives, rather than the entire film being able to react. What would the composition effects be, such as how much dopant would be required to see an effect in the vapor deposited films versus that of liquid cooled? What kind of relationship would there be between host molecular structure and size relative to that of the azobenzene derivative? These would all be related to the "photo-softening" effect that is utilized in Chapter 4.

Chapter 4 we demonstrated that activated leakage of a vesicles can be achieved by incorporating a single azobenzene unit into the backbone of an amphiphilic diblock copolymer, PEG-azo-PLA, located at the interface of hydrophilic polyethyleneglycol (PEG) and hydrophobic poly-DL-lactide (PLA) blocks. The PLA block has a T_g higher than 298K and acts as a gate keeper. Upon irradiation, the mobility of the PLA region increases due to the mechanical strain imposed on the film from the isomerization of the azobenzene units. Once the light input is stopped and the isomerization reactions ceases, the films reseal. This process can be repeated until the contents have no thermodynamic drive to leave the now porous vesicles. As mentioned, this is an example of "photo-softening" of a glassy matrix by an azobenzene unit. One of the first examples of measurable release of a dye molecule from the glassy matrix upon irradiation. Computationally, more work can be done to look at the mechanics of the system. For instance, calculate the amount of work done by a successful isomerization or can calculate the stress imposed on the membrane for different percentage of azobenzene units reacting.

Finally, Chapter 5 we demonstrated that by changing the location of triple bonded

ethynyl groups within a molecule can change the glass properties of the material. This is due to the change in internal degrees of freedom of the molecules. What is of interest is the properties that change that relate to cross-linking; the molecule that was thought to have steric hindrance reacts quite well in experiments. We attempted to start exploring this by simply looking at the relative radial distribution functions for the relevant reactive atoms. However, it is still being studied by members at IBM what the reaction pathway is for these types of molecules to cross-link. Once the structures of the transition states are better understood for the possible pathways, further studies can be done to look at how the packing of these materials either favor or disfavor these reactions. Such a study would then provide further insight into how confinement effects may affect the molecules ability to cross-link and act as a photo-resist.

REFERENCES

[1] Mark James Abraham, Teemu Murtola, Roland Schulz, Szilárd Páll, Jeremy C Smith, Berk Hess, and Erik Lindahl. GROMACS: High performance molecular simulations through multi-level parallelism from laptops to supercomputers. *SoftwareX*, 1-2:19–25, 2015.

[2] G. M. Wallraff* And and W. D. Hinsberg. Lithographic Imaging Techniques for the Formation of Nanoscopic Features. 1999.

[3] Yasuo Norikane And and Nobuyuki Tamaoki*. Light-Driven Molecular Hinge: A New Molecular Machine Showing a Light-Intensity-Dependent Photoresponse that Utilizes the TransCis Isomerization of Azobenzene. 2004.

[4] Lucas W. Antony, Nicholas E. Jackson, Ivan Lyubimov, Venkatram Vishwanath, Mark D. Ediger, and Juan J. de Pablo. Influence of vapor deposition on structural and charge transport properties of ethylbenzene films. *ACS Central Science*, 3(5):415–424, 2017.

[5] Rafael Auras, Bruce Harte, and Susan Selke. An overview of polylactides as packaging materials. *Macromolecular Bioscience*, 4(9):835–864, 2004.

[6] Nathan Bakken, Jessica M. Torres, Jian Li, and Bryan D. Vogt. Thickness dependent modulus of vacuum deposited organic molecular glasses for organic electronics applications. *Soft Matter*, 7(16):7269, 2011.

[7] H M Dhammika Bandara and Shawn C Burdette. Photoisomerization in different classes of azobenzene. *Chem. Soc. Rev.*, 41(5):1809–1825, 2012.

[8] Paul F. Barbara, Thomas J. Meyer, and Mark a. Ratner. Contemporary Issues in Electron Transfer Research. *The Journal of Physical Chemistry*, 100(31):13148–13168, 1996.

[9] Heinz Bassler and Anna Kohler. Charge Transport in Organic Semiconductors. In *Top Curr Chem*. Springer-Verlag, Berlin Heidelberg, 2012.

[10] M. S. Beasley, M. Tylinski, Y. Z. Chua, C. Schick, and M. D. Ediger. Glasses of three alkyl phosphates show a range of kinetic stabilities when prepared by physical vapor deposition. *The Journal of Chemical Physics*, 148(17):174503, 2018.

[11] Andrew A Beharry and G Andrew Woolley. Azobenzene photoswitches for biomolecules. *Chem. Soc. Rev.*, 40(8):4422–4437, 2011.

[12] Othmane R. Bennani, Tayel A. Al-Hujran, Jean-Michel Nunzi, Ribal Georges Sabat, and Olivier Lebel. Surface relief grating growth in thin films of mexylaminotriazine-functionalized glass-forming azobenzene derivatives. *New Journal of Chemistry*, 39(12):9162–9170, 2015.

[13] Herman Berendsen. Transport Properties Computed by Linear Response through Weak Coupling to a Bath. *Comp Simul Mat Sci*, 205, 1991.

[14] Deepanjan Bhattacharya and Vlad Sadtchenko. Vapor-deposited non-crystalline phase vs ordinary glasses and supercooled liquids: Subtle thermodynamic and kinetic differences. *The Journal of Chemical Physics*, 142(16):164510, 2015.

[15] Job Boekhoven, AurelieM. Brizard, KrishnaN.K. Kowlgi, GerJ.M. Koper, Rienk Eelkema, and JanH. vanEsch. Dissipative self-assembly of a molecular gelator by using a chemical fuel. *Angewandte Chemie International Edition*, 49(28):4825–4828, 2010.

[16] Giovanni Bussi, Davide Donadio, and Michele Parrinello. Canonical sampling through velocity rescaling. *The Journal of Chemical Physics*, 126(1):014101, 2007.

[17] Yi-Hong Chen, Li-Yen Lin, Chih-Wei Lu, Francis Lin, Zheng-Yu Huang, Hao-Wu Lin, Po-Han Wang, Yi-Hung Liu, Ken-Tsung Wong, Jianguo Wen, Dean J. Miller, and Seth B. Darling. Vacuum-Deposited Small-Molecule Organic Solar Cells with High Power Conversion Efficiencies by Judicious Molecular Design and Device Optimization. *Journal of the American Chemical Society*, 134(33):13616–13623, AUG 22 2012.

[18] Yinshan Chen, Men Zhu, Audrey Laventure, Olivier Lebel, M. D. Ediger, and Lian Yu. Influence of hydrogen bonding on the surface diffusion of molecular glasses: Comparison of three triazines. *The Journal of Physical Chemistry B*, 121(29):7221–7227, 2017. PMID: 28651429.

[19] Zhen Chen and Ranko Richert. Dynamics of glass-forming liquids. xv. dynamical features of molecular liquids that form ultra-stable glasses by vapor deposition. *The Journal of Chemical Physics*, 135(12):124515, 2011.

[20] Y. Z. Chua, M. Tylinski, S. Tatsumi, M. D. Ediger, and C. Schick. Glass transition and stable glass formation of tetrachloromethane. *The Journal of Chemical Physics*, 144(24):244503, jun 2016.

[21] MD Cohen and GMJ Schmidt. Topochemistry .1. Survey. *Journal of the Chemical Society*, (JUN):1996–&, 1964.

[22] E.F. Connor, V.Y. Lee, T. Magbitang, C.J. Hawker, W. Volksen, R. Siemens, R.A. DiPietro, J.C. Hedrick, H.C. Kim, R.D. Miller, and J.L. Hedrick. First Example of a Nanoporous High-Temperature Polymer Thermoset: Eluding TransitionTime-Temperature Constraints Associated with Organic Thermosets. *Advanced Materials*, 16(17):1525–1529, Sep 2004.

[23] Veaceslav Coropceanu, Jrme Cornil, Demetrio A. da Silva Filho, Yoann Olivier, Robert Silbey, and Jean-Luc Brdas. Charge transport in organic semiconductors. *Chemical Reviews*, 107(4):926–952, 2007. PMID: 17378615.

[24] Christina R. Crecca and Adrian E. Roitberg. Theoretical study of the isomerization mechanism of azobenzene and disubstituted azobenzene derivatives. *Journal of Physical Chemistry A*, 110(26):8188–8203, JUL 6 2006.

[25] Markus K. Dahlgren, Patric Schyman, Julian Tirado-Rives, and William L. Jorgensen. Characterization of biaryl torsional energetics and its treatment in opls all-atom force fields. *Journal of Chemical Information and Modeling*, 53(5):1191–1199, 2013. PMID: 23621692.

[26] Shakeel S. Dalal and M. D. Ediger. Molecular Orientation in Stable Glasses of Indomethacin. *The Journal of Physical Chemistry Letters*, 3(10):1229–1233, may 2012.

[27] Shakeel S. Dalal, Zahra Fakhraai, and M. D. Ediger. High-Throughput Ellipsometric Characterization of Vapor-Deposited Indomethacin Glasses. *Journal of Physical Chemistry B*, 117(49, SI):15415–15425, DEC 12 2013.

[28] Shakeel S. Dalal, A. Sepulveda, Greg K. Pribil, Zahra Fakhraai, and M. D. Ediger. Density and birefringence of a highly stable α,α,β-trisnaphthylbenzene glass. *The Journal of Chemical Physics*, 136(20):204501, 2012.

[29] Shakeel S. Dalal, Diane M. Walters, Ivan Lyubimov, Juan J. de Pablo, and M. D. Ediger. Tunable molecular orientation and elevated thermal stability of vapor-deposited organic semiconductors. *Proceedings of the National Academy of Sciences*, 112(14):4227–4232, 2015.

[30] Stefan Dapprich, István Komáromi, K. Suzie Byun, Keiji Morokuma, and Michael J. Frisch. A new ONIOM implementation in Gaussian98. Part I. The calculation of energies, gradients, vibrational frequencies and electric field derivatives. *Journal of Molecular Structure: THEOCHEM*, 461-462:1–21, 1999.

[31] Kevin Dawson, Laura a Kopff, Lei Zhu, Robert J McMahon, Lian Yu, Ranko Richert, and M D Ediger. Molecular packing in highly stable glasses of vapor-deposited trisnaphthylbenzene isomers. *The Journal of chemical physics*, 136(9):094505, mar 2012.

[32] Kevin Dawson, Lei Zhu, Laura A. Kopff, Robert J. McMahon, Lian Yu, and M. D. Ediger. Highly Stable Vapor-Deposited Glasses of Four Tris-naphthylbenzene Isomers. *Journal of Physical Chemistry Letters*, 2(21):2683–2687, NOV 3 2011.

[33] Kevin J Dawson, Lei Zhu, Lian Yu, and M D Ediger. Anisotropic structure and transformation kinetics of vapor-deposited indomethacin glasses. *The journal of physical chemistry. B*, 115(3):455–463, 2011.

[34] Anuja De Silva, Nelson M. Felix, and Christopher K. Ober. Molecular Glass Resists as High-Resolution Patterning Materials. *Advanced Materials*, 20(17):3355–3361, sep 2008.

[35] P G Debenedetti and F H Stillinger. Supercooled liquids and the glass transition. *Nature*, 410(6825):259–67, mar 2001.

[36] a. Dieckmann, H. Bässler, and P. M. Borsenberger. An assessment of the role of dipoles on the density-of-states function of disordered molecular solids. *The Journal of Chemical Physics*, 99(10):8136, 1993.

[37] Jadranka Dokic, Marcel Gothe, Jonas Wirth, Maike V. Peters, Jutta Schwarz, Stefan Hecht, and Peter Saalfrank. Quantum Chemical Investigation of Thermal Cis-to-Trans Isomerization of Azobenzene Derivatives: Substituent Effects, Solvent Effects, and Comparison to Experimental Data. *Journal of Physical Chemistry A*, 113(24):6763–6773, JUN 18 2009.

[38] Ruijiao Dong, Bangshang Zhu, Yongfeng Zhou, Deyue Yan, and Xinyuan Zhu. Reversible photoisomerization of azobenzene-containing polymeric systems driven by visible light. *Polym. Chem.*, 4(4):912–915, 2013.

[39] John R Dorgan, Hans Lehermeier, and Michael Mang. Thermal and Rheological Properties of Commercial-Grade Poly(Lactic Acid)s. *Journal of Polymers and the Environment*, 8(1):1–9, jan 2000.

[40] M. D. Ediger. Perspective: Highly stable vapor-deposited glasses. *The Journal of Chemical Physics*, 147(21):210901, dec 2017.

[41] Ulrich Essmann, Lalith Perera, Max L. Berkowitz, Tom Darden, Hsing Lee, and Lee G. Pedersen. A smooth particle mesh ewald method. *The Journal of Chemical Physics*, 103(19):8577–8593, 1995.

[42] G.J. Fang, J.E. Maclennan, Y. Yi, M.A. Glaser, M. Farrow, E. Korblova, D.M. Walba, T.E. Furtak, and N.A. Clark. Athermal photofluidization of glasses. *Nature Communications*, 4:1521, feb 2013.

[43] Abbas Farazdel, Michel Dupuis, Enrico Clementi, and Ari Aviram. Electric-field induced intramolecular electron transfer in spiro .pi.-electron systems and their suitability as molecular electronic devices. a theoretical study. *Journal of the American Chemical Society*, 112(11):4206–4214, 1990.

[44] Ze Feng, Li Lin, Zeng Yan, and Yanlei Yu. Dual responsive block copolymer micelles functionalized by nipam and azobenzene. *Macromolecular Rapid Communications*, 31(7):640–644, 2010.

[45] Marcin Fialkowski, Kyle J M Bishop, Rafal Klajn, Stoyan K Smoukov, Christopher J Campbell, and Bartosz A Grzybowski. Principles and Implementations of Dissipative (Dynamic) Self-Assembly. *The Journal of Physical Chemistry B*, 110(6):2482–2496, 2006.

[46] M. J. Frisch, G. W. Trucks, H. B. Schlegel, G. E. Scuseria, M. A. Robb, J. R. Cheeseman, G. Scalmani, V. Barone, B. Mennucci, G. A. Petersson, H. Nakatsuji, M. Caricato, X. Li, H. P. Hratchian, A. F. Izmaylov, J. Bloino, G. Zheng, J. L. Sonnenberg, M. Hada, M. Ehara, K. Toyota, R. Fukuda, J. Hasegawa, M. Ishida, T. Nakajima, Y. Honda, O. Kitao, H. Nakai, T. Vreven, J. A. Montgomery, Jr., J. E. Peralta,

F. Ogliaro, M. Bearpark, J. J. Heyd, E. Brothers, K. N. Kudin, V. N. Staroverov, R. Kobayashi, J. Normand, K. Raghavachari, A. Rendell, J. C. Burant, S. S. Iyengar, J. Tomasi, M. Cossi, N. Rega, J. M. Millam, M. Klene, J. E. Knox, J. B. Cross, V. Bakken, C. Adamo, J. Jaramillo, R. Gomperts, R. E. Stratmann, O. Yazyev, A. J. Austin, R. Cammi, C. Pomelli, J. W. Ochterski, R. L. Martin, K. Morokuma, V. G. Zakrzewski, G. A. Voth, P. Salvador, J. J. Dannenberg, S. Dapprich, A. D. Daniels, . Farkas, J. B. Foresman, J. V. Ortiz, J. Cioslowski, and D. J. Fox. Gaussian∼09 Revision E.01, 2009. Gaussian Inc. Wallingford CT 2009.

[47] G Gabor and E Fischer. Spectra and cis-trans Isomerism in Highly Bipolar Derivatives of Azobenzene. *Journal of Physical Chemistry*, 75(4):581–&, 1971.

[48] Anne Helene Gelebart, Dirk Jan Mulder, Michael Varga, Andrew Konya, Ghislaine Vantomme, E. W. Meijer, Robin L. B. Selinger, and Dirk J. Broer. Making waves in a photoactive polymer film. *Nature*, 546(7660):632–636, jun 2017.

[49] N. Goga, A. J. Rzepiela, A. H. de Vries, S. J. Marrink, and H. J. C. Berendsen. Efficient algorithms for langevin and dpd dynamics. *Journal of Chemical Theory and Computation*, 8(10):3637–3649, 2012. PMID: 26593009.

[50] Jaritza Gomez, Jing Jiang, Ankit Gujral, Chengbin Huang, Lian Yu, and M. D. Ediger. Vapor deposition of a smectic liquid crystal: highly anisotropic, homogeneous glasses with tunable molecular orientation. *Soft Matter*, 12:2942–2947, 2016.

[51] Stefan Grimme. Do special noncovalent stacking interactions really exist? *Angewandte Chemie International Edition*, 47(18):3430–3434, 2008.

[52] R Hagen and T Bieringer. Photoaddressable polymers for optical data storage. *Advanced Materials*, 13(23):1805–1810, DEC 2001.

[53] BC Hancock and M Parks. What is the true solubility advantage for amorphous pharmaceuticals? *Pharmaceutical Research*, 17(4):397–404, APR 2000.

[54] J Harada and K Ogawa. X-ray diffraction analysis of nonequilibrium states in crystals: Observation of an unstable conformer in flash-cooled crystals. *Journal of the American Chemical Society*, 126(11):3539–3544, MAR 24 2004.

[55] Fatima Hassouna, Abdelghani Laachachi, David Chapron, Yamna El Mouedden, Valérie Toniazzo, and David Ruch. Development of new approach based on Raman spectroscopy to study the dispersion of expanded graphite in poly(lactide). *Polymer Degradation and Stability*, 96(12):2040–2047, 2011.

[56] Yaning He, Wei He, Renbo Wei, Zhen Chen, and Xiaogong Wang. Synthesizing amphiphilic block copolymers through macromolecular azo-coupling reaction. *Chem. Commun.*, 48(7):1036–1038, 2012.

[57] Julian Helfferich, Ivan Lyubimov, Daniel Reid, and Juan J de Pablo. Inherent structure energy is a good indicator of molecular mobility in glasses. *Soft matter*, 12(27):5898–904, jul 2016.

[58] Berk Hess, Henk Bekker, Herman J. C. Berendsen, and Johannes G. E. M. Fraaije. LINCS: A linear constraint solver for molecular simulations. *Journal of Computational Chemistry*, 18(12):1463–1472, sep 1997.

[59] Berk Hess, Carsten Kutzner, David van der Spoel, and Erik Lindahl. GROMACS 4: Algorithms for Highly Efficient, Load-Balanced, and Scalable Molecular Simulation. *Journal of Chemical Theory and Computation*, 4(3):435–447, March 2008.

[60] Hideaki Hikawa, Masaharu Oguni, and Hiroshi Suga. Construction of an adiabatic calorimeter for a vapor-deposited sample and thermal characterization of amorphous butyronitrile. *Journal of Non-Crystalline Solids*, 101(1):90 – 100, 1988.

[61] R.W Hockney and J.W Eastwood. *Computer Simulation Using Particles*. Taylor & Francis, 1988.

[62] RJ Holmes, SR Forrest, YJ Tung, RC Kwong, JJ Brown, S Garon, and ME Thompson. Blue organic electrophosphorescence using exothermic host-guest energy transfer. *Applied Physics Letters*, 82(15):2422–2424, APR 14 2003.

[63] Kikujiro Ishii, Hideyuki Nakayama, Shin Hirabayashi, and Ryo Moriyama. Anomalously high-density glass of ethylbenzene prepared by vapor deposition at temperatures close to the glass-transition temperature. *Chemical Physics Letters*, 459(16):109 – 112, 2008.

[64] Kikujiro Ishii, Hideyuki Nakayama, and Ryo Moriyama. Nonequilibrium and relaxation in deeply supercooled liquid of isopropylbenzene obtained through glass transition from vapor-deposited glass. *The journal of physical chemistry. B*, 116(3):935–42, jan 2012.

[65] Kikujiro Ishii, Yuki Yokoyama, Ryo Moriyama, and Hideyuki Nakayama. Liquid-Liquid Relaxation in the Supercooled Liquid State of Ethylbenzene: Thermal Studies Using a Prototype DTA Sensor for the Study of Vapor-deposited Samples. *Chemistry Letters*, 39(9):958–960, sep 2010.

[66] Masahide Itoh, Kenji Harada, Shun-ichi Kamemaru, and Toyohiko Yatagai. Holographic Recording on Azo-benzene Functionalized Polymer Film. *Japanese Journal of Applied Physics*, 43(7B):4968–4971, jul 2004.

[67] Nicholas E. Jackson, Kevin L. Kohlstedt, Lin X. Chen, and Mark A. Ratner. A n-vector model for charge transport in molecular semiconductors. *The Journal of Chemical Physics*, 145(20):204102, 2016.

[68] Nicholas E. Jackson, Brett M. Savoie, Lin X. Chen, and Mark a. Ratner. A Simple Index for Characterizing Charge Transport in Molecular Materials. *The Journal of Physical Chemistry Letters*, 1021(1):1018–1021, 2015.

[69] William L. Jorgensen, David S. Maxwell, and Julian Tirado-Rives. Development and testing of the opls all-atom force field on conformational energetics and properties of organic liquids. *Journal of the American Chemical Society*, 118(45):11225–11236, 1996.

[70] Joshua Jortner. Temperature dependent activation energy for electron transfer between biological molecules. *J. Chem. Phys.*, 64(12):4860–4867, 1976.

[71] Andrew B. Kahng, Chul-Hong Park, Xu Xu, and Hailong Yao. Layout Decomposition Approaches for Double Patterning Lithography. *IEEE Transactions on Computer-Aided Design of Integrated Circuits and Systems*, 29(6):939–952, jun 2010.

[72] George A. Kaminski, Richard A. Friesner, Julian Tirado-Rives, and William L. Jorgensen. Evaluation and reparametrization of the opls-aa force field for proteins via comparison with accurate quantum chemical calculations on peptides. *The Journal of Physical Chemistry B*, 105(28):6474–6487, 2001.

[73] Peter Karageorgiev, Dieter Neher, Burkhard Schulz, Burkhard Stiller, Ullrich Pietsch, Michael Giersig, and Ludwig Brehmer. From anisotropic photo-fluidity towards nanomanipulation in the optical near-field. *Nature Materials*, 4(9):699–703, sep 2005.

[74] K L Kearns, S F Swallen, M D Ediger, T Wu, and L Yu. Influence of substrate temperature on the stability of glasses prepared by vapor deposition. *Journal of Chemical Physics*, 127(15):9, oct 2007.

[75] Kenneth L. Kearns, Hong-Yeop Na, Robert D. Froese, Sukrit Mukhopadhyay, Hunter Woodward, Dean Welsh, Timothy De Vries, David Devore, Peter Trefonas, and Liang Hong. Molecular orientation, thermal behavior and density of electron and hole transport layers and the implication on device performance for oleds. volume 9183, pages 91830F–91830F–12, 2014.

[76] Kenneth L. Kearns, Stephen F. Swallen, M. D. Ediger, Tian Wu, Ye Sun, and Lian Yu. Hiking down the energy landscape: Progress toward the Kauzmann temperature via vapor deposition. *Journal of Physical Chemistry B*, 112(16):4934–4942, APR 24 2008.

[77] Johanna M Kuiper and Jan B F N Engberts. H-Aggregation of Azobenzene-Substituted Amphiphiles in Vesicular Membranes. *Langmuir*, 20(4):1152–1160, 2004.

[78] Prajakta Kulkarni, Manas K Haldar, Seungyong You, Yongki Choi, and Sanku Mallik. Hypoxia-Responsive Polymersomes for Drug Delivery to Hypoxic Pancreatic Cancer Cells. *Biomacromolecules*, 17(8):2507–13, 2016.

[79] Jayant Kumar, Lian Li, Xin Li Jiang, Dong-Yu Kim, Taek Seung Lee, and Sukant Tripathy. Gradient force: The mechanism for surface relief grating formation in azobenzene functionalized polymers. *Applied Physics Letters*, 72(17):2096, jun 1998.

[80] I Kushida, M Ichikawa, and N Asakawa. Improvement of dissolution and oral absorption of ER-34122, a poorly water-soluble dual 5-lipoxygenase/cyclooxygenase inhibitor with anti-inflammatory activity by preparing solid dispersion. *Journal of Pharmaceutical Sciences*, 91(1):258–266, JAN 2002.

[81] Sang-Min Lee, Haimei Chen, Christine M Dettmer, Thomas V O'Halloran, and Son-Binh T Nguyen. Polymer-Caged Lipsomes: A pH-Responsive Delivery System with High Stability. *Journal of the American Chemical Society*, 129(49):15096–15097, 2007.

[82] E. Leon-Gutierrez, G. Garcia, M. T. Clavaguera-Mora, and J. Rodriguez-Viejo. Glass transition in vapor deposited thin films of toluene. *Thermochimica Acta*, 492(1-2):51–54, AUG 10 2009. 10th Lahnwitz Seminar on Calorimetry, Rostock, GERMANY, JUN 08-13, 2008.

[83] Edgar Leon-Gutierrez, Alfonso Sepúlveda, Gemma Garcia, Maria Teresa Clavaguera-Mora, and Javier Rodríguez-Viejo. Stability of thin film glasses of toluene and ethylbenzene formed by vapor deposition: an in situ nanocalorimetric study. *Physical chemistry chemical physics : PCCP*, 12(44):14693–8, nov 2010.

[84] Li Li, Xuan Liu, Shyam Pal, Shulan Wang, Christopher K. Ober, and Emmanuel P. Giannelis. Extreme ultraviolet resist materials for sub-7 nm patterning. *Chemical Society Reviews*, 46(16):4855–4866, aug 2017.

[85] Po-Han Lin, Ivan Lyubimov, Lian Yu, M D Ediger, and Juan J de Pablo. Molecular modeling of vapor-deposited polymer glasses. *The Journal of chemical physics*, 140(20):204504, may 2014.

[86] Xikui Liu and Ming Jiang. Optical switching of self-assembly: Micellization and micellehollow-sphere transition of hydrogen-bonded polymers. *Angewandte Chemie International Edition*, 45(23):3846–3850, 2006.

[87] Slade Louise, Levine Harry, Ievolella James, and Wang Martha. The glassy state phenomenon in applications for the food industry: Application of the food polymer science approach to structurefunction relationships of sucrose in cookie and cracker systems. *Journal of the Science of Food and Agriculture*, 63(2):133–176.

[88] Ivan Lyubimov, Lucas Antony, Diane M. Walters, David Rodney, M. D. Ediger, and Juan J. de Pablo. Orientational anisotropy in simulated vapor-deposited molecular glasses. *The Journal of Chemical Physics*, 143(9):094502, 2015.

[89] Ivan Lyubimov, M D Ediger, and Juan J de Pablo. Model vapor-deposited glasses: growth front and composition effects. *The Journal of chemical physics*, 139(14):144505, oct 2013.

[90] Seth R Marder, Lap-Tak Cheng, Bruce G Tiemann, Andrienne C Friedli, Mireille Blanchard-Desce, Joseph W Perry, and Jørgen Skindhøj. Large First Hyperpolarizabilities in Push-Pull Polyenes by Tuning of the Bond Length Alternation and Aromaticity. *Science*, 263(5146):511–514, 1994.

[91] Glenn J Martyna, Michael L Klein, and Mark Tuckerman. Nosé–hoover chains: the canonical ensemble via continuous dynamics. *The Journal of chemical physics*, 97(4):2635–2643, 1992.

[92] Elio Mattia and Sijbren Otto. Supramolecular systems chemistry. *Nature Nanotechnology*, 10(2):111–119, feb 2015.

[93] James H McAliley and David A Bruce. Development of Force Field Parameters for Molecular Simulation of Polylactide. *Journal of Chemical Theory and Computation*, 7(11):3756–3767, 2011.

[94] Estíbaliz Merino and María Ribagorda. Control over molecular motion using the cis-trans photoisomerization of the azo group. *Beilstein journal of organic chemistry*, 8:1071–90, 2012.

[95] Stephen Mirigian and Kenneth S. Schweizer. Theory of activated glassy relaxation, mobility gradients, surface diffusion, and vitrification in free standing thin films. *The Journal of Chemical Physics*, 143(24):244705, 2015.

[96] Amaresh Mishra and Peter Bäuerle. Small molecule organic semiconductors on the move: Promises for future solar energy technology. *Angewandte Chemie - International Edition*, 51(9):2020–2067, 2012.

[97] Shuichi Miyamoto and Peter A. Kollman. Settle: An analytical version of the SHAKE and RATTLE algorithm for rigid water models. *Journal of Computational Chemistry*, 13(8):952–962, oct 1992.

[98] Bojan Mohar. Laplace eigenvalues of graphsa survey. *Discrete Mathematics*, 109(1):171 – 183, 1992.

[99] Mijanur Rahaman Molla and Suhrit Ghosh. Exploring Versatile Sulfhydryl Chemistry in the Chain End of a Synthetic Polylactide. *Macromolecules*, 45(21):8561–8570, 2012.

[100] A Mostad and C Romming. Refinement of crystal-structure of cis-azobenzene. *Acta Chemica Scandinavica*, 25(10):3561–&, 1971.

[101] Takahiro Muraoka, Kazushi Kinbara, and Takuzo Aida. Mechanical twisting of a guest by a photoresponsive host. *Nature*, 440(7083):512–515, mar 2006.

[102] K Nakayama, L Jiang, T Iyoda, K Hashimoto, and A Fujishima. Photo-induced structural transformation on the surface of azobenzene crystals. *Japanese Journal of Applied Physics Part 1-Regular Papers Short Notes & Review Papers*, 36(6B):3898–3902, JUN 1997. 4th International Colloquium on Scanning Tunneling Microscopy, KANAZAWA INST TECHNOL, KANAZAWA, JAPAN, DEC 12-14, 1996.

[103] Almeria Natansohn and Paul Rochon. Photoinduced motions in azobenzenebased amorphous polymers: Possible photonic devices. *Advanced Materials*, 11(16):1387–1391, 1999.

[104] Almeria Natansohn and Paul Rochon. Photoinduced Motions in Azo-Containing Polymers. *Chemical Reviews*, 102(11):4139–4176, 2002.

[105] Rachel K. O'Reilly, Craig J. Hawker, and Karen L. Wooley. Cross-linked block copolymer micelles: functional nanostructures of great potential and versatility. *Chemical Society Reviews*, 35(11):1068, oct 2006.

[106] Haida Osamu, Suga Hiroshi, and Seki Syz. New finding of three kinds of glassy state por cyclohexene as a single compound. *Chemistry Letters*, 2(1):79–82, 1973.

[107] Szilárd Páll, Mark James Abraham, Carsten Kutzner, Berk Hess, and Erik Lindahl. Tackling Exascale Software Challenges in Molecular Dynamics Simulations with GROMACS. In Stefano Markidis and Erwin Laure, editors, *Solving Software Challenges for Exascale*, pages 3–27, Cham, 2015. Springer International Publishing.

[108] F Papadimitrakopoulos, XM Zhang, and KA Higginson. Chemical and morphological stability of aluminum tris(8-hydroxyquinoline) (Alq(3)): Effects in light-emitting devices. *IEEE Journal of Selected Topics in Quantum Electronics*, 4(1):49–57, JAN-FEB 1998.

[109] M Parrinello and A Rahman. Polymorphic transitions in single crystals: A new molecular dynamics method. *Journal of Applied Physics*, 52(12):7182–7190, 1981.

[110] Jeremy Pencer and F Ross Hallett. Effects of Vesicle Size and Shape on Static and Dynamic Light Scattering Measurements. *Langmuir*, 19(18):7488–7497, 2003.

[111] S Plimpton. Fast parallel algorithms for short-range molecular-dynamics. *Journal of Computational Physics*, 117(1):1–19, MAR 1 1995.

[112] Sander Pronk, Szilárd Páll, Roland Schulz, Per Larsson, Pär Bjelkmar, Rossen Apostolov, Michael R Shirts, Jeremy C Smith, Peter M Kasson, David van der Spoel, Berk Hess, and Erik Lindahl. GROMACS 4.5: a high-throughput and highly parallel open source molecular simulation toolkit. *Bioinformatics*, 29(7):845–54, April 2013.

[113] Yue Qiu, Lucas W. Antony, Juan J. de Pablo, and M. D. Ediger. Photostability can be significantly modulated by molecular packing in glasses. *Journal of the American Chemical Society*, 138(35):11282–11289, 2016. PMID: 27517130.

[114] Yue Qiu, Shakeel S. Dalal, and M. D. Ediger. Vapor-deposited organic glasses exhibit enhanced stability against photodegradation. *Soft Matter*, 14:2827–2834, 2018.

[115] Sergio Luis L. M. Ramos, Atsuko K. Chigira, and Masaharu Oguni. Devitrification Properties of Vapor-Deposited Ethylcyclohexane Glasses and Interpretation of the Molecular Mechanism for Formation of Vapor-Deposited Glasses. *Journal of Physical Chemistry B*, 119(10):4076–4083, MAR 12 2015.

[116] Sergio Luis L. M. Ramos, Masaharu Oguni, Kikujiro Ishii, and Hideyuki Nakayama. Character of devitrification, viewed from enthalpic paths, of the vapor-deposited ethylbenzene glasses. *The Journal of Physical Chemistry B*, 115(49):14327–14332, 2011. PMID: 22087882.

[117] Daniel R. Reid, Ivan Lyubimov, M. D. Ediger, and Juan J. de Pablo. Age and structure of a model vapour-deposited glass. *Nature Communications*, 7:13062, oct 2016.

[118] Daniele Rezzonico, Mojca Jazbinsek, Peter Gunter, Christian Bosshard, Denise H. Bale, Yi Liao, Larry R. Dalton, and Philip J. Reid. Photostability studies of pi-conjugated chromophores with resonant and nonresonant light excitation for long-life polymeric telecommunication devices. *Journal of the Optical Society of America B-Optical Physics*, 24(9):2199–2207, SEP 2007.

[119] C. Rodriguez-Tinoco, M. Gonzalez-Silveira, J. Rafols-Ribe, G. Garcia, and J. Rodriguez-Viejo. Highly stable glasses of celecoxib: Influence on thermo-kinetic properties, microstructure and response towards crystal growth. *JOURNAL OF NON-CRYSTALLINE SOLIDS*, 407(SI):256–261, JAN 1 2015. 7th International Discussion Meeting on Relaxations in Complex Systems (IDMRCS), Univ Politecnica Catalunya, Barcelona, SPAIN, JUL 21-26, 2013.

[120] Cristian Rodríguez-Tinoco, Marta Gonzalez-Silveira, Joan Ràfols-Ribé, Aitor F. Lopeandía, Maria Teresa Clavaguera-Mora, and Javier Rodríguez-Viejo. Evaluation of Growth Front Velocity in Ultrastable Glasses of Indomethacin over a Wide Temperature Interval. *The Journal of Physical Chemistry B*, 118(36):10795–10801, sep 2014.

[121] JS Royal and JM Torkelson. Photochromic and Fluorescent-Probe Studies in Glassy Polymer Matrices .5. Effects of Physical Aging on bisphenol-a polycarbonate and poly(vinyl acetate) as Sensed by a Size Distribution of Photochromic Probes. *Macromolecules*, 25(18):4792–4796, AUG 31 1992.

[122] Jean-Paul Ryckaert, Giovanni Ciccotti, and Herman J C Berendsen. Numerical integration of the cartesian equations of motion of a system with constraints: molecular dynamics of n-alkanes. *Journal of Computational Physics*, 23(3):327–341, 1977.

[123] Daniel P. Sanders. Advances in Patterning Materials for 193 nm Immersion Lithography. *Chemical Reviews*, 110(1):321–360, jan 2010.

[124] Marina Saphiannikova and Vladimir Toshchevikov. Optical deformations of azobenzene polymers: Orientation approach vs. photofluidization concept. *Journal of the Society for Information Display*, 23(4):146–153, apr 2015.

[125] Elamprakash N Savariar, Sivakumar V Aathimanikandan, and S Thayumanavan. Supramolecular Assemblies from Amphiphilic Homopolymers: Testing the Scope. *Journal of the American Chemical Society*, 128(50):16224–16230, 2006.

[126] G. M. J. Schmidt. Photodimerization in the solid state. *Pure and Applied Chemistry*, 27(4):647–678, 1971.

[127] Holger Schönherr, Joseph M Johnson, Peter Lenz, Curtis W Frank, and Steven G Boxer. Vesicle Adsorption and Lipid Bilayer Formation on Glass Studied by Atomic Force Microscopy. *Langmuir*, 20(26):11600–11606, 2004.

[128] Ruben Seifert, Ines Rabelo de Moraes, Sebastian Scholz, Malte C. Gather, Bjoern Luessem, and Karl Leo. Chemical degradation mechanisms of highly efficient blue phosphorescent emitters used for organic light emitting diodes. *Organic Electronics*, 14(1):115–123, JAN 2013.

[129] Nataraja SekharYadavalli, SarahLoebner, ThomasPapke, ElenaSava, NicolaeHurduc, and SvetlanaSanter. A comparative study of photoinduced deformation in azobenzene containing polymer films. *Soft Matter*, 12(9):2593–2603, feb 2016.

[130] Z Sekkat, G Kleideiter, and T Knoll. Optical orientation of azo dye in polymer films at high pressure. *Journal of the Optical Society of America B-Optical Physics*, 18(12):1854–1857, DEC 2001.

[131] Z Sekkat, J Wood, and W Knoll. Reorientation mechanism of azobenzenes within the trans-double-right-arrow-cis photoisomerization. *Journal of Physical Chemistry*, 99(47):17226–17234, NOV 23 1995.

[132] A. Sepulveda, M. Tylinski, A. Guiseppi-Elie, R. Richert, and M. D. Ediger. Role of Fragility in the Formation of Highly Stable Organic Glasses. *Physical Review Letters*, 113(4), JUL 23 2014.

[133] Yasuhiko Shirota and Hiroshi Kageyama. Charge carrier transporting molecular materials and their applications in devices. *Chemical Reviews*, 107(4):953–1010, APR 2007.

[134] Sadanand Singh and Juan J. de Pablo. A molecular view of vapor deposited glasses. *The Journal of Chemical Physics*, 134(19):194903, 2011.

[135] Sadanand Singh, M D Ediger, and Juan J de Pablo. Ultrastable glasses from in silico vapour deposition. *Nature Materials*, 12(2):139–44, feb 2013.

[136] Mutasem Omar Sinnokrot and C. David Sherrill. High-accuracy quantum mechanical studies of interactions in benzene dimers. *The Journal of Physical Chemistry A*, 110(37):10656–10668, 2006. PMID: 16970354.

[137] Ryutaro Souda. Surface and interface effects on structural transformation of vapor-deposited ethylbenzene films. *Surface Science*, 605(7-8):793–798, apr 2011.

[138] C Soutis. Carbon fiber reinforced plastics in aircraft construction. *Materials Science and Engineering A-Structural Materials Properties Microstructure and Processing*, 412(1-2, SI):171–176, DEC 5 2005. International Conference on Recent Advances in Composite Materials (ICRACM 2004), Banaras Hindu Univ, Varanasi, INDIA, DEC 17-19, 2004.

[139] Jacob D. Stevenson, Aleksandra M. Walczak, Randall W. Hall, and Peter G. Wolynes. Constructing explicit magnetic analogies for the dynamics of glass forming liquids. *Journal of Chemical Physics*, 129(19), NOV 21 2008.

[140] Stephen F Swallen, Kenneth L Kearns, Marie K Mapes, Yong Seol Kim, Robert J McMahon, M D Ediger, Tian Wu, Lian Yu, and Sushil Satija. Organic glasses with exceptional thermodynamic and kinetic stability. *Science (New York, N.Y.)*, 315(5810):353–6, jan 2007.

[141] Stephen F. Swallen, Kenneth L. Kearns, Marie K. Mapes, Yong Seol Kim, Robert J. McMahon, M. D. Ediger, Tian Wu, Lian Yu, and Sushil Satija. Organic glasses with exceptional thermodynamic and kinetic stability. *Science*, 315(5810):353–356, JAN 19 2007.

[142] Stephen F Swallen, Kenneth L Kearns, Sushil Satija, Katherine Traynor, Robert J McMahon, and M D Ediger. Molecular view of the isothermal transformation of a stable glass to a liquid. *The Journal of chemical physics*, 128(21):214514, jun 2008.

[143] OM Tanchak and CJ Barrett. Light-induced reversible volume changes in thin films of azo polymers: The photomechanical effect. *Macromolecules*, 38(25):10566–10570, DEC 13 2005.

[144] Takahiro Tanino, Satoru Yoshikawa, Toshiki Ujike, Daisuke Nagahama, Kazuyuki Moriwaki, Toru Takahashi, Yoshiko Kotani, Hideyuki Nakano, and Yasuhiko Shirota. Creation of azobenzene-based photochromic amorphous molecular materials - synthesis, glass-forming properties, and photochromic response. *Journal of Materials Chemistry*, 17(47):4953–4963, 2007.

[145] Karl J. Thorley and Chad Risko. Mapping the configuration dependence of electronic coupling in organic semiconductors. *J. Mater. Chem. C*, 4:3825–3832, 2016.

[146] Daniel Trawny, Valentin Kunz, and HansUlrich Reissig. Modular Syntheses of Star-Shaped Pyridine, Bipyridine, and Terpyridine Derivatives by Employing Sonogashira Reactions. *European Journal of Organic Chemistry*, 2014(28):6295–6302.

[147] Gareth A Tribello, Massimiliano Bonomi, Davide Branduardi, Carlo Camilloni, and Giovanni Bussi. PLUMED 2: New feathers for an old bird. *Computer Physics Communications*, 185(2):604–613, 2014.

[148] M. Tylinski, A. Sepulveda, Diane M. Walters, Y. Z. Chua, C. Schick, and M. D. Ediger. Vapor-deposited glasses of methyl-m-toluate: How uniform is stable glass transformation? *Journal of Chemical Physics*, 143(24), DEC 28 2015.

[149] Wilfred T. Tysoe, Graeme L. Nyberg, and Richard M. Lambert. Low temperature catalytic chemistry of the Pd(111) surface: benzene and ethylene from acetylene. *Journal of the Chemical Society, Chemical Communications*, 0(11):623, jan 1983.

[150] M. Valiev, E.J. Bylaska, N. Govind, K. Kowalski, T.P. Straatsma, H.J.J. Van Dam, D. Wang, J. Nieplocha, E. Apra, T.L. Windus, and W.A. de Jong. Nwchem: A comprehensive and scalable open-source solution for large scale molecular simulations. *Computer Physics Communications*, 181(9):1477 – 1489, 2010.

[151] David van der Spoel, Erik J. W. Wensink, and Alex C. Hoffmann. Lifting a wet glass from a table: a microscopic picture. *Langmuir*, 22(13):5666–5672, 2006. PMID: 16768492.

[152] Hartel Richard W., Ergun Roja, and Vogel Sarah. Phase/state transitions of confectionery sweeteners: Thermodynamic and kinetic aspects. *Comprehensive Reviews in Food Science and Food Safety*, 10(1):17–32.

[153] Diane M. Walters, Ranko Richert, and M. D. Ediger. Thermal stability of vapor-deposited stable glasses of an organic semiconductor. *Journal of Chemical Physics*, 142(13), APR 7 2015.

[154] Guang Wang, Xia Tong, and Yue Zhao. Preparation of Azobenzene-Containing Amphiphilic Diblock Copolymers for Light-Responsive Micellar Aggregates. *Macromolecules*, 37(24):8911–8917, 2004.

[155] Qi Wang, Yichun Luo, and Hany Aziz. Photodegradation of the organic/metal cathode interface in organic light-emitting devices. *Applied Physics Letters*, 97(6), AUG 9 2010.

[156] C. Grant Willson and Bernard J. Roman. The Future of Lithography: SEMATECH Litho Forum 2008. *ACS Nano*, 2(7):1323–1328, jul 2008.

[157] Munenori Yamada, Mizuho Kondo, Jun-ichi Mamiya, Yanlei Yu, Motoi Kinoshita, ChristopherJ. Barrett, and Tomiki Ikeda. Photomobile polymer materials: Towards light-driven plastic motors. *Angewandte Chemie International Edition*, 47(27):4986–4988, 2008.

[158] Bin Yan, Xia Tong, Patrick Ayotte, and Yue Zhao. Light-responsive block copolymer vesicles based on a photo-softening effect. *Soft Matter*, 7(21):10001–10009, 2011.

[159] Yunqi Yan, Xin Wang, Jennifer I. L. Chen, and David S. Ginger. Photoisomerization Quantum Yield of Azobenzene-Modified DNA Depends on Local Sequence. *Journal of the American Chemical Society*, 135(22):8382–8387, JUN 5 2013.

[160] In-Chul Yeh and Max L. Berkowitz. Ewald summation for systems with slab geometry. *The Journal of Chemical Physics*, 111(7):3155, 1999.

[161] Daisuke Yokoyama. Molecular orientation in small-molecule organic light-emitting diodes. *Journal of Materials Chemistry*, 21(48):19187, nov 2011.

[162] Daisuke Yokoyama, Yousuke Setoguchi, Akio Sakaguchi, Michio Suzuki, and Chihaya Adachi. Orientation Control of Linear-Shaped Molecules in Vacuum-Deposited Organic Amorphous Films and Its Effect on Carrier Mobilities. *Advanced Functional Materials*, 20(3):386–391, feb 2010.

[163] Hani Younes and Daniel Cohn. Phase separation in poly(ethylene glycol)/poly(lactic acid) blends. *European Polymer Journal*, 24(8):765–773, 1988.

[164] L Yu. Amorphous pharmaceutical solids: preparation, characterization and stabilization. *Advanced Drug Delivery Reviews*, 48(1):27–42, MAY 16 2001.

[165] Wei Zhang, Caleb W. Brian, and Lian Yu. Fast Surface Diffusion of Amorphous o-Terphenyl and Its Competition with Viscous Flow in Surface Evolution. *Journal of Physical Chemistry B*, 119(15):5071–5078, APR 16 2015.

[166] Ye Zhang, Wai-Shing Luk, Hai Zhou, Changhao Yan, and Xuan Zeng. Layout decomposition with pairwise coloring for multiple patterning lithography. In *2013 IEEE/ACM International Conference on Computer-Aided Design (ICCAD)*, pages 170–177. IEEE, nov 2013.

[167] Yifan Zhang, Jaesang Lee, and Stephen R. Forrest. Tenfold increase in the lifetime of blue phosphorescent organic light-emitting diodes. *Nature Communications*, 5, SEP 2014.

[168] Hesong Zhao, Zhun Liu, Sang-Hyuk Park, Sang-Ho Kim, Jung-Hyun Kim, and Longhai Piao. Preparation and Characterization of PEG/PLA Multiblock and Triblock Copolymer. *Bulletin of the Korean Chemical Society*, 33, 2012.

[169] L. Zhu, C. W. Brian, S. F. Swallen, P. T. Straus, M. D. Ediger, and L. Yu. Surface self-diffusion of an organic glass. *Phys. Rev. Lett.*, 106:256103, Jun 2011.

[170] Lei Zhu and Lian Yu. Generality of forming stable organic glasses by vapor deposition. *Chemical Physics Letters*, 499(1):62–65, 2010.